UCLouvain

École polytechnique de Louvain

Self-centering reinforced concrete shear walls with shape-memory alloy rebars:

Experimental response and mechanics-based modelling

Author: **Sébastien de Cock de Rameyen**
Supervisor: **João Saraiva Esteves Pacheco De Almeida**
Readers: **Catherine Doneux, Jose Baena Urrea, Martin Steinmetz**
Academic year 2019–2020
Master [120] in Civil Engineering

UCLouvain
École polytechnique de Louvain

Remerciements

Je tiens tout d'abord à exprimer mes plus sincères remerciements à mon promoteur, le professeur João Saraiva Esteves Pacheco de Almeida. Merci pour tout le temps consacré à m'aiguiller semaine après semaine à travers ces « Namazu meetings » qui ont toujours dépassé l'heure qui leur était prévue. Je n'aurais pas pu avoir un meilleur encadrement que ce soit de jour ou par mail à 3h du matin.

Je remercie aussi Martin Steinmetz, Thomas Wyckmans, Tristan Herrezeel et Fabrice Rigot pour leur travail sans lequel mon mémoire n'aurait pas été possible. Ils ont toujours été disponibles et prêts à répondre à la moindre question. J'aimerais souligner tout particulièrement le soutien et la participation de Martin à la réalisation de mon mémoire. Merci d'avoir eu le courage de m'accompagner dans l'exploration de la montagne de données qui m'a été remise. J'ai passé tellement de temps dans son bureau que Igor a failli me faire un double des clés.

Je voudrais remercier ensuite toute l'équipe du LEMSC pour leur accueil et leurs conseils avisés. Plus particulièrement, Samuel Laurent pour son aide et la patience avec laquelle il m'a familiarisé avec la DIC.

Je remercie aussi M. Danilo Tarquini pour avoir pris le temps de m'expliquer en détails le modèle qu'il a développé et le code qui l'accompagne un peu moins d'une semaine avant son mariage.

Finalement, je tiens à remercier tous mes proches pour leur soutien et leurs encouragements que ce soit durant la réalisation de ce mémoire ou tout au long de mes études.

UCLouvain

École polytechnique de Louvain

Abstract

Seismically-induced economic damage and post-earthquake repairability are largely related to the existence of residual structural displacements. This thesis develops and tests the use of shape memory alloy rebars to replace traditional steel rebars in restricted regions of reinforced concrete shear walls. Large-scale cyclic quasi-static experimental tests on two units, predominantly behaving in flexure, show major improvements in terms of minimisation of damage and residual displacements. Additionally, the superelastic flag-shaped hysteretic response of the smart alloys in the wall boundary elements guarantees a sizeable energy dissipation, opening a promising avenue both for application in new constructions and repair works.

Additionally, to further analyse the results, this thesis presents the adaptation of a mechanical model to simulate reinforced concrete wall boundary elements with shape memory alloy rebars. The model is composed of a set of elements which account for different sources of deformation. For an imposed global displacement of the boundary elements, the model provides the steel, concrete and SMA stress and strain profiles and the crack distribution and opening. Overall, a good match is obtained between the numerical and the experimental results from the previously mentioned experiments.

UCLouvain

École polytechnique de Louvain

Table of Contents

List of figures and tables

List of abbreviations and symbols

A_c	[mm^2]	Concrete area
A_s	[mm^2]	Steel area
A_{sma}	[mm^2]	SMA area
A_t	[mm^2]	Total sectional area
E_c	[GPa]	Concrete elastic stiffness
E_s	[GPa]	Steel elastic stiffness
E_{sh}	[GPa]	Steel plastic stiffness
f_{ct}	[MPa]	Concrete tensile strength
f_c'	[MPa]	Concrete compressive strength
f_y	[MPa]	Steel yield strength
f_u	[MPa]	Steel ultimate strength
L_0	[mm]	Total length of the RC wall boundary element (or of the tension chord)
l_0	[mm]	Straight length of the anchored rebar
l_{ac}	[mm]	Length required to develop the steel strain at crack (ε_{ac})
$l_{ac,p}$	[mm]	Length required to develop the plastic portion of the steel strain at crack ($\varepsilon_{ac} - \varepsilon_y$)
$l_{ac,s}$	[mm]	Length required to develop the SMA strain at crack ($\varepsilon_{ac} < \varepsilon_{AMf}$)
$l_{ac,s}$	[mm]	Length required to develop the SMA strain at crack ($\varepsilon_{ac} > \varepsilon_{AMf}$)
l_{anc}	[mm]	Anchorage length
l_b	[mm]	Development length required to pass from a pre-crack to a post-crack steel stress state
l_p	[mm]	Length required to develop the total rebar plastic strain ($\varepsilon_{ult} - \varepsilon_y$)
l_s	[mm]	Lap splice length
l_y	[mm]	Development length required to achieve rebar yielding
$l_{y,eqF}$	[mm]	Distance between the yield point and the first point in which ε_{eqF} is reached
l_{ult}	[mm]	Development length required to achieve rebar rupture
N	[kN]	Imposed axial force
N_c	[kN]	Concrete force
N_{cs}	[kN]	Force required to attain crack stabilization

$N_{c,max}$	[kN]	Maximum force carried by the concrete (at *srm/2*) with reinforcement remaining elastic
$N_{c,max,p}$	[kN]	Maximum force carried by the concrete (at *srm/2*) with reinforcement that has yielded
N_s	[kN]	Steel force
N_{fc}	[kN]	Force required to attain first cracking
$N_{fc,lap}$	[kN]	Force required to attain first cracking within the lap splice region
C	[mm]	Concrete cover
srm	[mm]	Crack spacing
u_s	[mm]	Steel displacement
u_{sma}	[mm]	SMA displacement
u_c	[mm]	Concrete displacement
w	[mm]	Crack width
δ	[mm]	Relative steel-concrete slip
$\mathit{\Delta}$	[mm]	Imposed axial displacement
$\mathit{\Delta}_{anc}$	[mm]	Slip of the anchored rebar at the interface
Δ_{comput}	[mm]	Total displacement of the boundary element computed internally (integral of ε_s)
$\mathit{\Delta}_{ls}$	[mm]	Total displacement of a lap splice element
Δ_{peak}	[%]	Peak drift
Δ_{res}	[%]	Residual lateral drift
$\mathit{\Delta}_{TC}$	[mm]	Total displacement of a basic tension chord element
Δ_{tot}	[mm]	Total imposed displacement to the RC wall boundary element
ε_{ac}	[/]	Steel strain at crack location
$\varepsilon_{ac(2)}$	[/]	SMA strain at crack location
ε_c	[/]	Concrete strain
ε_{cs}	[/]	Minimum steel strain required to have crack stabilization
$\varepsilon_{c,srm/2}$	[/]	Concrete strain at midway between two cracks (*srm/2*)
$\varepsilon_{c,y}$	[/]	Steel strain at the point corresponding to steel yielding ($\varepsilon_s = \varepsilon_y$)
ε_{eqF}	[/]	Steel strain at the point where steel and concrete stress are equal within the lap splice zone
ε_p	[/]	Steel plastic strain ($\varepsilon_p = \varepsilon_s - \varepsilon_y$)

ε_s	[/]	Steel strain
$\varepsilon_{srm/2}$	[/]	Steel strain at midway between two cracks (*srm/2*)
ε_{sma}	[/]	SMA strain
ε_y	[/]	Steel yield strain
ε_{ult}	[/]	Ultimate steel strain
$\emptyset_l$	[mm]	Longitudinal rebar diameter
$\emptyset_t$	[mm]	Transversal rebar diameter
ρ_l	[%]	Longitudinal reinforcement ratio
ρ_t	[%]	Transverse reinforcement ratio
σ_c	[MPa]	Concrete stress
$\sigma_{c,max,p}$	[MPa]	Maximum concrete stress between cracks (at *srm/2*) when the steel is in a post-yield state
σ_s	[MPa]	Steel stress
$\sigma_{s,B}$	[MPa]	Concrete stress before crack
$\sigma_{s,C}$	[MPa]	Concrete stress after crack
σ_{sma}	[MPa]	SMA stress
φ	[1/mm]	Local curvature
ϕ_y	[1/mm]	Yield curvature
τ_b	[MPa]	Bond stress
τ_{b0}	[MPa]	Elastic bond stress ($\sigma_s < f_y$)
τ_{b1}	[MPa]	Plastic bond stress ($\sigma_s > f_y$)
τ_{max}	[MPa]	Maximum SMA elastic bond stress

UCLouvain
École polytechnique de Louvain

Introduction

Throughout the 20th century, a steady reduction of the number of casualties from natural disasters has been observed, from approximately 550'000 people per year in the 1920s-1930s to around 50'000 people per year throughout the 1980s-1990s (see Figure 1). This trend reversed and started rising in the period 2000-2015, due to the impact of earthquakes, which became the major natural disaster in term of casualties. Earthquakes kill on average 45'000 people per year, which is approximately 2.5 times more than during the 20th century (EMDAT, 2017). As an example, after the 2010 Haiti earthquake, the Haitian government estimated a death toll of 220 000 casualties and that 250 000 residences and 30 000 commercial buildings collapsed during the earthquake (BBC. 10 February 2010). Examples like this one are not uncommon: the 2004 Indian Ocean earthquake made 227 898 casualties, the 2008 Sichuan and the 2008 Kashmir earthquakes had a death toll of 80 000 each (I. Fehr, 2005). Regarding the economic damage for the same period (2000-2015), the impact of earthquakes is on a steep rise: they are accountable for 1.85 thousand billion US dollars (1.85×10^{12} US$), which corresponds to approximately 27% of the total economic losses from natural disasters (Dunbar, 2014). These costs are partly attributable to excessive post-earthquake residual displacements in structures, which impose very costly repairs or require demolition followed by reconstruction. For instance, Marquis (2017), citing a work by Muir-Wood (2015), indicate that after the New Zealand earthquakes of 2010-2011, approximately 25% of all buildings in the Central Business District of Christchurch were no longer vertical, with tilts equal or larger than 25 mm. In most cases, these out-of-plumb buildings were demolished after being declared "uneconomic to repair". Many other examples could be cited, like the numerous reinforced concrete buildings demolished after the 1985 Mexico earthquake (Rosenblueth and Meli, 1986) (E. Rosenblueth, 1986), or the multiple bridges that also could not be straightened back to their original configuration following the 1995 Kobe earthquake (Kawashima, 2000).

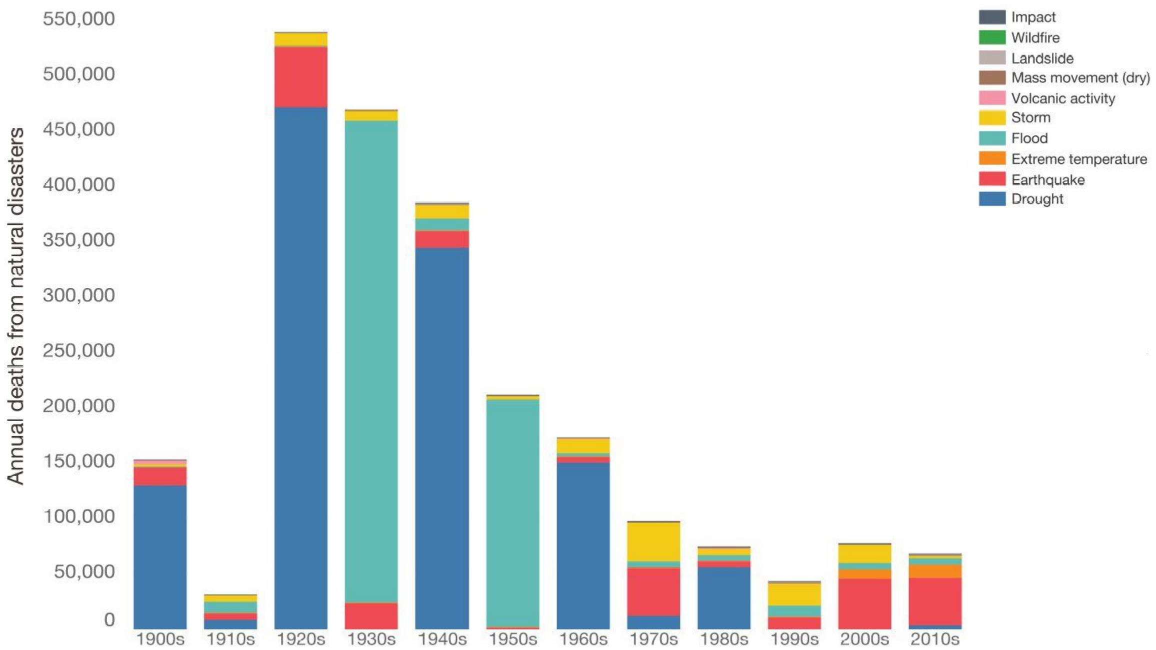

Figure 1 Evolution of the number of deaths due to natural disasters per decade achieved in 2018 according to the data base "OFDA/CRED"

Most of the structures that underwent post-earthquake residual displacements had a satisfactory performance during the earthquake according to modern codes. These codes do not consider or are not sufficiently stringent regarding residual deformations. In fact, many of the demolition decisions are not strictly related to structural engineering considerations but to more subjective aspects, such as building functionality and even psychological well-being impairment. For instance, headaches and dizziness due to perceived inclination angles are well known. A study by McCormick et al. (2008) indicates that the definition of a maximum acceptable residual drift needs to combine the several latter variables. The authors suggest a single standard permissible residual drift level of 0.005 rad as a reference in the development of self-centring systems. These considerations indicate that developed countries and regions with increased seismic awareness, modern design regulations and construction practices may experience limited human casualties during earthquakes, while simultaneously incurring in potentially massive economic losses – also due to usually large wealth and exposure. This was the case of the Christchurch Central Business District, with estimated losses of more than $NZD 40 billion (roughly 20 % of the GDP), demolition of approximately 60% of the multi-storey reinforced concrete buildings, and closure of the core business district for over 2 years (F. Marquis, 2017). There is thus an urgent need for construction technology improvement in order to reduce material damages during and after earthquakes.

1.1 Self-centering technologies

The acknowledgement of the fundamental role of residual displacements has progressively increased through the contribution of analytical studies (G.A. MacRae, 1997), performance-based loss estimation methodologies explicitly incorporating residual deformations (C.M. Ramirez, 2012), seismic resilience quantification frameworks (M. Bruneau, 2007), new design philosophies such as damage avoidance design (J.B. Mander, 1997), and through the development of new materials and technologies. Regarding the development of new technologies, the structural design idea for rocking behaviour has made a considerable impact within the research community. In the 90s, the use of beam prestressing tendons through the joints was first proposed by Priestley and Tao (1993) for reinforced concrete (RC) framed buildings. This idea evolved in modified forms to this day (X. Geng, 2019). RC wall buildings are extensively used as an effective lateral resisting system for mid- and high-rise buildings as well as bridge piers worldwide. Several research programs have focused on the development of self-centring technologies for such buildings. The concept of rocking was incorporated in the design and successful tested on a 60% scale 5-storey precast building developed under the PRESSS research program (M.J.N. Priestley S. S., 1999). The building had a ductile structural frame in one direction and a hybrid structural wall system in the orthogonal one. The hybrid wall concept comes from not being a prestressed-only system, which would show a bilinear elastic self-centring response (due to the restoring force provided by the post-tensioned tendons and the vertical load). Instead, energy dissipation components or devices complement the system, which produces their final characteristic flag-shaped hysteretic behaviour. Many variations of unbonded post-tensioned concrete systems were proposed over the past two decades (T. Holden, 2003) (W.A. Zatar, 2002) (J.I. Restrepo, 2007) (A. Belleri, 2014), for which a state-of-the-art review can be found in Kurama et al. (2018). Recent shake table tests proved the feasibility and the improvements of this technique under realistic nonlinear dynamic loading (K.M. Twigden, 2019). It is noted that the “energy myth”, wherein elasto-plastic behaviour is seen as the most desired hysteretic form of earthquake response, was dispelled by

Priestley and collaborators (Priestley, 2003). In fact, structures with this type of behaviour tend to have large residual deformations, although peak displacements are similar to structures with nonlinear elastic (flag-shaped) hysteresis (see Figure 2).

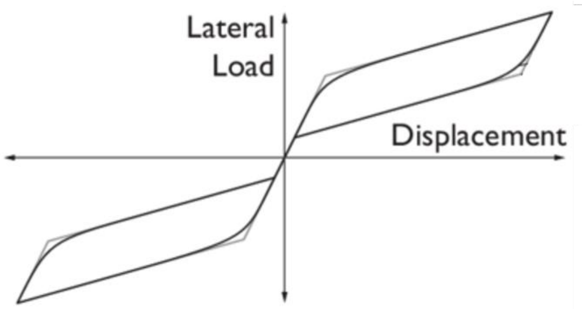

Figure 2 flag-shaped hysteresis latera load, displacement curve (Christopoulos, 2010)

The flag shape hysteresis is particularly interesting in the seismic domain, mainly because of small residual displacement, which can be seen in Figure 2 as the displacement for a null load. Additionally, due to this shape, energy can be dissipated. The flag-shaped hysteretic can be directly found in the constitutive behaviour of one category of metal alloys, known as shape-memory alloys (SMA). This superelastic (or pseudo-elastic) relation is explained by a transition from the austenitic parent phase to stress-induced martensite upon loading, followed by reversion to austenite upon unloading to lower stress (R. DesRoches, 2004). SMA are also appealing because of the increased tangent modulus of martensite at large strains (after the end of the phase transformation), which can be used to control seismic displacements (see Figure 3). Applications of SMA to RC members go well beyond earthquake engineering (B. Mas, 2017) as some take advantage of the thermo-mechanical behaviour of SMA, as these alloys also recover their shape through heating or shape-memory effect (J.M. Rius, 2019). The potential of SMA as reinforcement in RC frames has been explored for more than 10 years: the initial studies focused on their use in plastic hinge regions of columns (M.S. Saiidi H. W., 2006) and beam-column joints (M.A. Youssef, 2008), as well as in beams (M.S. Saiidi M. S.-Z., 2007). The promising results in terms of reduction of post-earthquake residual displacements opened a new and very active line of research, which extended to combination with other materials such as fibre reinforced polymer bars (A.H.M.M. Billah, 2012).

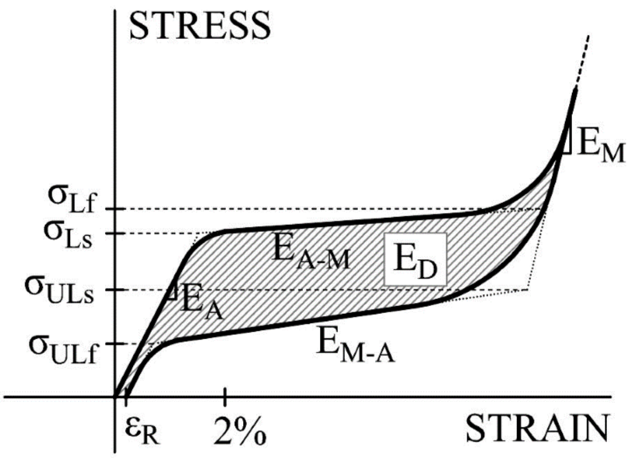

Figure 3 Idealized cyclic behavior of shape memory alloy (Gonzales 2019)

UCLouvain
École polytechnique de Louvain

There are several reasons why the application of SMA rebars is more appealing for RC wall buildings than for RC frames. The first argument is economical, since SMA remain expensive materials and are needed in smaller quantities for RC wall buildings. Indeed, while there are many potential plastic hinge regions in the extremities of every storey columns and bay beams in RC frames, there are usually a rather limited number of walls in wall buildings, for which only one plastic hinge region is designed to form at the base. Additionally, walls behaving in bending are controlled by the boundary elements, suggesting that the placement of SMA rebars can be restricted to such cross-sectional regions. This allows for an extremely reduced required quantity of SMA rebars in wall buildings – particularly when compared to frames – and therefore a negligible overall construction cost increase. The second argument relates to structural mechanics: for an identical curvature demand in a column and a wall, the outermost rebar strains are significantly larger in a wall due to the much-increased effective cross-sectional depth, which suggests an activation of the SMA superelastic effect from smaller displacement demands. Moreover, the SMA "equivalent yield strain", corresponding to the initiation of forward austenite-to-martensite phase transformation, is much larger than the yield strain of standard construction steel rebars. As a consequence, the long wall cross sections promote an enhanced utilization of the combined behaviour of steel rebars in the web and SMA rebars in the boundary regions.

Paradoxically, despite the more attractive cost-benefit performance of SMA in walls, together with a more optimized mechanical use of SMA rebars, there is proportionally less research on walls with SMA rebars than RC frames. It seems that there are only three studies in which the application of SMA rebars in walls is addressed numerically or analytically (E. Abraik, 2015) (M. Maciel, 2016) (B. Wang, 2018) and two experimental studies (A. Abdulridha, 2017) (M.J.T. Kian, 2018). A recent experimental study (L. Cortés-Puentes, 2018) also highlighted how the self-centring properties of walls with SMAs permits an efficient repair, including the reuse of the SMA rebars.

1.2 Thesis objectives

This thesis is based on the observation that, due to laboratory constraints, most existing experimental tests on shear walls involve small shear span ratios (X. Zhai, 2019). This is also the case for existing experimental tests of RC walls with SMA rebars so far (A. Abdulridha, 2017) (M.J.T. Kian, 2018). The construction of considerably taller and more expensive units (T. Holden, 2003) is unfortunately not always possible.

During the previous academic year, two experimental theses on this subject were made. The first thesis (M. Steinmetz, 2019) discusses the conception and the realization of a test setup for a Self-centering reinforced concrete shear walls with shape-memory alloy rebars. This setup aims to produce quasi-static earthquake-resistant tests of high scale structural elements. In June 2019, two paraseismic walls were successfully tested using this experimental setup in the "Laboratoire d'Essais mécaniques, Structures et Génie Civil" (LEMSC). The second thesis (T. Herrezeel, 2019) exposes the dimensioning and a numerical modeling of the aforementioned experiment. Those theses extend the existing test results to larger shear span ratios, representative of most high-rise buildings, where a flexural response of the wall is expected. Additionally, in the design of the test units, a minimal use of SMA rebar lengths was defined – considerably smaller than the plastic hinge length or the lengths used in the other RC+SMA wall tests – and modifications to typical construction practices were avoided. Recent

instrumentation techniques which included one RC wall, namely digital image correlation, provided insights into the local behaviour of the two test units.
The first objective of this thesis is to analyze the results and conclusions of the previous experiments by first combining the findings of the two theses and then assessing the performance of a ductile, hybrid SMA-deformed steel reinforced concrete shear wall.
The second objective is to predict the location and the wideness of the cracks and determine the local stress of the steel and SMA rebar in the wall. This will be obtained by adapting a tension chord model (D. Taquini, 2019) to a concrete wall reinforced with SMA rebars.

1.3 Organization

This thesis starts with a description of the experimental program including test units, test setup, materials and instrumentation of the previous experiments.
Section 2 is a brief summary of the work done in the above-mentioned theses.
Section 3 fulfills the first objective of this thesis: it exposes the experimental response and presents the general test results as well as more specific features of the units' response.

Section 4 marks the start of the second objective of this thesis. It exposes exiting tension chord model (D. Taquini, 2019) and explains the principles on which it is based. The different elements which compose the model and the general implementation are presented in this section as well. Section 5 exposes the adaptation made on the exiting model to adapt it to a SMA reinforced concrete wall. Once the new model completed, it is then compared to the experiment result. Specific cases and model limitations are developed in section 6.
Finally, the last section outlines the conclusion for both the experiments and the mechanical model adaptation.

2 Experimental program

This section describes the experiment made during a previous thesis which is used as a background for the present thesis. It starts by explaining and illustrating the test setup, including a description of the actuator and its implantation at the technological platform LEMSC (*Laboratoire Essais Mécaniques, Structures et Génie Civil*). The section then continues with the description and difference between the two test units as well as the reinforce layout. Section 2.2 goes over all the materials used, the justification of their choice and properties. Section 2.3 goes over the mechanical coupler between steel and the SMA rebars and his limitations. In Section 2.4, the loading protocol is explained. Finally, section 2.5 resumes all the instrumentation, their use in this test setup and if they were useful to collect data.

2.1 Test setup

The purpose of the experiment is to study the performances of a ductile reinforced concrete shear wall with shape-memory alloy rebars. This stimulation implies a 3-floor building (Figure 4) subject to an earthquake. The test setup imposes a seismic load coupled with the forces induced by the movement of the building to a wall. The goal of the test setup is to represent as accurately as possible the load imposed to one of the base walls of this building. The test setup will then be used to carry out tests on two ductile walls subjected to the same seismic load. The first reinforced concrete wall is sized in accordance with European standards of Eurocode 8. In the second wall, the longitudinal reinforcement in "classic" structural steel are replaced by SMA reinforcements. As this alloy is expensive, it is limited to the most sensitive areas, in this case, the base of the wall.

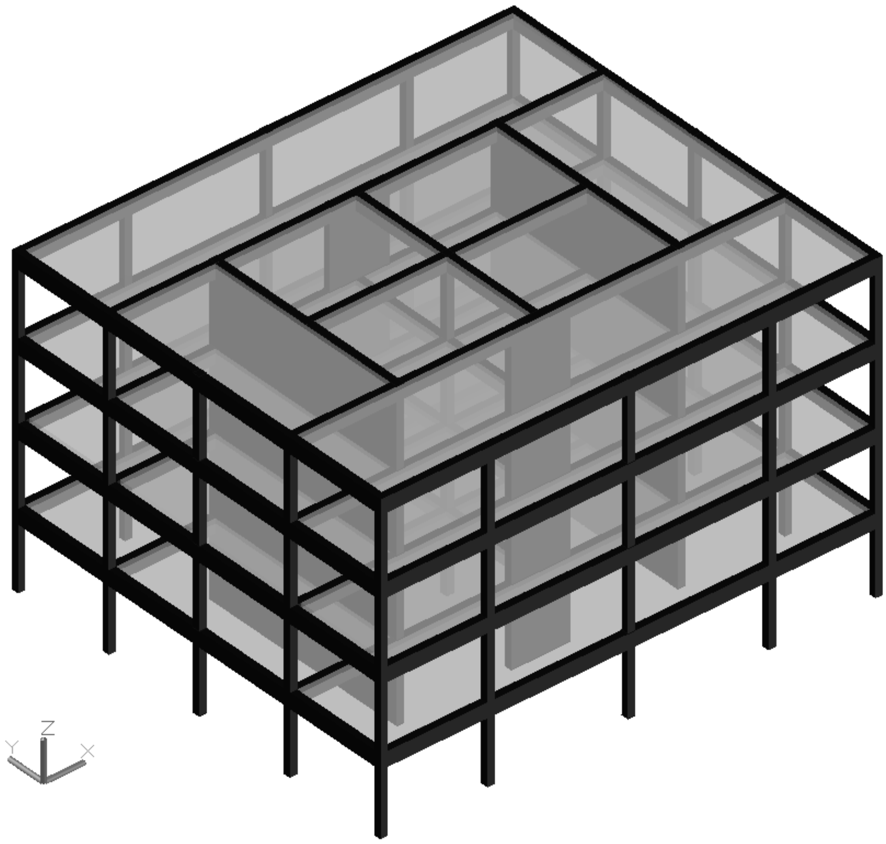

Figure 4 – 3D representation of the 3-floor building used for the experiment (M. Steinmetz, 2019)

The test setup, which is largely inspired by previous works (J.P. Almeida, 2017), was assembled at the technological platform LEMSC of the iMMC (*Institute of Mechanics, Materials, and Civil Engineering*). The setup is illustrated in Figure 5 and Figure 6. It consists of two independent steel frames affixed to the laboratory consolidated floor, one supporting the vertical actuators and the other serving as reaction frame for the horizontal actuator force. One stiffened steel beam is placed over the top RC beam to allow for a larger lever arm between the vertical actuators and simultaneously to better distribute the vertical forces into the wall. The two vertical actuators, both with a force capacity of 350 kN and a stroke of 250 mm, apply a total compressive load of 350 kN and a varying bending moment (corresponding to a chosen and constant shear span, as discussed below) through the actuators' lever arm. The third horizontal actuator (750 kN) applies the cyclic displacement protocol to the top RC beam of the specimen. The latter was post-tensioned with four steel rods (two on North side of the beam, two on the South) connected to H-shaped steel profiles with stiffeners, placed on the East and West extremities of the RC beam. The horizontal actuator was also connected to the East steel profile. All the actuators are hinged on both ends and equipped with load cells.

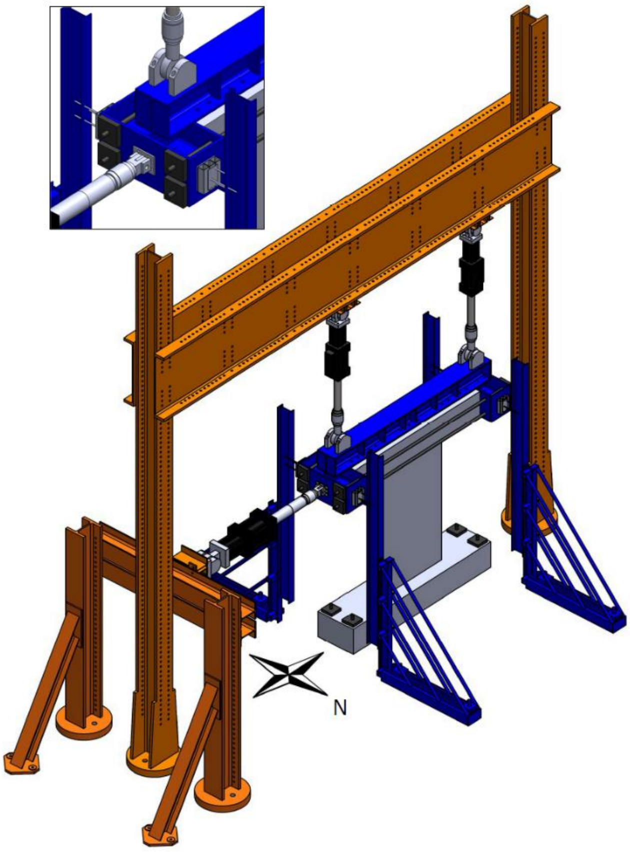

Figure 5 Sketch of the setup assembled at the technological platform LEMSC for the tests of the two walls, together with a close-up of the connection between the horizontal actuator and an extremity H-shaped profile.

The occurrence of out-of-plane displacements at the height of the RC beam is prevented by four sliding supports attached to lateral bracing frames, represented in blue in Figure 5. Each sliding support comprises a plate with spherical rollers connected to the bracing frame by three steel rods instrumented with strain gauges. The rollers can slide over the side plates of the two extremity H-shaped steel profiles, as sketched in the close-up of Figure 5, allowing for a free or reduced-friction in-plane movement of the wall. Throughout the test of the RC wall, the maximum out-of-plane force transmitted to the braces – inferred from the strains measured in the rods – was lower than 13.98 kN, which corresponds to 4 % of the total applied vertical force. For the RC+SMA specimen test, these values were 16.24 kN or 4.6 %.

The axial load ratio (7.3 %) and the shear span ratio (equal to 3.6) imposed during the test is derived from the design of a 12 m tall 4-floor prototype building. The latter is assumed to be located in the highest seismicity region of Belgium (PGA of 0.23 *g*) and composed of two RC walls 1800 mm long and 300 mm thick in each orthogonal direction. *Ad hoc* quasi-static loading protocols are developed by the authors from the results of nonlinear dynamic analysis of the prototype building, and are meant to represent far-fault earthquakes of magnitude around 5 and a PGA of 0.2 *g*. The procedure, detailed in the previously mentioned theses (M. Steinmetz, 2019) (T. Herrezeel, 2019) was inspired by the works of Bazaez and Dusicka (2016) and Mergos and Beyer (2014).

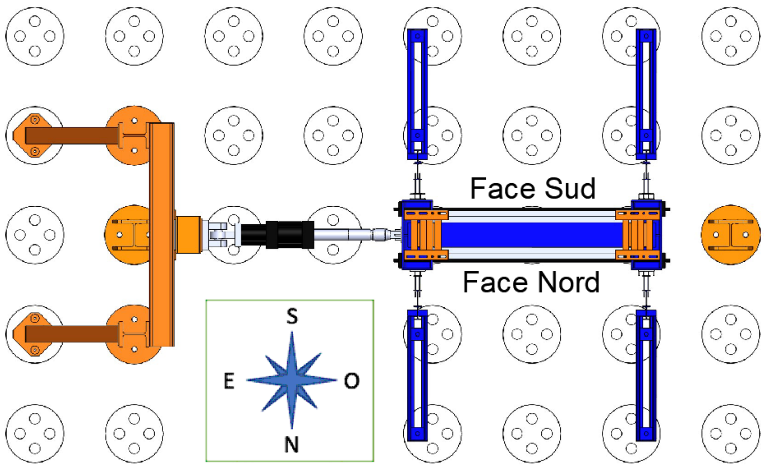

Figure 6 general disposition of the test setup (M. Steinmetz, 2019)

2.1 Test unit

Two units at scale 2:3 with identical geometry are tested: a RC wall designed in accordance to Eurocode 8 (ECS, 2004) and a RC wall with four SMA rebars at the base of each boundary element (herein denoted as RC+SMA), as indicated in Figure 7 reinforcement layout of the two test units RC and RC+SMA wall. . This figure shows that each unit includes a wall 2000 mm tall, 200 mm thick, and 1200 mm long, as well as a top beam (400 × 400 × 2400 mm³) and a foundation (600 × 400 × 2800 mm³). The longitudinal reinforcement of the RC wall consists of two symmetric layers of seven continuous rebars of diameter ϕ_l = 12 mm. The latter corresponds to a total longitudinal reinforcement ratio of ρ_l = 0.66% and a boundary element longitudinal reinforcement ratio of 0.85%. The transverse reinforcement along the wall length consists in 13 rebar layers of ϕ_t = 8 mm, 150 mm apart. At the level of these layers, standard anti-buckling crossties are provided to the longitudinal rebars within the boundary element regions. The latter is further confined by 15 ϕ12 hoops, 150 mm apart, effectively reducing the spacing of horizontal reinforcement in these regions to 75 mm. The total transverse reinforcement ratio is thus $\rho_t = 0.34$ %. The clear concrete cover is 30 thick.

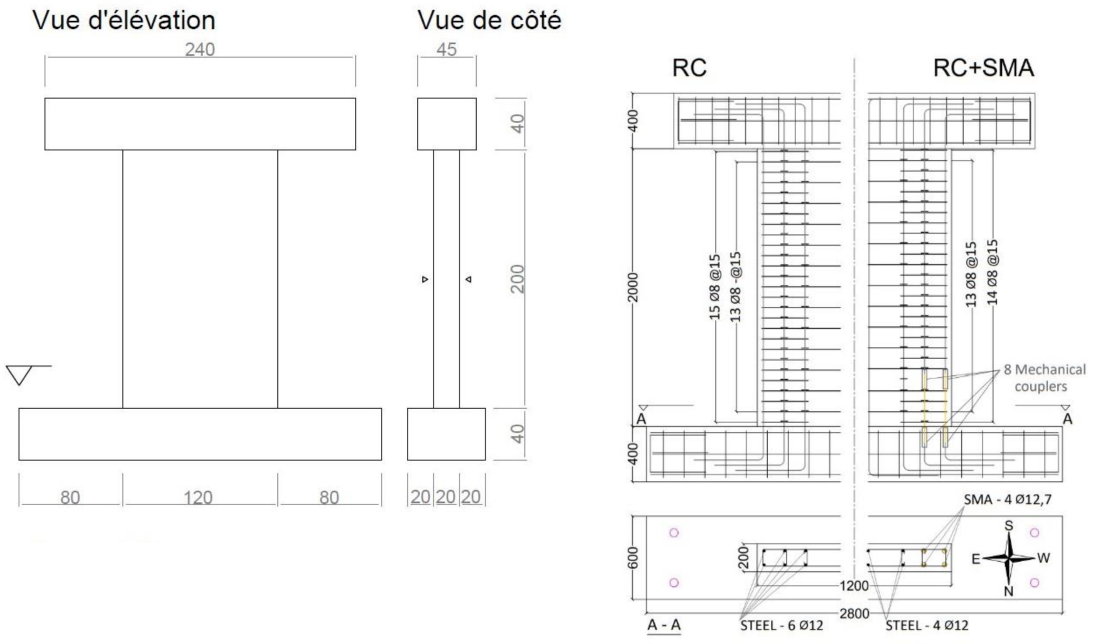

(a) (b)

Figure 7 reinforcement layout of the two test units RC and RC+SMA wall. Units: (a) cm, (b) mm.

For the RC+SMA wall, which is sketched in Figure 7. SMA rebars of diameter ϕ_l = 12.7 mm replace the bottom 270 mm of the longitudinal reinforcement in the wall (10 mm of SMA go in the foundation for a total 280mm free length of SMA). The SMA and standard steel rebars are connected by mechanical couplers, as shown in Figure 8. The presence of the couplers, whose outside diameter (33 mm) is considerably larger than the diameter of the bars they connect, implies skipping one of the boundary element hoops (i.e., 14 were used instead of 15). Owing to their geometry, the test units are cast horizontally in two steps: the first includes the wall itself and the south side of the top beam and foundation, while the second comprises the north side of the top beam and foundation.

Figure 8 Mechanical coupler used to connect the SMA and the standard steel rebars in the test unit RC+SMA (T. Herrezeel, 2019)

2.2 Materials

Material		Properties	Unit	Value
Concrete	$f_{c,cube,mean}$	Mean value of compressive strength	[MPa]	49,2
	$f_{t,cube,mean}$	Mean value of tensile strength	[MPa]	3,9
	ε_{C0}	Strain at compressive strength	[%]	0,23
	ε_{Cu}	Ultimate strain	[%]	0,35
	E_{cm}	Modulus of elasticity	[GPa]	35,1
Steel ϕ12	f_t	Ultimate tensile strength	[MPa]	635
	f_y	Yield tensile strength	[MPa]	517
	E	Modulus of elasticity	[GPa]	205
	$k = f_t/f_y$	Ductility ratio	[-]	1,23
	ε_{sh}	Tensile strain at onset of hardening	[%]	0.29
	ε_{su}	Ultimate tensile strain	[%]	7,6
SMA	E	Modulus of elasticity	[GPa]	31
	σ_{AMs}	Austenite to martensite start stress	[MPa]	319
	σ_{AMf}	Austenite to martensite finish stress	[MPa]	349
	σ_{MAs}	Martensite to austenite start stress	[MPa]	73
	σ_{MAf}	Martensite to austenite finish stress	[MPa]	32
	σ_{nu}	Ultimate tensile strength	[MPa]	1053
	ε_{nu}	Ultimate tensile strain	[%]	13

Table 1 Summary of material properties

2.2.1 Steel and concrete

Concrete cubes vibrated simultaneously with wall casting and were stored in the same conditions than the units up until testing. The properties shown in Table 1 are based on compression and splitting tests in accordance with NBN-EN-12390 (NBN, 2001).

To ensure ductility and energy dissipation, Eurocode 8 (ECS, 2004) requires the use of ductility class C steel for longitudinal reinforcement in critical regions of primary seismic elements. For the wall units of the present study, rebars nominally of Class B were used. However, the results of laboratory tests demonstrated their compliance with requirements for Class C steels, as shown in Table 1. Figure 9 Steel stress strain curves for monotonic and cyclic tests shows the uniaxial monotonic test response of the employed ϕ12 rebars.

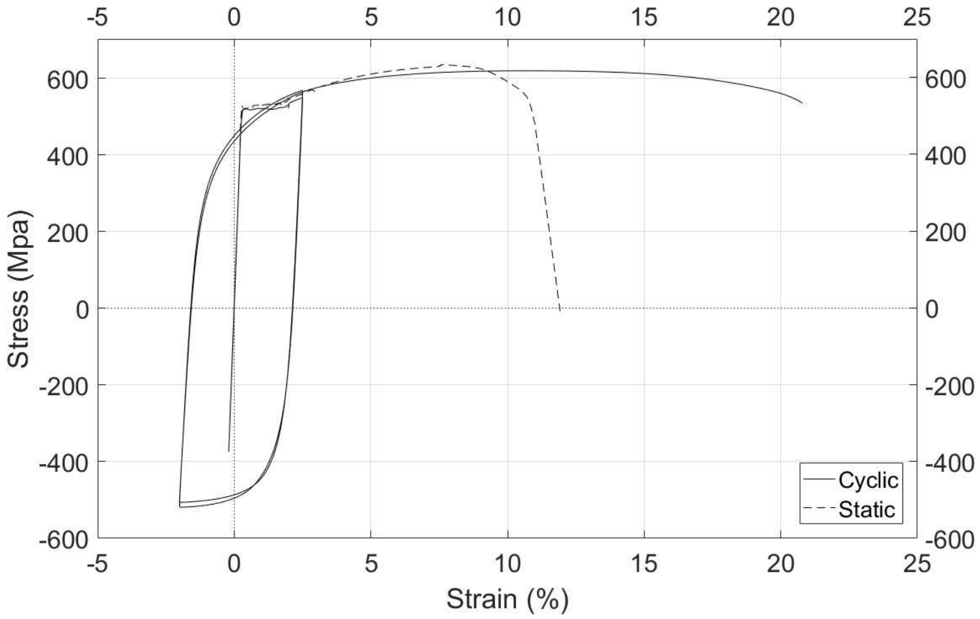

Figure 9 Steel stress strain curves for monotonic and cyclic tests

2.2.2 SMA

Beforehand, the 12.7 mm diameter SMA bars were hot-rolled and then heat-treated to obtain a superelastic behaviour for regular ambient temperatures. Uniaxial monotonic and cyclic tests were carried out at the laboratory, the superposition of which is shown in Figure 10. The results point to a slightly higher stress level triggering martensitic transformation for the monotonic case, when compared with the cyclic response. Then can likely be explained by the lower speed at which the cyclic test was performed. The properties indicated in Table 1 are obtained from the cyclic tests. The superelastic hysteretic behaviour of the SMA can be seen to occur up to deformations of about 6 %, for which a residual strain (the strain which corresponds to a stress of 0 Mpa) of +/- 0.75% can be observed. Beyond this value, a drastic reduction of the pseudo-elastic behaviour of the SMA rebar occurs, e.g. a residual strain of around 3.6 % is obtained upon unloading from an imposed deformation of approximately 8 %.

The use of the SMA can be justified by comparing Figure 10 and Figure 9. During the elastic phase, no energy is dissipated as the stress-strain relation is the same for the loading and the unloading. In other words, the surface area under the curve in Figure 9 for the elastic phase is null. This is not the case for the plastic phase in which the steel has a residual strain of approximately 2 %. From the austenite to the martensite phase (from 1 % to 6 % strains), the SMA dissipate some energy and have for the worst case a residual strain of maximum 0.75 % (see Figure 10). Due to the flag shape hysteresis behaviour, SMA are able of dissipating some energy and have a small residual drift. Those characteristics are a great asset in the para-seismic field as explained in the introduction. Even if steel dissipates more energy, the residual strains is too restrictive in comparison with the SMA.

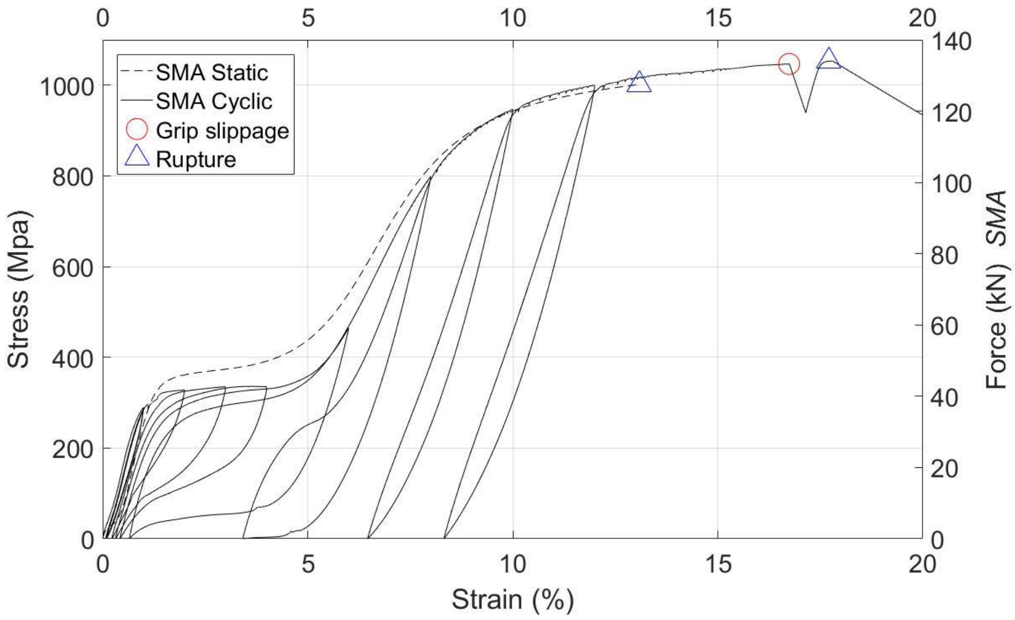

Figure 10 SMA stress strain for monotonic and cyclic tests

2.3 Mechanical couplers

One of the remaining practical challenges for a more widespread application of SMA rebars in RC construction is their connection to the standard ribbed steel rebars due to the smooth surface of the SMA rebars. In the literature, it appears that past structural engineering applications have always resorted to the use of couplers. However, laser welding techniques to connect SMA to steel wires can be found, such as the one proposed by (Hall, 2004), where *Ni* filler metal was used to avoid a brittle welding zone. M.S Alan (2010) developed and tested different mechanical couplers, namely a single bar coupler with three rows of aligned screws arranged at rebar central angles of 120º. This showed a good performance under cyclic tensile stresses. The screws' heads were blunted to reduce SMA rebar punch sensitivity. An identical coupler was used in the study on hybrid RC columns by (A.H.M.M. Billah, 2012). For the RC+SMA wall used in the present study, standard six-screw row couplers were used. The clamping of the rebar was maximized by screwing the SMA bar with five of six head-blunted screws. The steel rebar is fixed by only one screw, in order to guarantee rebar alignment, and is also welded to the extremity of the coupler. Finally, an epoxy injection mortar is infused through a small hole at the coupler's mid-length to further increase adherence between the SMA rebar and the internal coupler surface along its entire length. Prior to the assembly, the SMA rebar is sand-blasted to increase surface roughness. Figure 11 shows a photo of the mechanical coupler with the aforementioned adaptations.

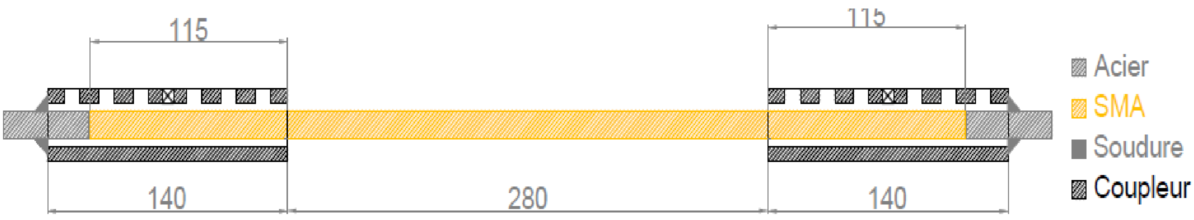

Figure 11 Mechanical coupler used to connect the SMA and the standard steel rebars in the test unit RC+SMA (Herrezeel and Rigot, 2019)

The assembly sketched in Figure 11 – composed of two steel rebars, two couplers, and one connecting SMA bar – was tested in tension. The results shown in Figure 12 indicate a first tensile peak strength at 67.8 kN, beyond which consecutive sudden force drop-and-recovery events take place (at values of resisting force of 68.5 kN and 58.3 kN). Those drops correspond to a local slipping followed by gripping of the SMA rebar in the couplers. The force-displacement response of the assembly during loading appears similar in shape to the stress-strain response of the SMA rebar in Figure 10. This is an expected and desired feature and the diameter of the SMA rebar was chosen along with the design of coupler to behave as such.

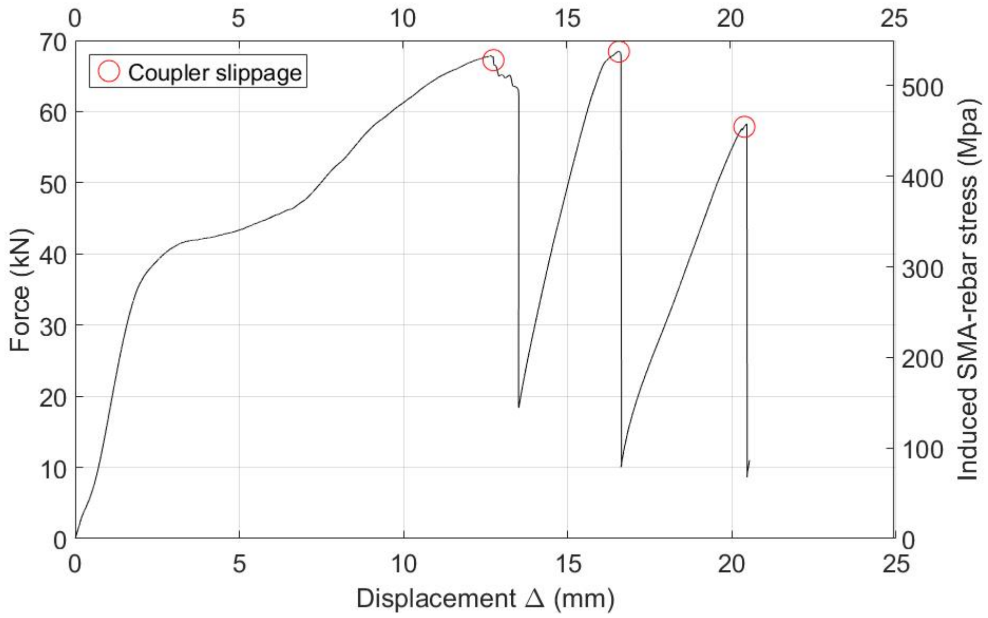

Figure 12 Force-displacement response of the assembly 2 × steel rebar + 2 × couplers + 1 SMA bar.

Namely, as the two additional ordinate axes on the right side of Figure 13 show, the value of the force corresponding to the martensitic transformation was intentionally kept below the yield force of the steel rebar, in order to ensure the concentration of deformations in the smart alloy. This feature is reflected by the formation of a large crack at the base of the RC+SMA wall, as discussed in Section 3. The response curve in Figure 12 also indicates, with reference to the right-hand side ordinate axis, that first sliding occurs well within the full martensitic crystalline phase. The increased tangent modulus due to martensitic crystalline phase can be useful to control seismic displacements as discussed in the introduction.

This test was repeated several times to gauge the variability of the response. All the tests confirmed that the assembly capacity is: (i) largely above the SMA rebar austenite-martensite transition phase, and (ii) equal or larger than the ultimate strength of the steel rebar, hence ensuring also the spread of plasticity to the part of the wall above the coupler. The SMA-steel rebar connection system herein developed is illustrated in Figure 8 to provide a fully satisfactory performance when cast inside the RC wall.

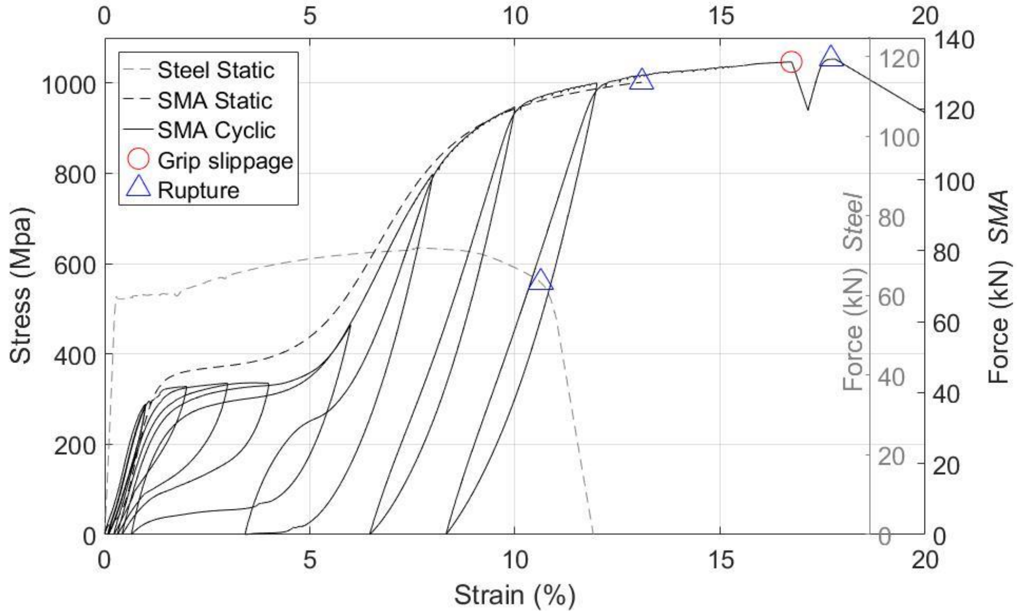

Figure 13 SMA and Steel stress strain comparison

2.4 Loading protocol

(a) (b)

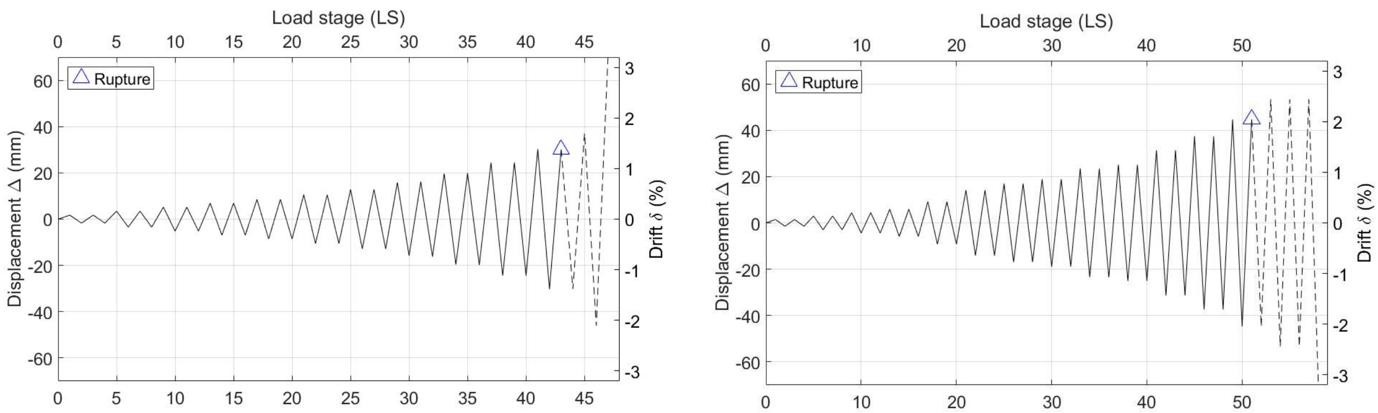

Figure 14 Loading protocol applied to the: (a) RC wall, and (b) RC+SMA wall.

As mentioned in section 2.1, the procedure for the loading protocol can be found in the previously mentioned theses (M. Steinmetz, 2019) (T. Herrezeel, 2019). The resulting protocol imposes a cyclic drift followed by an exponentially increasing envelope. The peak values (positive and negative) of the imposed cyclic drift are named here after load stages (LS). Two cycles, defined by four consecutive load stages, are imposed at each drift value in order to allow stiffness observation and strength degradation. The previous loading protocols, applicable to a prototype wall of 3000 mm (height) × 1800 mm (length) × 300 mm (thickness), are then scaled for the 2:3 test units of the present study. Further details regarding the scaling procedure can be found in Wyckmans and Steinmetz (2019) and Herrezeel and Rigot (2019). The cyclic displacements imposed by the horizontal actuator to the test units follow the scaled quasi-static loading protocols represented in Figure 14 (a) and (b) respectively for the RC wall and the

RC+SMA wall. Although the first load stage (LS01) was applied – by mistake – towards different directions for each wall (push to the West for the RC wall, pull to the East for the RC+SMA wall), the loading protocols, as well as the plots, figures and photos of the following sections, are adjusted as if LS01 had been applied towards the same (positive) direction. A numerical simulation of the test units' response to the indicated axial load and cyclic loading history was performed with the software Opensees (McKenna et al., 2000): additional information and results can be found in section 3. This simulation is particularly useful to define the expected force interval and displacement capacities in order to design the test setup, select the actuators, etc.

2.5 Instrumentation

Both test units were instrumented with conventional and optical measurement systems. In addition, detailed and general photos of the walls were taken both at the load stages and in between load stages. Videos were also recorded during loading. Crack widths were measured manually and with an electronic crack measuring device and compiled in the laboratory notebook. Although the instrumentation is almost identical for both tests, the chains of linear variable displacement transducers (LVDTs) placed along the edges had slight differences. These are shown in Figure 15. An additional piece of equipments not depicted in Figure 15 were installed: four rotational potentiometers (two along the vertical wall edges and two measuring the diagonal unit elongation), two inclinometers, nine micrometres along the wall to measure the base crack width, and 12 strain gauges in the rods of the sliding supports as discussed above.

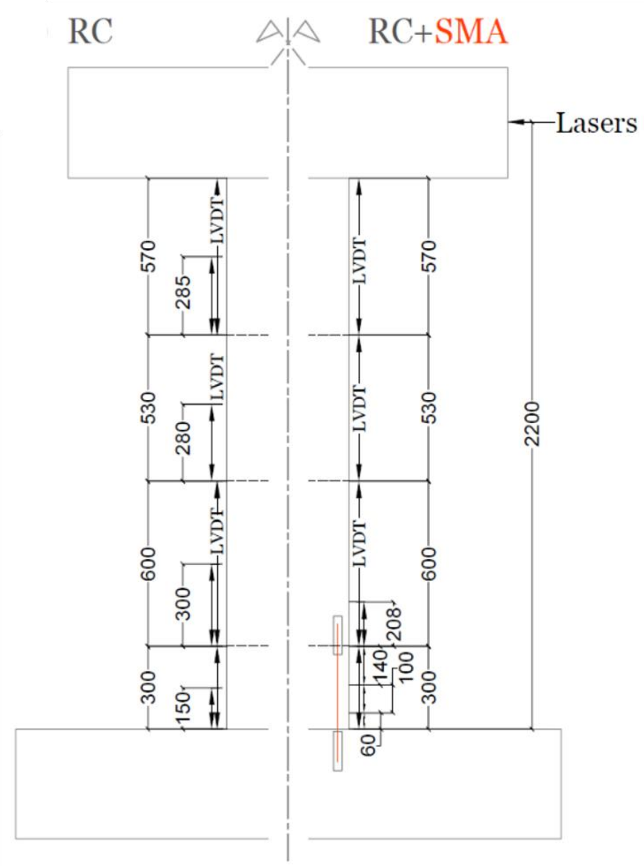

Figure 15 Instrumentation with LVDTs and the laser measurement position.

In view of the instrumentation channels, the acquisition rate of the RC wall test was 0.5 Hz, which was then optimised for the RC+SMA test to 0.33 Hz. Opposite to the horizontal actuator, on the west side of the wall, two laser distance measurers were used to control the top beam's horizontal displacement. It must finally be mentioned that two losses of acquisition occurred during the test of the RC wall: (i) measurements were not saved from LS30 to LS31; (ii) part of the conventional measurements (horizontal lasers not included) were also not recorded from LS37 to LS41.

Digital Image Correlation (DIC) is an optical method of measurement that employs tracking and image comparison methods. It is often used in plan stress strain deformation experiments as it can provide local and average data.

During the experiments, four 12-megapixel cameras were used to capture high quality images of the walls during all the load stages. Those images were later analyzed and compared to each other with the software *"ISTRA 4D ®"* to obtain various pieces of information, such as the local stress and deformation, the exact location and opening of cracks, the vertical elongation of the walls…
The first step to use the DIC is to cover or paint the subject with a speckle pattern as illustrated in Figure 16. The purpose is to have a more accurate comparison between two pictures by making it easier for the software to detect subtle changes. The DIC method tracks the movement of the speckle pattern during the experiment. This is done by analyzing the displacement of the pattern within subsets of the whole image between two consecutive pictures.

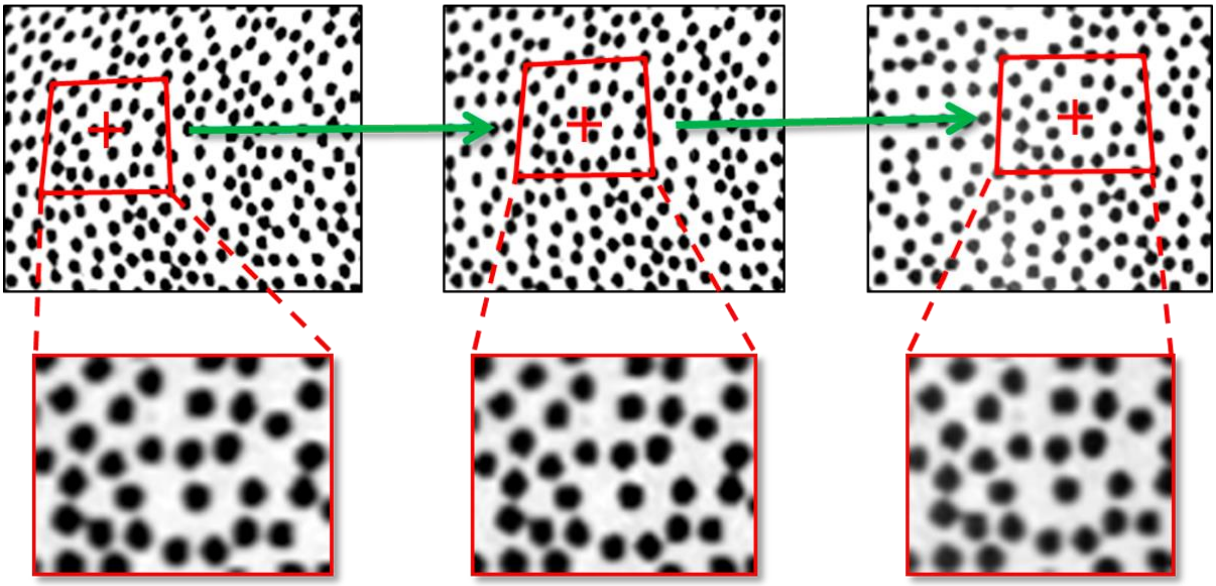

Figure 16 The DIC uses speckle pattern to detect differences between two pictures

During the test, DIC was applied to the south side of each wall for the RC test unit, the bottom region along a height of 1250 mm was monitored as shown in Figure 17, whereas for the RC+SMA wall the camera location was optimized and the DIC system captured the whole height of the wall unit.

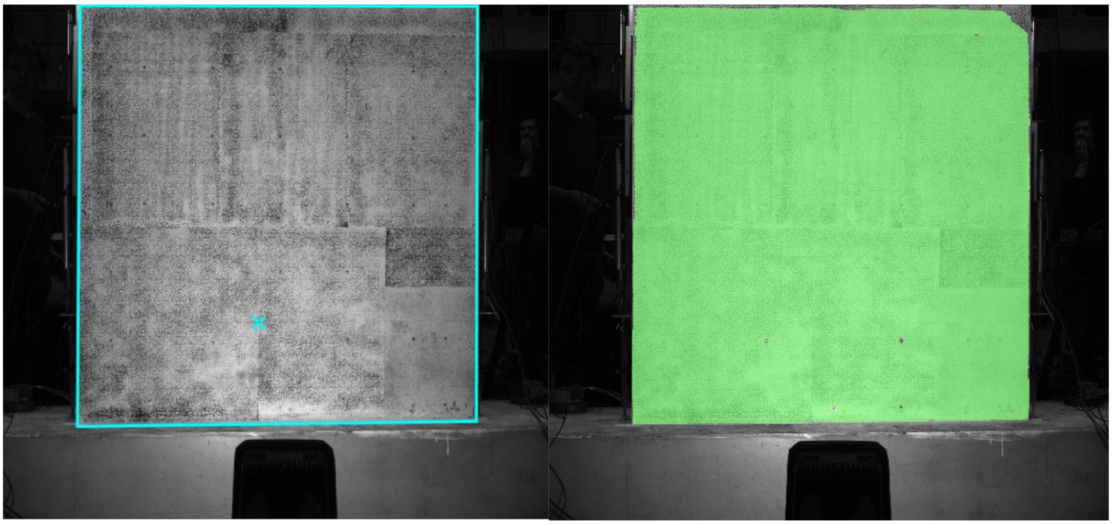

Figure 17 Picture of the RC wall with the speckle pattern, from afar the wall look grey due to the small distance between dots and a picture of the wall after first results.

3 Test results

This section addresses a general description of the several important aspects of the experimental response of the two units tested, together with an interpretation and discussion. First, it exposes the behaviour of both walls during the test, the hysteretic responses, important steps, deformations and failure modes. It follows with cracking, damage progression, and curvature comparison between the two walls. This comparison is used to highlight one of the uses of the DIC. In section 3.1.3, comparisons are made between the numerical simulations and the results are discussed. Finally, section 3.2 analyzes and discusses the most relevant indicators to assess the benefit of adding SMA rebars to increase the seismic performance of RC walls. As the RC wall shows a non-ductile behaviour accompanied by a premature fragile failure, the comparison is made cautiously up to peak strength of the RC wall, in absolute terms regarding the RC+SMA wall alone, along with other literature results.

3.1 Experimental response

3.1.1 Hysteretic response, deformation and failure modes

Figure 18 Close-ups on the base of both units: at the end of the test (LS47) for RC wall (right), and the failure (LS51) for RC+SMA wall that occurred at 0.9% (left).

The in-plane force-displacement responses of the two units, as found from the experimental tests, are depicted in Figure 19, Figure 20 and Figure 21. Considering first the response of the RC wall, one can observe a stable hysteretic response up to the specimen peak force. A lateral force capacity of -146.5 kN was attained at a drift of -0.74 %, corresponding to a horizontal displacement of -16.18 mm (LS30). A positive capacity of 145.89 kN was attained at a drift of 0.9 % (LS33). For imposed drifts beyond the aforementioned values, only the wall base crack width kept increasing, pointing to a concentration of deformations inside the foundation. While loading from -0.9 % to 0.9 % (i.e., from LS34 to LS35), a loud “explosive” noise was heard, corresponding to the formation of a large foundation cone together with likely rebar failure in the foundation. This foundation cone can be observed in Figure 18.

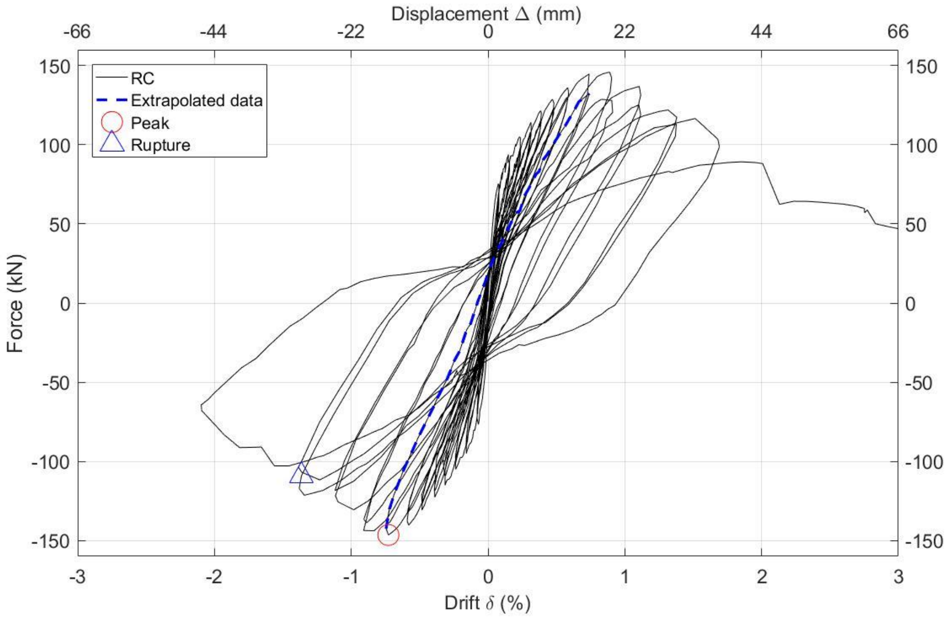

Figure 19 Experimental force-displacement responses of the RC wall.

This failure, which took place at a drift near 0.9 %, was accompanied by a sudden increase of the base crack width (at the tip of the cone) and a small reduction of the above cracks' widths. Subsequent loading cycles reported hysteretic dissipation thinner than usual for RC members, indicative of a restrained spread of plasticity. During loading towards LS41, at a drift of 1.37 % (i.e., at a lateral displacement of 30.2 mm), the sound of two additional rebar ruptures was perceived. The corresponding drop in resistance (see Figure 19) was apparent during the second cycle at the same value of drift (LS43), at which the resistance of the RC wall was 112.9 kN. Such value verifies the criterion of 20% reduction with respect to the member capacity, which is commonly accepted as definition of failure. The rupture of the RC wall was therefore highly premature when compared to well-designed and detailed RC members, which explains the significant difference between the initially predicted force-displacement response from numerical simulations and the experimentally measured response, evidenced in Figure 25 and discussed later in section 3.1.3.

The test continued until the wall lost up to 70% of its maximum strength (see Figure 18), along which five clear rebar rupture sounds were heard (two while pushing towards positive drifts, three during negative drifts). The reasons for the much-reduced ductility capacity of the wall can be explained by a combination of (i) low reinforcement ratio in the wall boundary regions, (ii) lower-than-usual ductility of the employed steel rebars (it is recalled that nominal B-class steel was employed), and (iii) the relatively thin unit foundation block, which allowed the main base crack to dive into the foundation as well as for wall-perpendicular cracks to spread from very early stages (starting from LS07 and LS08, i.e. 0.16% and -0.16% drift). It is noted that the non-recorded data between LS30 and LS31, as discussed in the previous section, was extrapolated (based on the experimental data obtained from LS32 to LS33) and appears in Figure 19 with a dashed blue line.

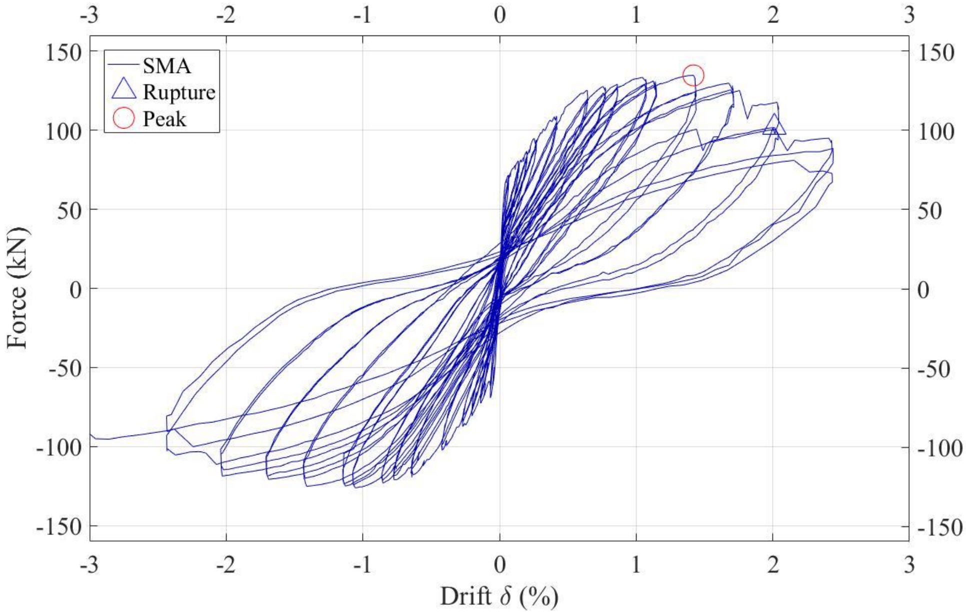

Figure 20 Experimental force-displacement responses of the SMA wall.

The RC+SMA wall showed a more favorable response than initially predicted by the finite element model, as highlighted later in Figure 26. Although the expected flag-shaped force-displacement hysteretic response can be observed in Figure 20, a larger-than-predicted displacement ductility capacity was attained, and bulkier energy-dissipation cycles could also be noticed. The performance was also much superior to the RC wall, but this comparison should be done with care since the latter did not perform in the expected ductile manner.

A maximum lateral strength of 134.7 kN was obtained for the RC+SMA wall at LS41, for a positive drift of 1.42 % (31.5 mm). The unit reached a maximum negative capacity of -126.9 kN at a drift of -1.06 %, immediately before attaining LS34. While progressing to a drift of 2.03 % (LS49) all LVDTs on the west extremity of the specimen – except the two upper ones – fell after a steel rebar fracture sound (occurring at an imposed displacement of 40 mm), which caused the drop in strength visible in Figure 20. This steel rupture was eventually mixed with slipping of the SMA rebar in the coupler. The 20% reduction with respect to the member capacity was attained at the second cycle at the same drift value (2.03 %, LS51), corresponding to a resisting force of 101.7 kN. While loading towards this load stage, at an imposed displacement of 32.2 mm, a new clear rebar fracture sound was distinctly heard, which is also reflected by a strength drop in Figure 20.

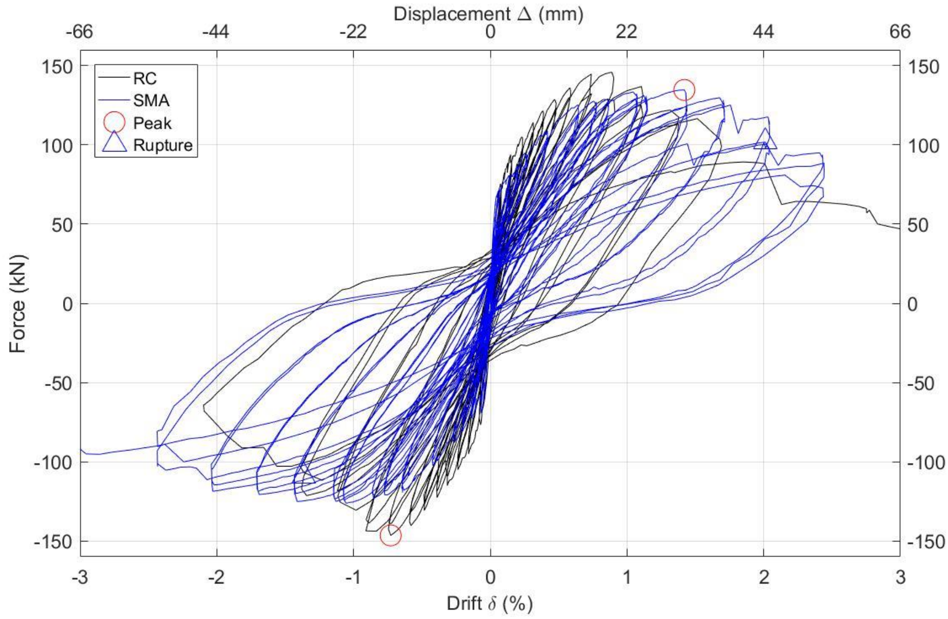

Figure 21 Experimental force-displacement responses of the two test units.

3.1.2 Cracking and damage progression

This section presents and discusses the differences regarding the progression of damage and crack patterns between both units, including the evolution of curvature demands with drift. The first observation relates to the development of a nearly-horizontal crack pattern along the entire wall height, both for the RC wall and the RC+SMA wall. This is apparent in Figure 22, which shows the comparison between the vertical strains for both units at drifts around 0.45 %, 0.9 %, and 1.4 %, attesting to the predominantly flexural behaviour of the units, as expected from the large applied shear span ratio (equal to 3.6). The strain maps at the walls' surface were obtained from digital image correlation (DIC), as mentioned above.

Focusing on the RC wall, the horizontal cracks appeared from LS01 and quickly spread throughout the height of the wall, attaining at a drift of 0.24 % (LS09) their approximate final spacing. The first vertical splitting crack in the RC wall tension side also appeared at LS09. The initial compression crushing cracks occurred when loading to a drift of -1.11 % (LS38) in the lower corner of the wall. As the previous load stage closely precedes the drift at failure (1.37 %), and as concrete crushing is a progressive phenomenon, it is estimated that the minor losses of concrete cover that may have occurred before failure were largely compensated by an increase in confinement of the boundary element. Therefore, concrete crushing did not contribute to the drop in lateral strength and failure was hence entirely due to rebar failure in the foundation. The effects of the foundation failure can be observed by comparing Figure 22(b) and Figure 22(c), where a reduction of the crack widths at the tensile extremity of the wall, particularly at the bottom, is accompanied by the appearance of a large foundation crack (not monitored by the DIC system but visible in the image).

Regarding the RC+SMA wall, the initial crack development was substantially different from the RC unit. At the first load stages, horizontal cracks appeared, the largest of which at the wall base. Up to LS16, there was only a couple of hairline cracks above the couplers' position, up to a height of 1590 mm. Between LS16 and LS17, i.e. while loading from a drift of -0.27 % to 0.42 %, a thud was heard with spread cracking (5 new cracks) suddenly appearing throughout the height of the west side of the wall. While loading to the next target drift (-0.42 %, LS18), 4 new cracks also appeared on the unit east side. Loading from -0.64 % to 0.77 % (LS24 to LS25) and from 0.77 % to -0.77 % (LS25 to LS26) gave rise to the first compression crushing cracks on both sides at the wall base. These cracks eventually led to concrete spalling while loading towards a positive drift of 1.14 % (LS39) and a negative drift of -1.42 % (LS42). For larger imposed displacements, similarly to the RC wall and as initially designed, deformations concentrated in bottom wall cracks. This expected response indicates the activation of the superelastic SMA rebar behaviour while the stress in the steel rebars above the couplers remained below the yield stress, according to the capacity design principles employed and referred in Section 2.1. Cracks at the bottom of the RC+SMA wall were not symmetrical: when loading towards negative values of drift, a major crack formed at the wall-foundation interface, whereas, while loading to positive drifts, the deformation was distributed between two bottom cracks, one at the interface and another approximately 8 cm above, see Figure 22(f). The first evidence of concrete crushing, obtained from the appearance of vertical compressive cracks, occurred at slightly lower drifts compared to the RC wall, namely while loading from a drift of 0.77 % to -0.77 % (i.e., from LS25 to LS26). Therefore, and unlike its RC counterpart, the progressive concrete crushing that kept developing until the drift at failure (2.03 %) likely contributed to the degradation of the RC+SMA wall strength.

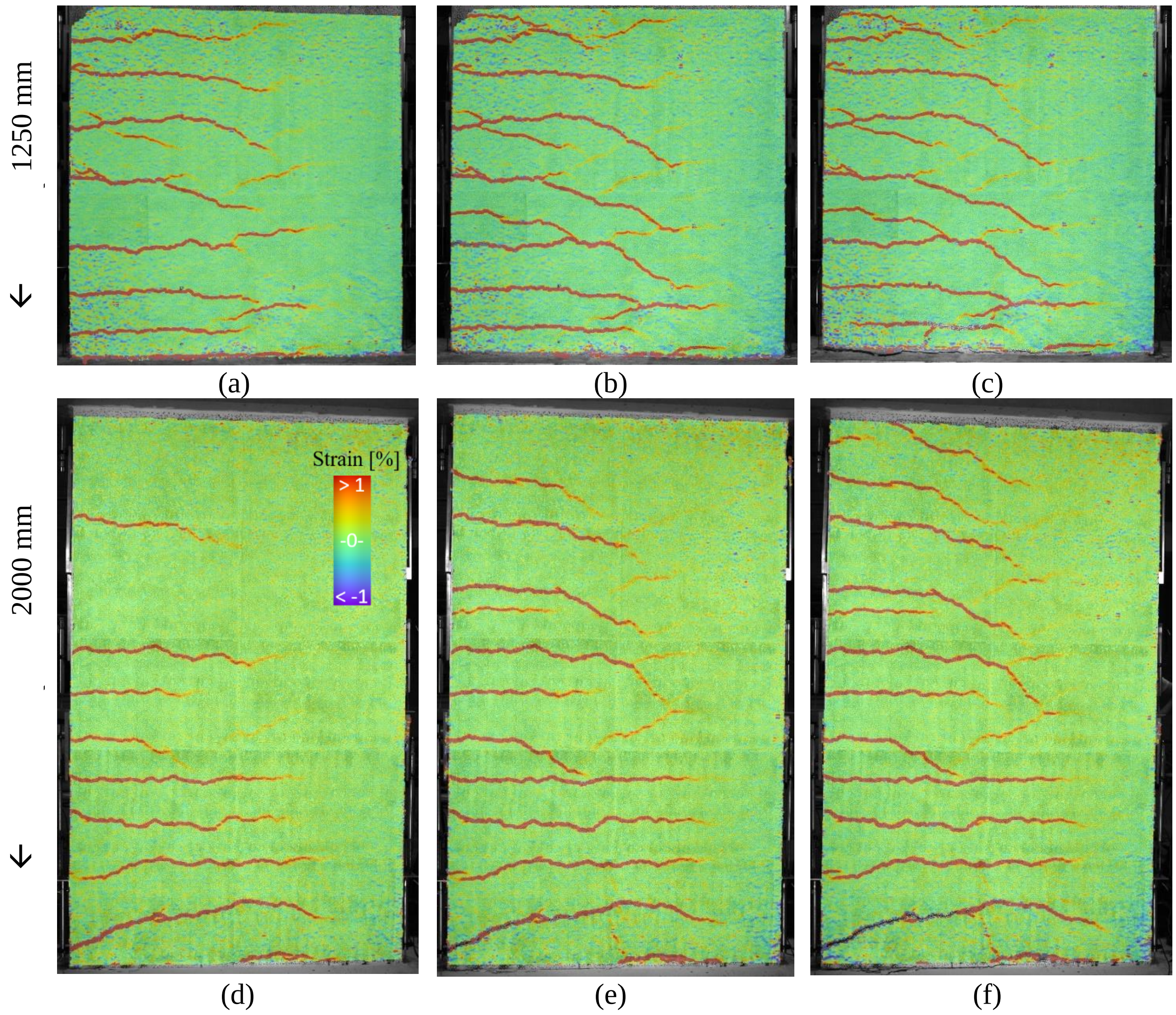

Figure 22 Vertical strains as obtained from digital image correlation for the RC wall at positive drifts of (a) 0.48 %, LS 21 (b) 0.9%, LS 33, and (c) 1.37%, LS 41, and for the RC+SMA wall at (d) 0.42%, LS 17 (e) 0.86 %, LS 29, and (c) 1.42%, LS 41.

Figure 24 shows the curvature profiles along the height for both walls at the same values of drift (around 0.45 %, 0.9 %, and 1.4 %). These profiles were calculated from a mesh of virtual displacement gauges aligned vertically at both extremities of the wall in the DIC software. Each gauge is 10 cm long (h). Once a wall has been subject to deformations, the length of the virtual gauges varies accordingly, and the local curvature (φ) is calculated as such:

$$\frac{h_1 - h_2}{L} = \tan(\theta) \cong \theta$$

$$\varphi = \frac{\theta}{h}$$

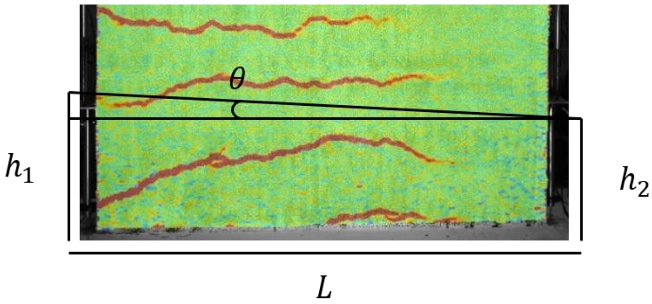

Figure 23 Local wall curvature: example.

with h_1, h_2 the new lengths of the corresponding gauges of each side and L the length of the base of the walls.

A comparison and a validation of the DIC results with those from the actual chains of LVDTs (see Figure 15) was also performed. The base curvature was derived from measurements of LVDTs at the bottom of the wall, since the DIC could not accurately capture the cracks at the wall-foundation interface. The upper half of the RC wall curvatures was also derived from physical LVDT measurements. The profiles in Figure 24 show a similar progression of curvatures for both walls, with a large concentration in the first few unit bottom centimeters. Such a profile was the desired response for the RC+SMA wall, where the previous concentration of curvature demand in the bottom SMA rebar region occurred up to the failure drift and beyond. For the RC wall, the inelastic curvature demand should have extended up the height of the wall, instead of concentrating at the base, in order to enable a larger displacement ductility capacity. The inability to do so, previously discussed, inevitably led to a premature non-ductile failure. Figure 24 also depicts the estimate of the yield curvature ϕ_y (represented with a vertical dashed line) for the corner of the equivalent bilinear approximation, as proposed by Priestley et al. (2007). It is computed as $\phi_y = 2.0\varepsilon_y/l_w$, where $\varepsilon_y = 0.0025$ is the yield strain and $l_w = 1200$ mm is the wall length.

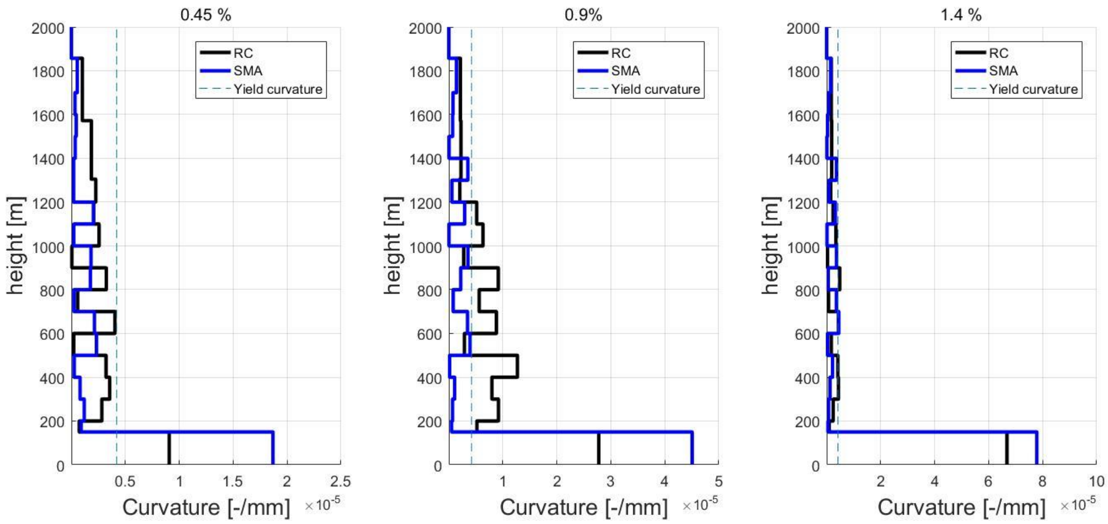

(a) (b) (c)

Figure 24 . Curvature profile along the wall height for both units at the following drifts: (a) 0.45%, (b) 0.9%, and (c) 1.4%.

3.1.3 Comparison with results from numerical simulations

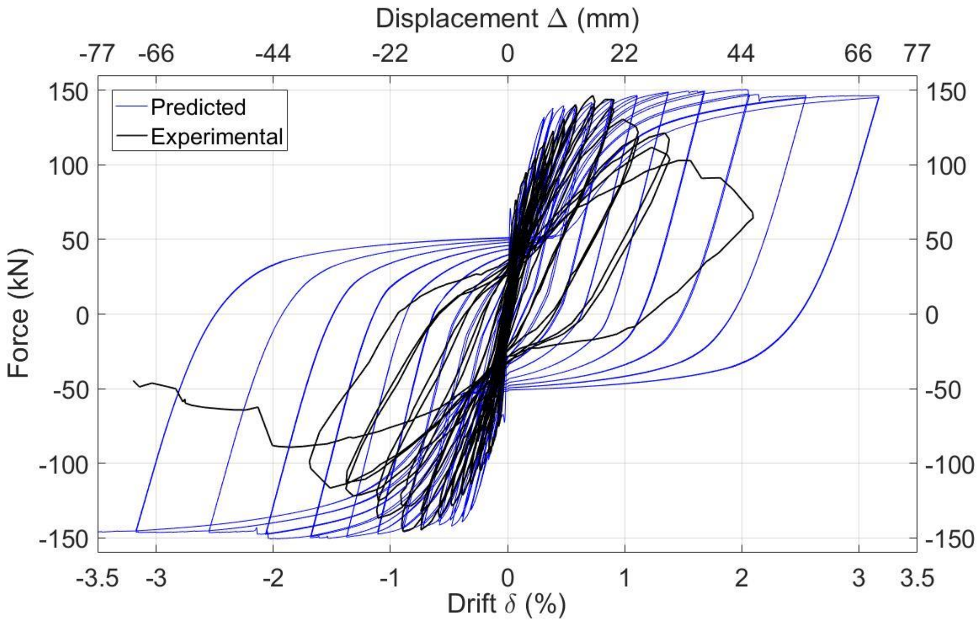

Figure 25 Force-displacement response of the test units as predicted by the finite element model: RC wall.

Finite element models developed with the software *Opensees* (F. McKenna, 2000) have been employed to estimate the response of the walls before the tests. Two axially equilibrated displacement-based elements have been used to model the walls and the expected bilinearization of curvature along the height for inelastic loading (D. Tarquini, 2017).The sectional response took into account the confined boundary regions through fibre discretization and confinement factors. Common *OpenSees* uniaxial cyclic models for concrete (*Concrete04*) and steel (*Steel02*) were assigned, whose parameters were defined from the material test results. A similar approach was used to simulate the SMA rebars, but since the specific *OpenSees* SMA uniaxial model could not be found, an alternative material model *SelfCentering* was used. In order to simulate the capacity of the assembly composed of the couplers and the rebars, as tested experimentally, the SMA material strength was defined to reproduce the tensile capacity of the assembly (68 kN) in place of the SMA rebar strength. Complete details regarding the numerical simulations can be found in the work of Herrezeel et al. (2019).

Figure 25 and Figure 26 show the force-displacement curves obtained with the finite element model and compare them with the experimentally measured wall responses. The large discrepancy of the RC wall stands out in terms of displacement ductility, which was discussed in the previous sections. On the other hand, an overall acceptable estimate is obtained for the RC+SMA wall, despite the inability of the model to predict residual displacements.

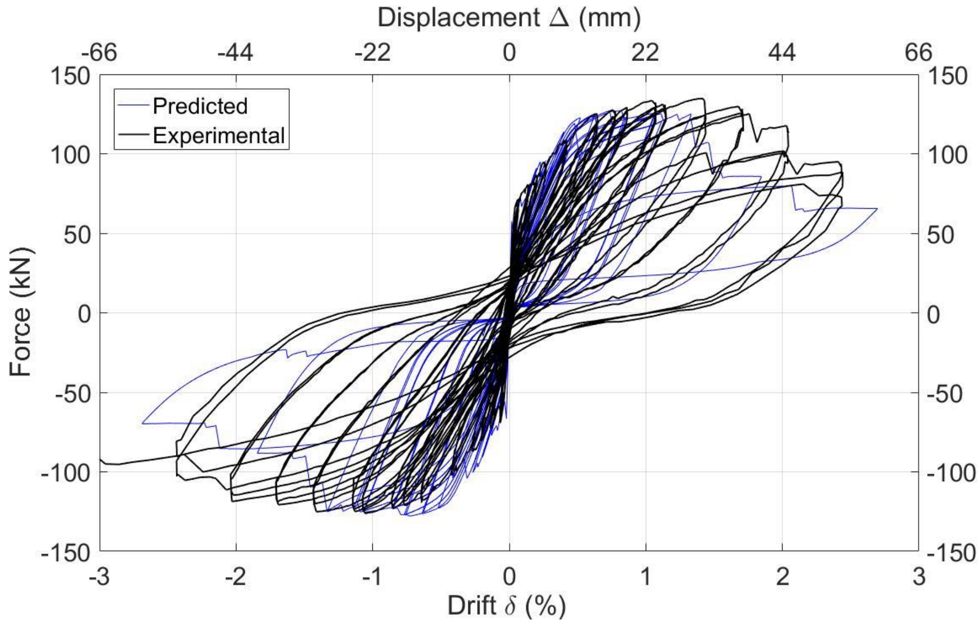

Figure 26 Force-displacement response of the test units as predicted by the finite element model: SMA wall.

3.2 Response analysis

This section analyses and discusses the most relevant indicators to assess the benefit of adding SMA rebars to increase the seismic performance of RC walls. As the RC wall showed a non-ductile behaviour accompanied by a premature fragile failure, the comparison is performed cautiously up to peak strength of the RC wall, in absolute terms regarding the RC+SMA wall alone, and in comparison, with other literature results.

3.2.1 Residual lateral displacement

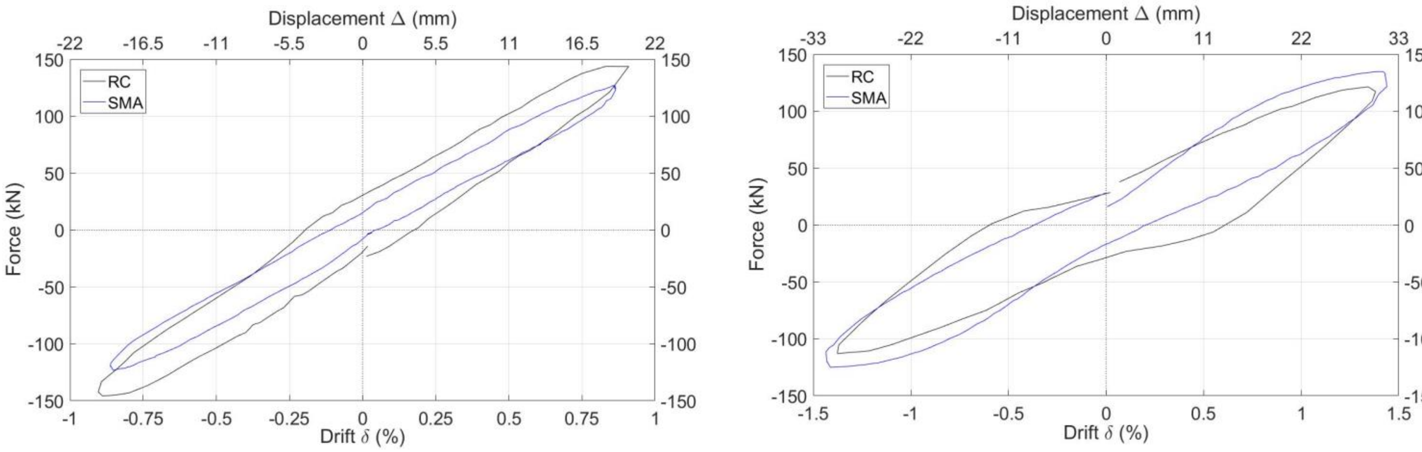

(a) (b)

Figure 27 Complete cycle of the force-displacement response for both walls, in between similar levels of imposed drift: (a) RC: +/-0.9 % and RC+SMA: +/- 0.87 % (b) RC: +/-1.37 % and RC+SMA: +/- 1.42 %.

As discussed in the introduction, the improved self-centring ability of the wall RC+SMA (with respect to the reference RC unit) is a fundamental feature for the reduction of damage and repair costs after an earthquake. Figure 27(a) displays the cycle of the force-displacement response of the RC unit between the zero-drift preceding an imposed drift of 0.9 % and the zero-drift when unloading from the following imposed drift of -0.9 %. In the same graph, the analogous cycle of the response for the RC+SMA wall, between load stages with similar levels of imposed displacements, is overlapped. Figure 27(b) is an analogous graph for the last two load stages corresponding to the failure for the RC wall. From these graphs, the reduction in the residual displacement, after similar imposed peaks of lateral displacements, is clearly apparent for the unit with SMA rebars. Additionally, this decrease is clearly more significant for displacement levels imposing larger levels of inelasticity in the wall units.

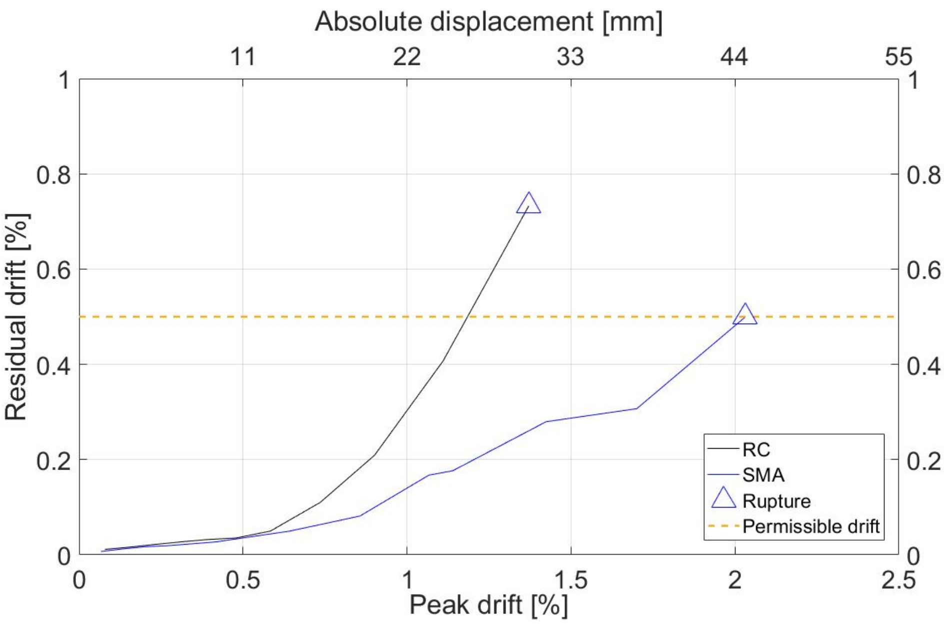

Figure 28 Residual drift versus imposed lateral drift for both units.

In order to quantify and compare this reduction throughout the entire response, Figure 28 shows the evolution of the residual lateral drift, Δ_{res}, as a function of the imposed peak lateral drift, Δ_{peak}, for both walls. Figure 29 shows the displacement recovery capacity, defined as $(\Delta_{peak} - \Delta_{res})/\Delta_{peak}$. It is noted that the plotted results were derived from averaging the absolute value of the peak and residual displacements at each set of four load stages at the same imposed lateral drift. Several conclusions can be drawn. First, it appears that the behaviour during the initial cycles up to a drift of around 0.6% is similar for both walls, which had also been observed by Kian and Noguez (2018) for approximately similar values of drift. Therefore, the influence of SMA rebars in minimizing residual displacements for low-intensity ground motions can be relatively minor. Beyond 0.6%, the self-centring features of the SMA rebars show up clearly in the wall response: in fact, for the peak drift corresponding to the failure of the RC wall (i.e., around 1.4 %), the residual drift of the RC+SMA unit is around 35 % of the residual drift of the RC wall. In other words, the unit with the smart alloy rebars is able to recover 80% of the imposed peak displacement, while the recovery is smaller than 50 % for the RC unit. The tests by Kian and Noguez (2018) also confirm these findings, pointing out the efficiency of this self-centring technique for medium and high-intensity ground motions.

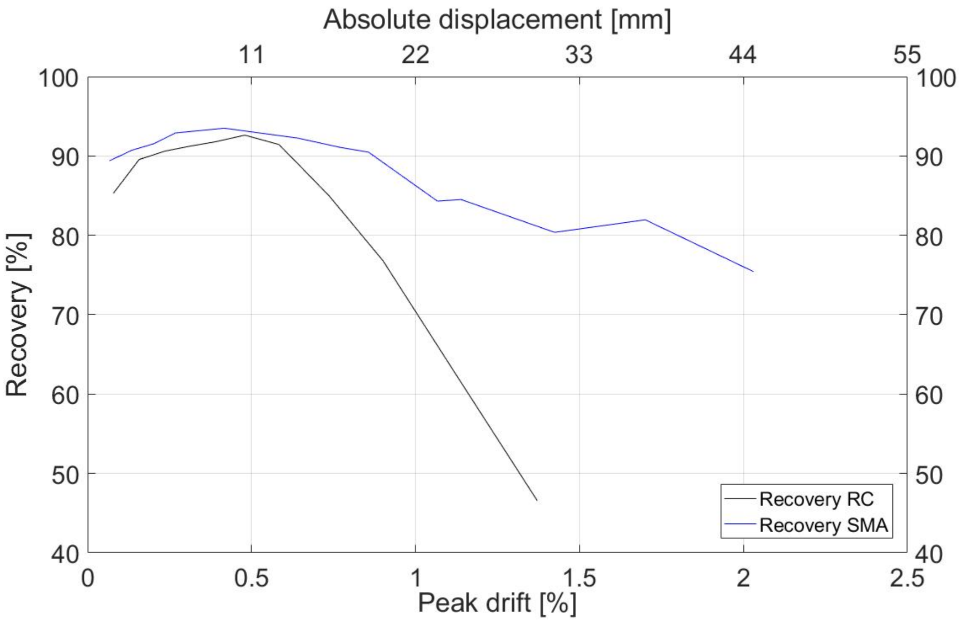

Figure 29 Displacement recovery capacity versus imposed lateral drift for both units.

Trying to extend the comparisons with other self-centring systems, such as the post-tensioned wall systems, is not straightforward. In fact, with these techniques, the residual displacement strongly depends on the type of energy-dissipating system adopted (K.M. Twigden, 2019). It is also interesting to note that, for the permissible residual drift level of 0.005 rad (roughly 0.5 % drift) suggested by McCormick et al. (2008) and mentioned in the introduction, a maximum drift of 2 % can be imposed to the RC+SMA wall, which compares to a much-reduced drift of 1.19 % for the RC unit. The unit failure coincided with the attainment of the above permissible residual drift.

3.2.2 Vertical elongation

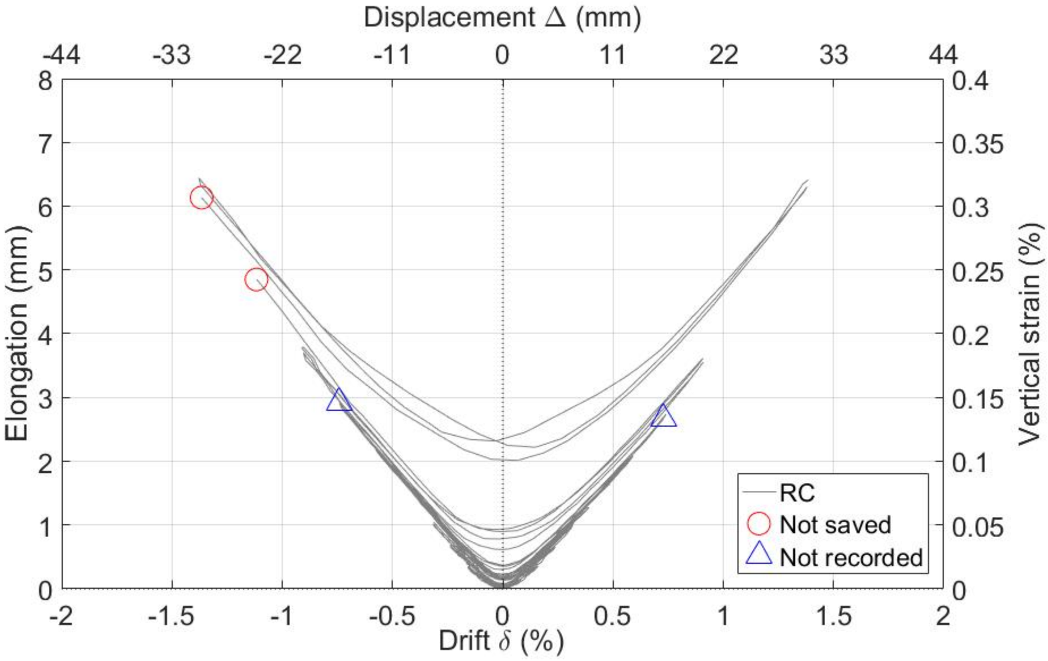

Figure 30 Evolution of vertical elongation and strain with applied drift for the RC wall.

The lateral residual drift is not the only measure of post-earthquake damage that can be obtained from a quasi-static cyclic test. The vertical elongation of RC members subjected to inelastic response due to the shift of the neutral axis is a well-known effect and should also be investigated, both regarding its maximum attained values as well as the residual value. This effect, which is sometimes neglected, can cause problems particularly if accompanied by differential elongations between distinct vertical members (e.g. shear walls and gravity columns). Such demands can crack and damage the connecting horizontal members (e.g. slabs and beams) and affect the post-earthquake serviceability of the structure.

The evolution of the vertical elongation with the imposed cyclic drift is shown in Figure 30 and Figure 31 where the results are also plotted in terms of vertical strain. The vertical elongation is computed as the average of the vertical displacements at both (west and east) ends of the wall. the vertical displacements of each side is the sum of each chain of LVDTs. The loss of data for the RC and RC+SMA walls, discussed in Section 3, is also indicated. The response is very similar for both units except when unloading and reloading from load stages larger than around 0.75 % drift (in absolute value), as discussed below.

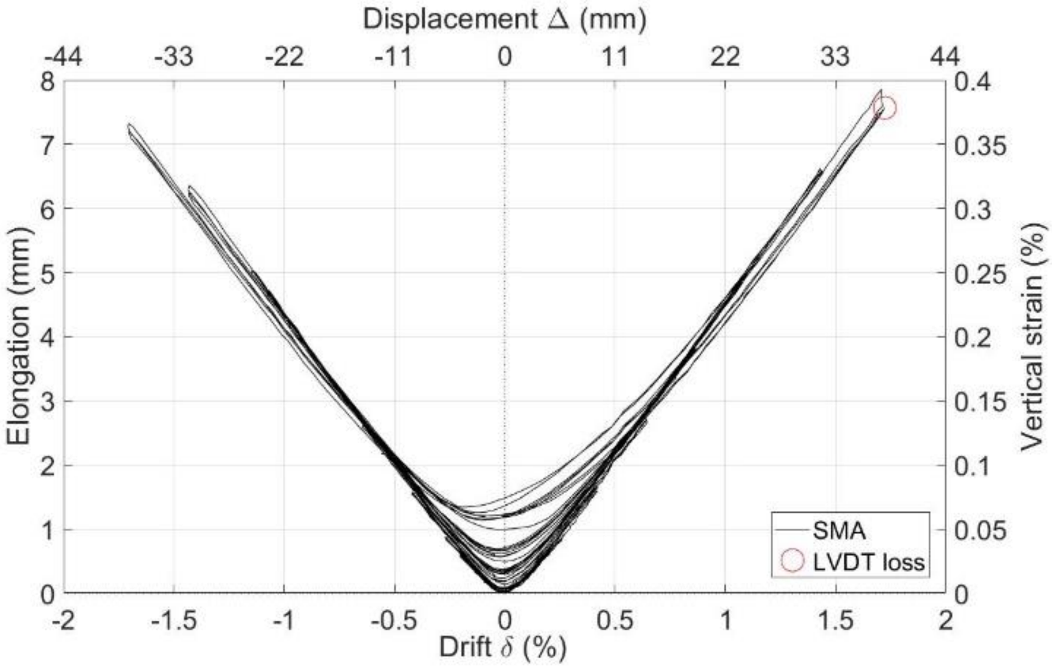

Figure 31 Evolution of vertical elongation and strain with applied drift for the SMA wall.

The previous comment can be made clearer with Figure 32 and Figure 33. Figure 32 depicts the maximum vertical elongation attained at each imposed drift, whereas Figure 33 plots the residual vertical elongation in between two load stages (i.e., when the horizontal force is zero). For both figures, the results are obtained by averaging the absolute values of the peak and residual displacements from each set of four load stages at the same imposed lateral drift. Although the maximum vertical elongation of the RC+SMA unit is consistently slightly larger than the RC wall (19 % higher for a drift of around 1.37 %, corresponding to the failure of the RC specimen), as shown in Figure 32, conversely the residual vertical elongation is smaller as Figure 33 points out. This desirable feature, which attains a significant reduction (approximately 50 % less for a drift of around 1.37 %), appears to be an additional advantage of this new technological approach to wall design with traditional RC construction. Such important aspect has not yet been put in evidence in the literature.

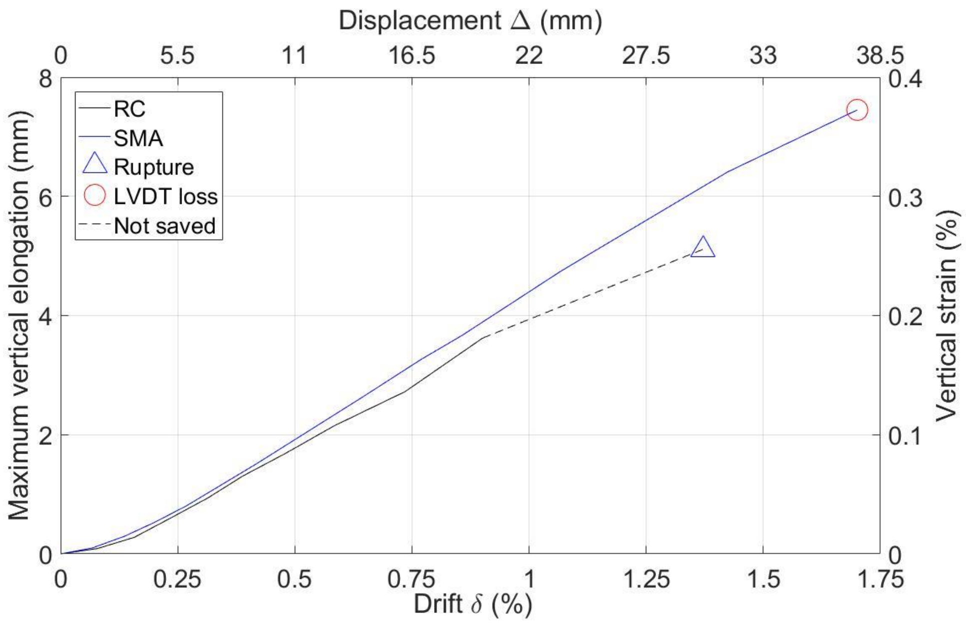

Figure 32 Relation between (maximum) vertical elongation and imposed lateral displacement.

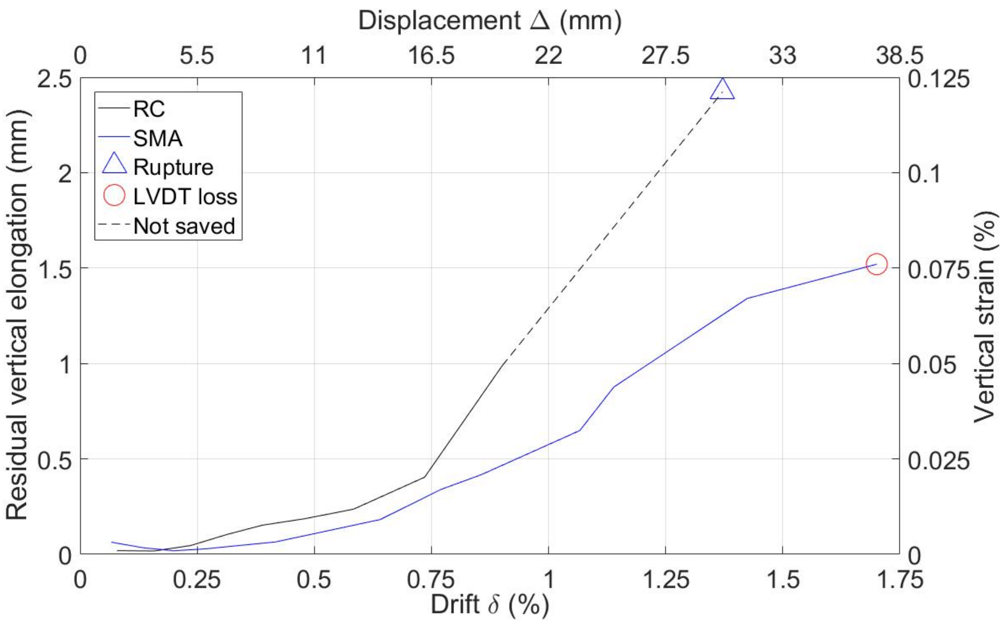

Figure 33 Residual vertical elongation and strain (i.e., when applied horizontal force unloads to zero), both for the RC wall and the RC+SMA wall.

3.2.3 Energy dissipation

This paragraph addresses the behaviour of both walls considering the energy dissipation, which is summarized in Figure 34. This shows that the difference between the dissipation energy curves is minor. For an imposed drift of 1.4%, the RC wall dissipated 15.6 % more energy than the RC+SMA unit. In comparison, Abdulridha and Palermo (2017) report a 34 % average larger energy dissipation of the RC+SMA wall with respect to the RC unit, whereas Kian and Noguez (2018) report an increase of around 70 % at 3.3 % drift. The difference between the present results and the two aforementioned studies can be explained by the poorly ductile behaviour of the RC wall test in the present study, as thoroughly discussed above, which also prevents the comparison to extend over a larger range of drifts. This seemingly favourable comparison in terms of energy dissipation is hence artificial, although Figure 34 unequivocally shows that the hysteretic cycles are encouragingly plump. In terms of absolute value of dissipated energy by the RC+SMA unit, the wall tested in the present study is comparable in magnitude with the values reported by the other studies. A more detailed comparison would need to take into account the specific geometric characteristics and reinforcement detailing, as well as loading features of the different tests.

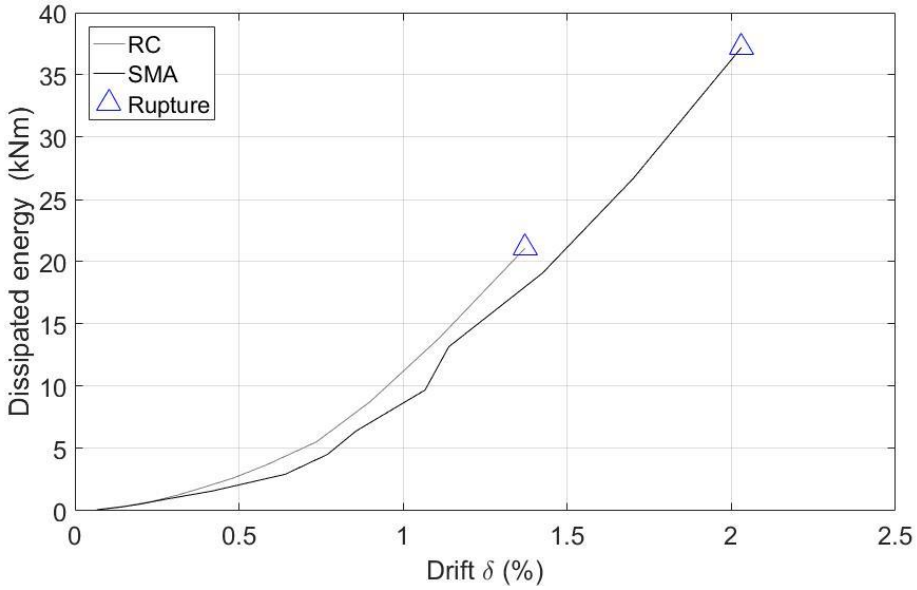

Figure 34 Energy dissipated by the RC and RC+SMA walls with applied drift.

3.3 Residual Vertical strains

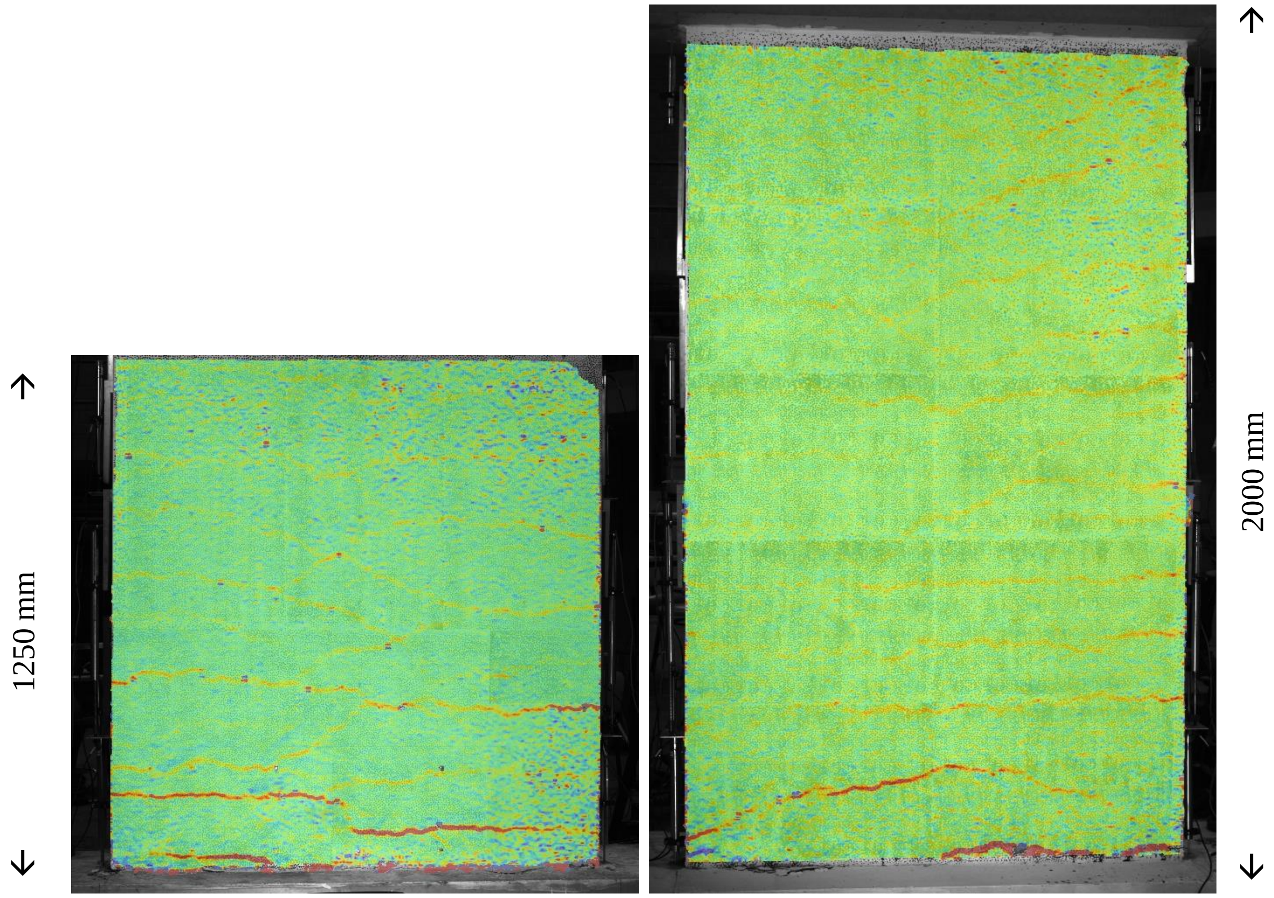

Figure 35 Map of wall surface vertical strains at zero-force upon load reversal from the following imposed drift levels: (a) 1.37% RC wall and (b) 1.42%, RC+SMA wall.

Strain maps and crack patterns upon force removal are the most direct and reliable indication of residual post-earthquake damage. But this paragraph will not go into detail.

Figure 35 plots the residual surface vertical strains upon unloading from imposed drift levels corresponding to the failure of the RC wall unit (around 1.4 %), as obtained from the DIC system. The differences between the two walls are not significant in view of the unexpected deformation and failure mode of the RC unit. In a ductile-behaving RC wall, a distributed cracking along the unit height would show up, which would be further accentuated for strain residuals from larger imposed drifts. On the other hand, the concentration of deformations at the base of the RC+SMA wall was anticipated and it qualitatively corroborates the results of other studies (A. Abdulridha, 2017) (M.J.T. Kian, 2018). Note that the foundation-wall base interface crack cannot be accurately monitored by the DIC system.

4 Mechanical model

From this section starts the second part of this thesis. As mentioned in the introduction, the second objective of this thesis was to adapt an existing mechanical model for boundary elements of RC walls to RC wall with SMA rebars.

At the beginning of this section, the tension chord model (Marti P, 1998) on which the mechanical model (D. Taquini, 2019) is based is briefly explained. The main assumptions and theoretical aspects underlying the tension chord model are summarized. Next, the mechanical model is detailed along with the different composing elements and its implementation. This section is greatly inspired by the article (D. Taquini, 2019).

4.1 Tension chord model

The original tension chord model (Marti P, 1998) was originally developed for addressing problems of cracking, tension stiffening in RC members subjected to uniaxial loading.

Figure 36(a) shows a reinforced concrete wall boundary element with a longitudinal rebars of a diameter ϕ_l and an area of $A_s = \pi\phi_l^2/4$. The gross sectional area is equal to A_t with a longitudinal reinforcement ratio of $\rho_l = A_s/A_t$.

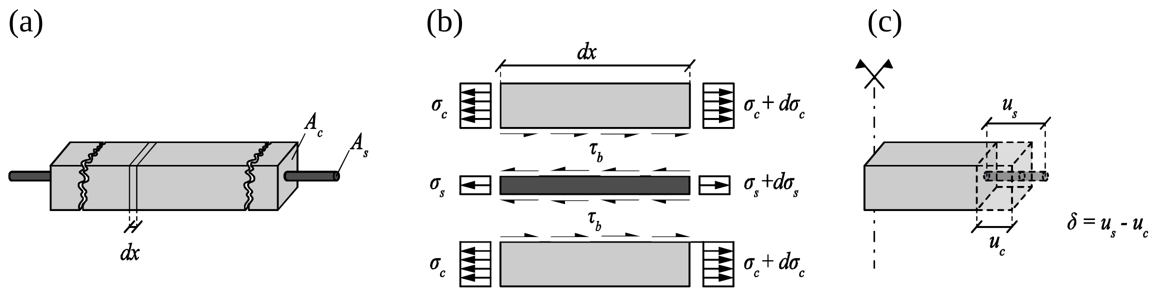

Figure 36 (a) Sketch of a basic tension chord element, i.e. the portion of tension chord between two cracks; (b) Concrete and steel equilibrium for an infinitesimal length dx; (c) Compatibility requirements. Adapted from (Marti P, 1998)

Considering an infinitesimal length of dx (see Figure 36(b)), the equilibrium equation can be written as such:

$$\frac{d\sigma_c}{dx} = -\frac{\tau_b \cdot \pi \cdot \emptyset_l}{A_t \cdot (1-\rho_l)} \quad (1)$$

$$\frac{d\sigma_s}{dx} = \frac{4 \cdot \tau_b}{\emptyset_l} \quad (2)$$

where σ_c and σ_s are the concrete and steel stresses and τ_b is the bond stress.

From the strain-displacement relations, we can deduce:

- $\varepsilon_s = du_s/dx$
- $\varepsilon_c = du_c/dx$

where u_s and u_c are the steel and concrete displacements, as shown in Figure 34(c), and ε_s and ε_c are the corresponding strains. From the previous equations, the steel-concrete slip δ can be calculated as the difference between the concrete and the steel displacement:

$$\delta = u_s - u_c \tag{3}$$

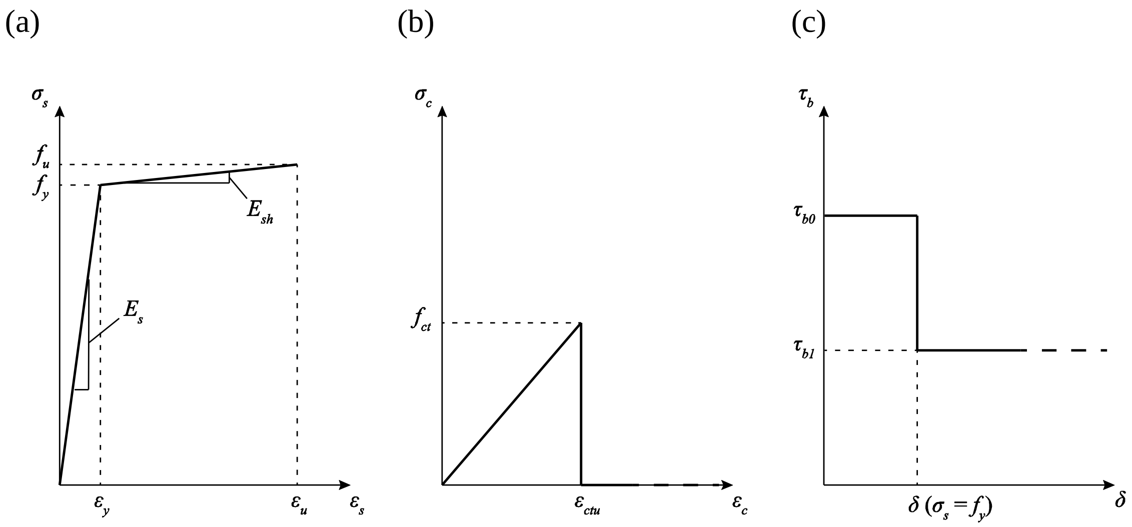

Figure 37 Constitutive relations employed in the extended tension chord model: (a) Bilinear steel stress-strain law; (b) Concrete tensile stress-strain behavior; (c) Steel-concrete bond-slip relationship. (D. Taquini, 2019)

Using the assumption that the stress-strain law for the concrete is linear and that the steel stress-strain law is bi-linear (Figure 37 (a) and (b)) and by combining the previous equation, we can obtain:

$$\frac{d^2\delta}{dx^2} = \frac{4 \cdot \tau_b}{{d\sigma_s}/{dx} \cdot \emptyset_l} + \frac{\tau_b \cdot \pi \cdot \emptyset_l}{A_t \cdot E_c \cdot (1 - \rho_l)} \tag{4}$$

E_c and ${d\sigma_s}/{dx}$ are the young modulus of the concrete and the steel. ${d\sigma_s}/{dx}$, in the bilinear model, can take two values: E_s and E_{sh} which correspond to the pre- and post-yield stress young modulus as show in Figure 37 (a).

Equation (4) can be integrated if the bond slip law is known. Figure 38(a) shows an experimental steel-concrete bond slip response along with the approximation done by Shima et al. (1987). Figure 38(b) illustrates the approximation done by Marti (1998). In this approximation, the bond slip law is assumed to be stepped and rigid-perfectly-plastic. This form is particularly convenient for the integration of Equation (4). As consequence, in a basic tension chord element (the portion between two consecutive cracks of the tension chord), the steel stress distribution can be derived without the need to deal with a complex numerical integration of the equation (4). The concrete stress, the concrete and steel strain, the crack width and the elongation can also be derived from the equilibrium conditions.

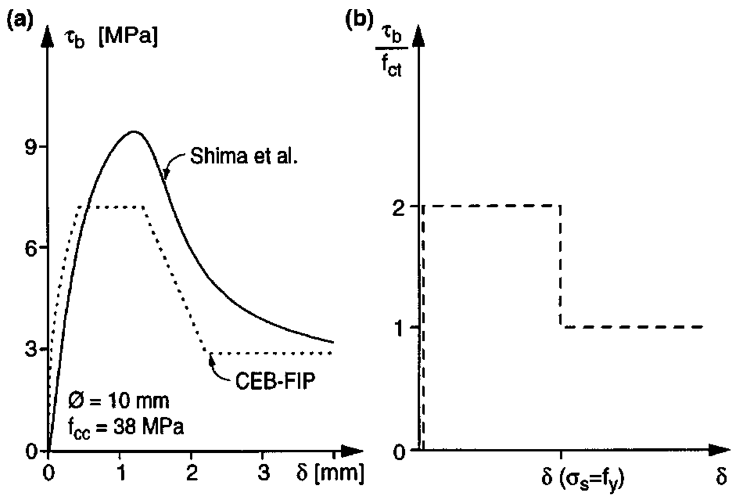

Figure 38 Bond shear stress-slip models: (a) Shima et al. (1987) and CEB-FIP (1993); (b) tension chord model (Marti P, 1998) Tension chord element subject to different displacements

4.2 Tension chord subject to different level of imposed displacement.

Figure 39 (a) shows a qualitative steel and concrete strain distribution of a tension chord of length L_0 subjected to increasing imposed displacements Δ. This section discusses the different possible scenarios.

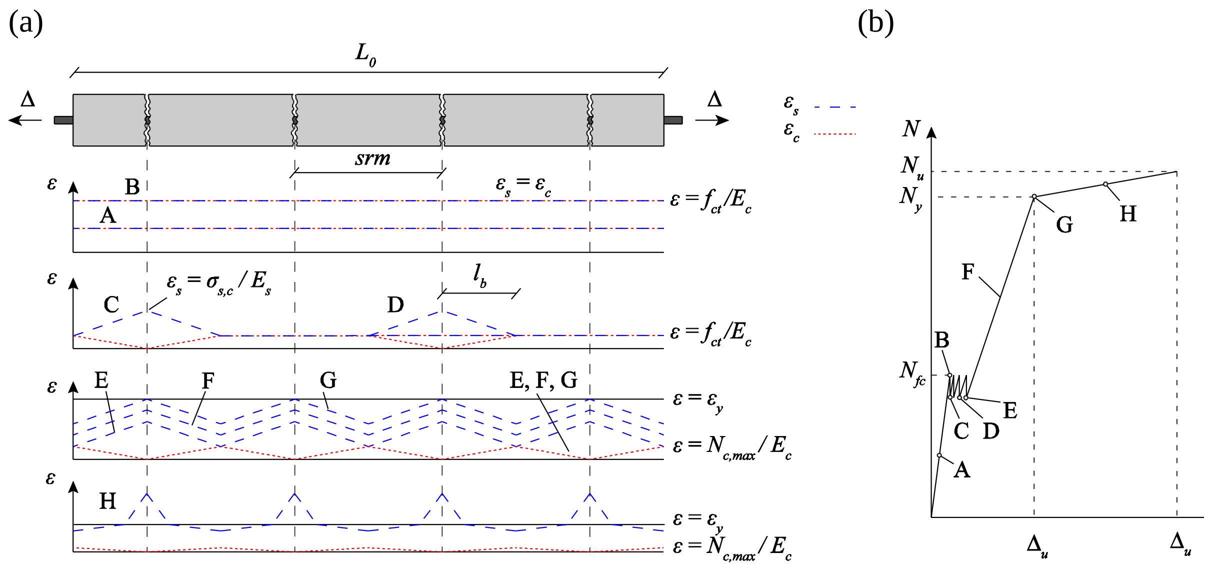

Figure 39 from (D. Taquini, 2019): Tension chord subjected to increasing imposed displacements: (a) Force-displacement response; (b) Qualitative steel and concrete strain distributions.

Before the first crack, no slip between the concrete and the steel occurs. This means that they share the same state of deformation, which corresponds to state A in Figure 39. The axial stiffness of the axial member can be computed as the sum of the stiffness of the concrete and the steel:

$$\frac{(EA)_{equiv.}}{L_0} = \frac{(E_c \cdot A_c + E_s \cdot A_s)}{L_0} \qquad (5)$$

where $A_c = A_t - A_s$ is the concrete area.

State B from Figure 39 is the limit state just before the appearance of the first crack. The first crack takes place when the concrete is subject to the tensile stress f_{ct}, which occurs when the following force is applied:

$$N_{fc} = \frac{(EA)_{equiv.} \cdot f_{ct}}{E_c} \tag{6}$$

When the first crack takes place, the stress and strain of the concrete are both equal to zero (state C in Figure 39(a)). the whole force is taken up by the steel. The steel stress goes from a pre-crack $\sigma_{s,B}$ to a post-crack stress $\sigma_{s,C}$. Assuming the rebar is still in the elastic phase, they can be expressed as:

$$\sigma_{s,B} = \frac{E_s \cdot f_{ct}}{E_c} \tag{7}$$

$$\sigma_{s,C} = \frac{N_{fc}}{A_s} \tag{8}$$

Cracks occur one after another if larger deformations are imposed (see state D in Figure 39 (a)), up until crack stabilization. This stabilization corresponds to the state in which a large imposed force does not generate new crack but the existing cracks are widening as shown by states E, F and G in Figure 39(a). The distance between two cracks *srm* is bounded by $l_b \leq srm \leq 2l_b$ where l_b is the minimum length required to transfer the difference between steel forces in the pre- and post-crack states from the steel to the concrete through bond action.

$$l_b = \frac{\emptyset_l \cdot \left(\sigma_{s,C} - \sigma_{s,B}\right)}{4 \cdot \tau_{b0}} = \frac{\emptyset_l \cdot f_{ct} \cdot (1 - \rho_l)}{4 \cdot \rho_l \cdot \tau_{b0}} \tag{9}$$

If two cracks appear at a distance greater than $2l_b$, the distance is enough to transmit a force greater than N_{fc} from the rebar to the concrete through bond action and create a new crack. In the opposite case, i.e. if the *srm* is smaller than l_b, the force transmitted to the concrete is smaller than N_{fc} and new cracks cannot appear. In this thesis, similarly to Tarquini et al (2019), the intermediate value of $srm = 1.5 \cdot l_b$ is assumed.

The maximum force applied to the concrete can be calculated, depending on the *srm*, as:

$$N_{c,max} = \frac{srm}{2} \cdot \tau_{b0} \cdot \emptyset_l \cdot \pi \tag{10}$$

Solving analytically equation (4) between two cracks, the steel and concrete strain and stress can be obtained. The crack width can be obtained by calculating the integral, along *srm*, of the difference between the steel and concrete strains:

$$w = \int_{-\frac{srm}{2}}^{\frac{srm}{2}} \varepsilon_s - \varepsilon_c \, dx \tag{11}$$

The total elongation of a basic tension chord can be obtained by integrating the steel strain:

$$\Delta_{TC} = \int_{-\frac{srm}{2}}^{\frac{srm}{2}} \varepsilon_s \, dx \tag{12}$$

4.3 Elements composing the model

The model developed by Tarquini et al (2019) is based on the classical model described in the previous section (Marti P, 1998) and is briefly explained here. The mechanical model proposed developed the classical model and adapt it to different situation by making different element base on the classic tension chord model. These elements represent one section between two cracks (*srm*) for different cases such as an anchorage-slip element, a lap-splice element or the simple tension chord element. For each element, it is possible to calculate the crack width and the total elongation (equation (11) and (12)). The model takes different types of elements and places them in series to match a boundary element of an RC wall. From that, the model can predict all cracks width and position, the concrete and steel strains of a RC wall.

4.3.1 Anchorage-slip element

The anchorage-slip element is the first element used in this model. Its purpose is to estimate the anchorage-slip displacement Δ_{anc} and the concrete and steel strain distribution along the anchorage length l_{anc} .

$$\Delta_{anc} = \int_{l_{anc}}^{0} \varepsilon_s \, dx \tag{13}$$

This element is designed to only apply to anchorage with a length l_{anc} longer than the length required to achieve the ultimate steel stress (l_{ult}).

$$l_{ult} = l_y + l_p = \frac{f_y \cdot \phi_l}{4 \cdot \tau_{b0}} + \frac{(f_u - f_y) \cdot \phi_l}{4 \cdot \tau_{b1}} \tag{14}$$

with l_y the elastic and l_p the plastic components and with f_y and f_u the steel yield and ultimate strength.

$$\Delta_{anc} = \begin{cases} \dfrac{\varepsilon_{ac}}{2} \cdot l_{ac} & for \quad \varepsilon_{ac} < \varepsilon_y \\ \dfrac{\varepsilon_y}{2} \cdot l_y + \dfrac{\varepsilon_y + \varepsilon_{ac}}{2} \cdot (l_{ac} - l_y) & for \quad \varepsilon_{ac} > \varepsilon_y \end{cases} \tag{15}$$

The previous equations (15) are illustrated in Figure 40. They depicted two cases pre- and post-yield cases.

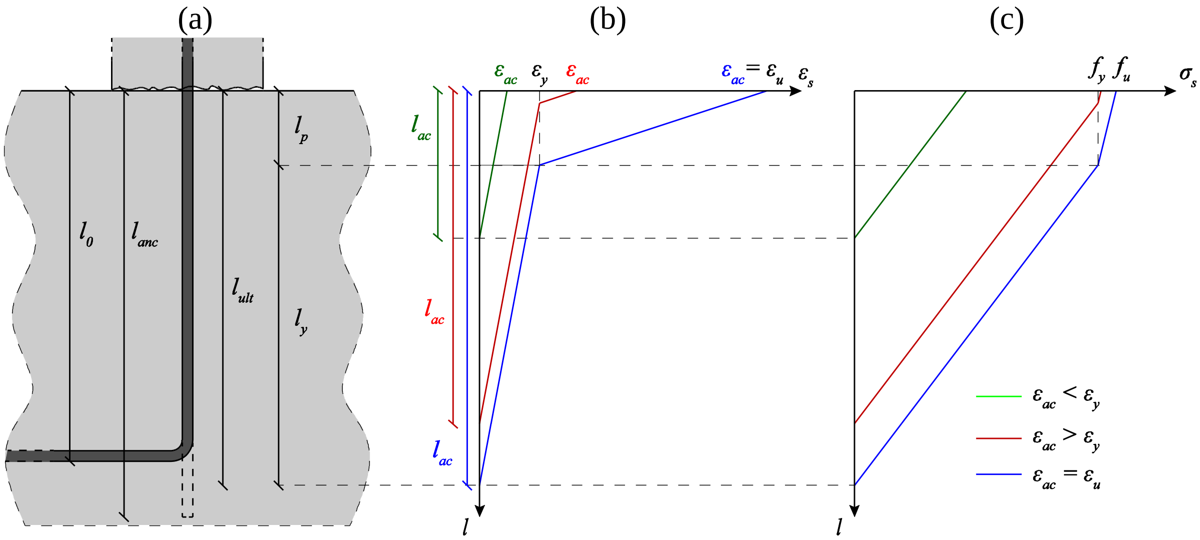

Figure 40 (D. Taquini, 2019) Anchorage-slip element for bent anchored bars with lanc>lult: (a) Sketch of the anchorage detail; (b) Qualitative steel strain profiles; (b) Qualitative steel stress profiles.

Equation (15) gives the analytical expression for the anchorage-slip displacement if $l_{anc} > l_{ul}$. For reaching the strain at crack ε_{ac}, a certain length l_{ac} is required and is computed as :

$$l_{ac} = \begin{cases} \dfrac{\varepsilon_{ac} \cdot E_s \cdot \phi_l}{4 \cdot \tau_{b0}} & for \quad \varepsilon_{ac} < \varepsilon_y \\ \dfrac{f_y \cdot \phi_l}{4 \cdot \tau_{b0}} + \dfrac{(\varepsilon_{ac} - \varepsilon_y) \cdot E_{sh} \cdot \phi_l}{4 \cdot \tau_{b1}} & for \quad \varepsilon_{ac} > \varepsilon_y \end{cases} \tag{16}$$

4.3.2 Basic tension chord element

As described in section 4.2, the basic tension chord element represents the portion between two consecutive cracks of a tension chord (spaced *srm* apart). For an arbitrary value of the steel strain at crack ε_{ac} between ε_{cs} the steel strain at crack stabilization and ε_{ac} the steel ultimate strain ($\varepsilon_{cs} < \varepsilon_{ac} < \varepsilon_{ult}$), the steel and concrete stress and strain can be derived from the equilibrium conditions. By resolving Equation (11) and Equation (12), the crack width and the total elongation of the element can be determined. Three cases can be distinguished:

1. $\varepsilon_{ac} < \varepsilon_y$: the steel is in an elastic state.
2. $\varepsilon_{ac} > \varepsilon_y$ and $l_{ac,p} < srm/2$: the rebar is parsley in an elastic and in a plastic state.
3. $\varepsilon_{ac} > \varepsilon_y$ and $l_{ac,p} > srm/2$: the steel is in a plastic state.

with $l_{ac,p}$ the length required to develop the plastic strain $\varepsilon_p = \varepsilon_{ac} - \varepsilon_y$ (Figure 41)

$$l_{ac,p} = \frac{A_s \cdot E_{sh} \cdot (\varepsilon_{ac} - \varepsilon_y)}{\tau_{b1} \cdot \pi \cdot \phi_l} \tag{17}$$

For each of the 3 cases, Equations (18) and (19) give the expression of the crack width. The elongation is derived from Equations (11) and (12):

$$\Delta_{TC} = \begin{cases} \left(\varepsilon_{ac} - \dfrac{N_{c,max}}{2 \cdot A_s \cdot E_s}\right) \cdot srm & for\ case\ (1) \\ \varepsilon_{ac} \cdot l_{ac,p} + \varepsilon_y \cdot \dfrac{srm}{2} + \varepsilon_{srm/2} \cdot \left(\dfrac{srm}{2} - l_{ac,p}\right) & for\ case\ (2) \\ \left(\varepsilon_{ac} - \dfrac{N_{c,max,p}}{2 \cdot A_s \cdot E_{sh}}\right) \cdot srm & for\ case\ (3) \end{cases} \tag{18}$$

$$w = \begin{cases} \left(\varepsilon_{ac} - \dfrac{N_{c,max}}{2 \cdot A_s \cdot E_s} - \dfrac{N_{c,max}}{2 \cdot A_c \cdot E_c}\right) \cdot srm & for\ case\ (1) \\ \Delta_{TC}^{case(2)} - \varepsilon_{c,y} \cdot \dfrac{srm}{2} - \varepsilon_{c,srm/2} \cdot \left(\dfrac{srm}{2} - l_{ac,p}\right) & for\ case\ (2) \\ \left(\varepsilon_{ac} - \dfrac{N_{c,max,p}}{2 \cdot A_s \cdot E_{sh}} - \dfrac{N_{c,max,p}}{2 \cdot A_c \cdot E_c}\right) \cdot srm & for\ case\ (3) \end{cases} \tag{19}$$

Where:

- $\varepsilon_{srm/2}$ and $\varepsilon_{c,srm/2}$ are the steel and concrete strains at *srm/2*.
- $\varepsilon_{c,y}$ is the concrete strain corresponding to the yield point.
- $N_{c,max,p}$ is the maximum concrete force occurring at *srm/2*.

$$\varepsilon_{srm/2} = \varepsilon_y - \frac{\tau_{b0} \cdot \pi \cdot \phi_l \cdot \left(\dfrac{srm}{2} - l_{ac,p}\right)}{A_s \cdot E_s} \tag{20}$$

$$\varepsilon_{c,srm/2} = \varepsilon_{c,y} + \frac{\tau_{b0} \cdot \pi \cdot \phi_l \cdot \left(\dfrac{srm}{2} - l_{ac,p}\right)}{A_c \cdot E_c} \tag{21}$$

$$\varepsilon_{c,y} = \frac{\tau_{b1} \cdot \pi \cdot \phi_l \cdot l_{ac,p}}{A_c \cdot E_c} \tag{22}$$

$$N_{c,max,p} = \sigma_{c,max,p} \cdot A_c = \frac{srm}{2} \cdot \tau_{b1} \cdot \emptyset_l \cdot \pi \tag{23}$$

The basic tension chord element is illustrated in Figure 41. The material stress and strain distribution are depicted for each case.

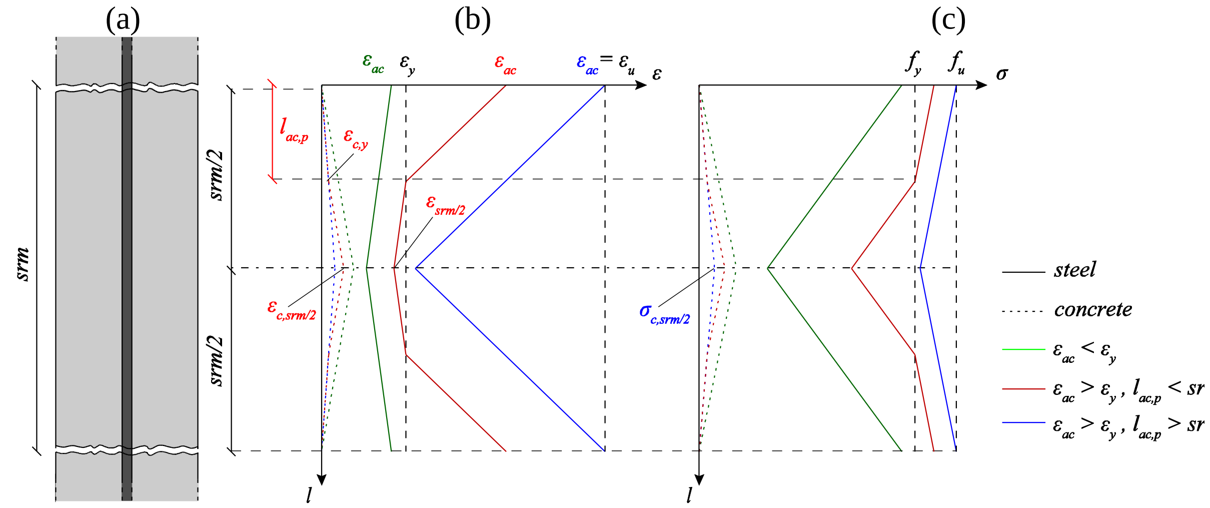

Figure 41 (D. Taquini, 2019)): Basic tension chord element: (a) Sketch; (b) Qualitative steel and concrete strain profile; (b) Qualitative steel and concrete stress profile.

4.3.3 Lap-splice element

A big part in the study done in Tarquini et al (2019) focuses on the influence of lap splices in RC walls. More often, lap-splices are found above the foundation level, the more solicitated part during a seismic activity. As the two previous elements, a third one was developed specially for the lap-splices regions. It is worth mentioning the existence of this element, but it will not be developed here because it will not be used in the adaptation of the model.

4.4 Model implementation

Section 4.4 presents an iterative solution using the model to obtain the local deformation and forces for an imposed global displacement.

The model can predict the RC wall response given the materials properties and the global top displacement Δ_{tot} imposed on a RC wall boundary element with lap splices. The outputs of the model are the resisting axial force, crack spacing and width, steel and concrete strain distributions. To obtain that, the model takes the three previously described elements and connects several of them in series to simulate the response. An example is shown in Figure 42 (a). To predict the response, the model uses an iterative method to resolve the non-linear problem. A flowchart illustrating the iterative method is depicted in Figure 42 (b).

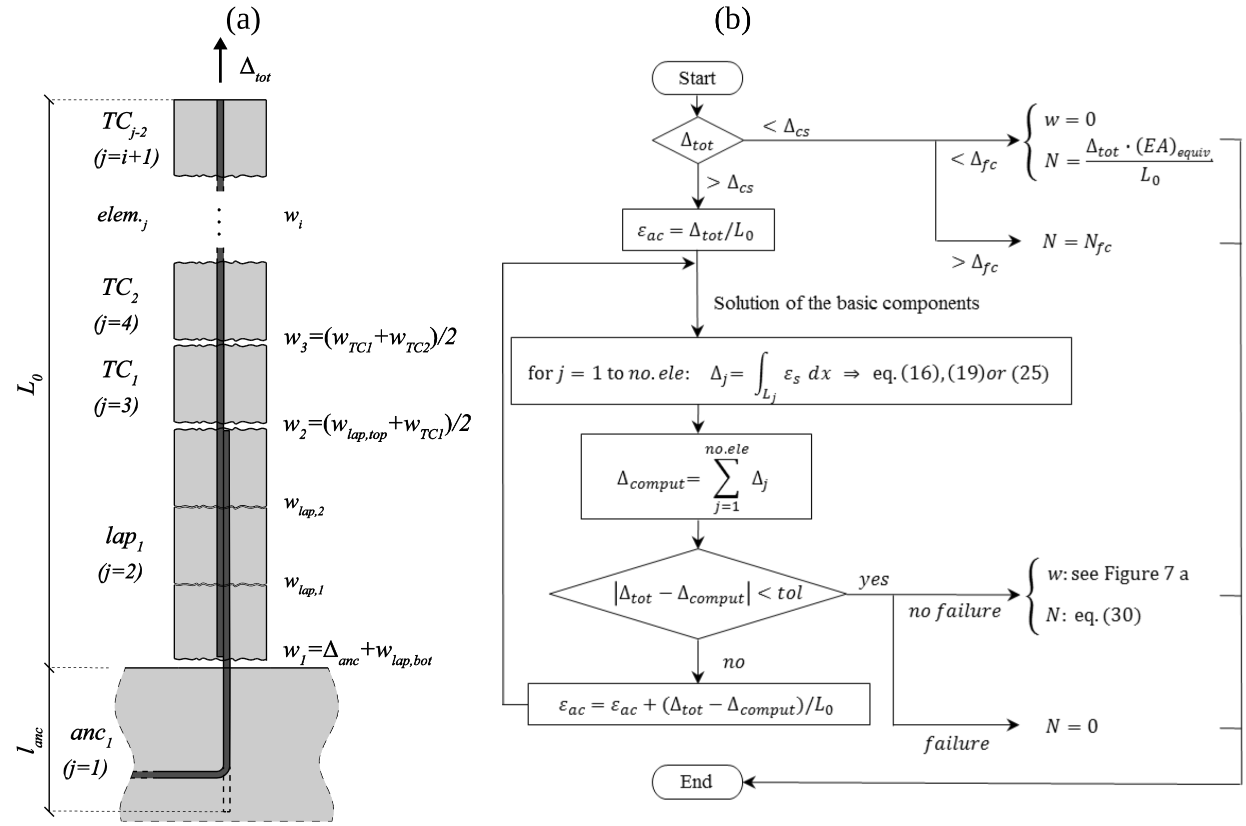

Figure 42 (D. Taquini, 2019) RC boundary element model: (a) Assembly of the components for a RC member featuring lap splice, anchorage, and multiple basic tension chord (TC_i) elements; (b) Flowchart of the iterative procedure.

No crack appears if the force applied is smaller than N_{fc} (see equation (6)), as the bond between the steel and the concrete is unbroken and they share the same strain:

$$\varepsilon_s = \varepsilon_c = \frac{\Delta_{tot}}{L_0} \tag{24}$$

with L_0 the total length of the wall (Figure 42 (a)).

The value of displacement before the first crack Δ_{fc} can be determined from N_{fc}. Once the force reaches a value of N_{fc}, the first crack appears. Up until crack stabilization (*cs*), cracks continue to be created. Between those two states, the force is assumed to be constant and equal to N_{fc}. In reality, it is not the case as it can be seen in Figure 39 (b) from case B to case E: small force drops occur due to the stiffness reduction caused by the opening of each cracks. The steel strain at crack stabilization can be determined by:

$$\varepsilon_{cs} = \frac{N_{fc}}{E_s \cdot A_s} \tag{25}$$

The displacement at crack stabilization Δ_{cs} can easily be calculated based on this value of strain.

To this point, the Δ_{tot} was easily and directly compared by the model to the two values of displacement, Δ_{cs} and Δ_{fc}. As illustrated in Figure 42, the model compares the input value of Δ_{tot} with different values of displacement to predict the response of the wall. If Δ_{tot} is smaller than Δ_{cs}, calculations are direct, and no iteration is needed. For imposed displacements larger than Δ_{cs}, an interactive method is used to resolve the nonlinear problem. Each element can be solved separately for a given strain at crack ε_{ac}. A first evaluation of $\varepsilon_{ac} = \Delta_{tot}/L_0$ is made to start the iterative prosses. The value of ε_{ac} is then recalculated at each iteration. The sum of the elongation of each element (Δ_{comput}), calculated as described in the previous sections, is then compared to the Δ_{tot}. If the difference is smaller than the tolerance (in this case $tol = \Delta_{tot}/1000$ is used), the iterative process is over. Otherwise, the value of ε_{ac} is updated and a new iteration is performed.

5 Model Adaptation

In this section, the modifications made to the previously described model (D. Taquini, 2019) are introduced. First the adaptations made to mechanical model (Marti P, 1998) are presented. Then, the new SMA element, similar to the Anchorage-slip element or the tension chord element, is detailed. Finally, the changes made to the implementation of the model are discussed.

5.1 Mechanical model

The first step to adapt the model was to come back to the basic and modify the mechanical model (Marti P, 1998). The model is initially made for steel and concrete, the purpose here is to adapt it for SMA and concrete.

The equilibrium shown in Figure 43 is still valid independently of the material. The three next equations and the development are nearly identical to the ones listed in the beginning of section 4, but here the steel is replaced by SMA.

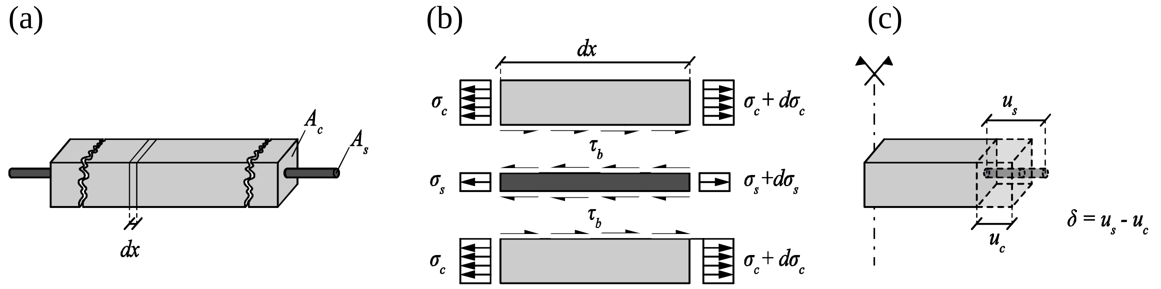

Figure 43 after (Marti P, 1998): (a) Sketch of a basic tension chord element, i.e. the portion of tension chord between two cracks; (b) Concrete and steel equilibrium for an infinitesimal length dx; (c) Compatibility requirements.

Considering an infinitesimal length of *dx* (see Figure 43 (b)), the equilibrium equation can be written as such:

$$\frac{d\sigma_c}{dx} = -\frac{\tau_b \cdot \pi \cdot \emptyset_l}{A_t \cdot (1-\rho_l)} \tag{26}$$

$$\frac{d\sigma_{sma}}{dx} = \frac{4 \cdot \tau_b}{\emptyset_l} \tag{27}$$

here

- σ_c and σ_{sma} are the concrete and SMA stresses and τ_b is the bond stress.
- ϕ_l the diameter of longitudinal SMA rebars with an area of $A_{sma} = \pi\phi_l^2/4$.
- A_t the gross sectional area and $\rho_l = A_{sma}/A_t$ the longitudinal reinforcement ratio.

From the strain-displacement the following relations can be deduced:

- $\varepsilon_{sma} = du_{sma}/dx$
- $\varepsilon_c = du_c/dx$

where u_{sma} and u_c are the SMA and concrete displacements, as shown in Figure 34(c), and ε_{sma} and ε_c are the corresponding strains.

From the previous equations, the SMA concrete slip δ can be calculated as the difference between the concrete and the SMA displacement:

$$\delta = u_{sma} - u_c \tag{28}$$

The first adaptations begin by determining the SMA stress strain law and the SMA-concrete bond slip relationship.

5.1.1 SMA stress strain law

As explained in section 2.2.2, uniaxial monotonic and cyclic tests were carried out on SMA rebars as part of Herrezeel (2019) thesis. The superposition of which is shown in Figure 44.

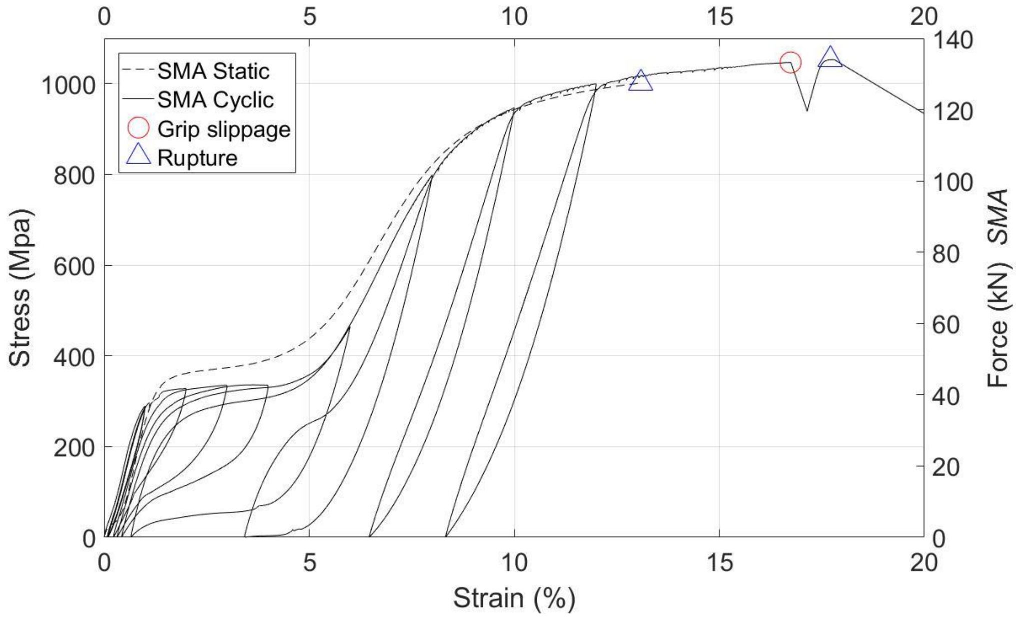

Figure 44 SMA stress strain for monotonic and cyclic tests

In this case, a simplification was made for calculation purpose. Based on the SMA cyclic test, a simplification, composed of three linear assumptions, was made resulting with three different young moduli as shown in Figure 45 and in Table 2.

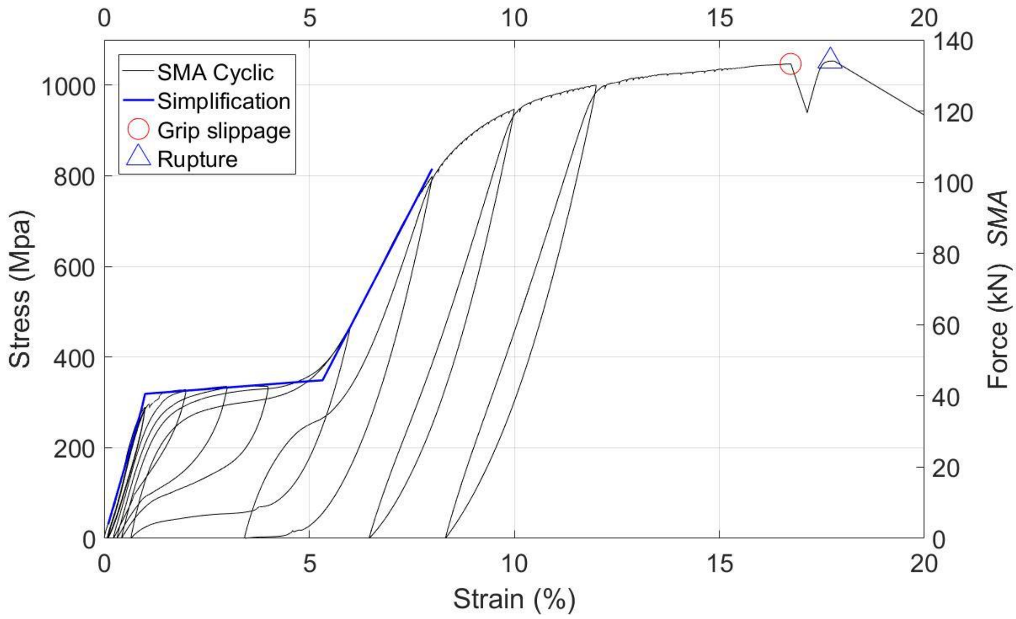

Figure 45 SMA stress strain for cyclic tests and simplification

Material		Properties	Unit	Value
SMA	σ_{AMs}	Austenite to martensite start stress	[MPa]	319
	E_{AMs}	Modulus of elasticity	[GPa]	31,2
	ε_{AMs}	tensile strain	[%]	1
	σ_{AMf}	Austenite to martensite finish stress	[MPa]	349
	E_{AMf}	Modulus of elasticity	[GPa]	0,6
	ε_{AMf}	tensile strain	[%]	5,5
	σ_{nu}	Ultimate tensile strength	[MPa]	1053
	E_{nu}	Modulus of elasticity	[GPa]	17,5
	ε_{nu}	Ultimate tensile strain	[%]	13

Table 2 SMA Properties

5.1.2 SMA-concrete bond slip relationship

Muntasir (2015) investigated the bond law between concrete and SMA rebar trough 56 push out specimens. The purpose was to explore the influence of different parameters (concrete strength, bar diameter, embedment length and surface condition) on the bond stress relation between SMA and concrete. The final purpose of this article was to develop an empirical equation to predict the maximum average bond strength.

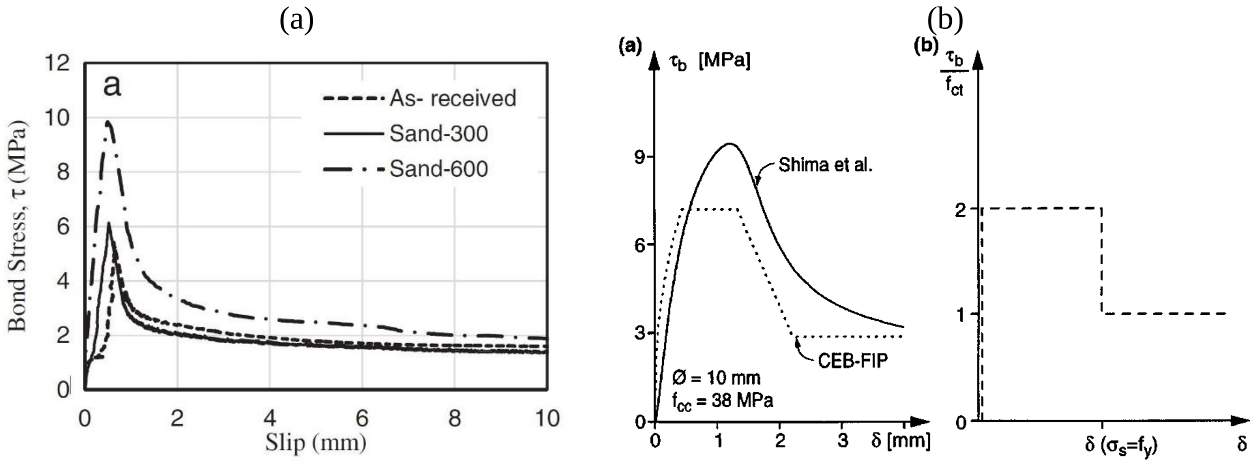

Figure 46 Bond shear stress-slip models: (a) (Muntasir et al. 2015) experimental result for SMA-concrete bond slip; (b) Shima et al. (1987) experimental result for steel-concrete bond slip and CEB-FIP (1993); (c) tension chord model (Marti P, 1998)

The Muntasir (2015) experimental SMA concrete bond slip results and Shima (1987) experimental steel and concrete bond slip relations have the same shape. Approximating the SMA and concrete bond slip law, as done by Marti (1998), by a stepped and rigid-perfectly-plastic law is fairly reasonable. To do so, the maximum bond strength and the plastic bond strength need to be known. The maximum bond strength can be approximated by empirical equation developed by Muntasir (2015):

$$\tau_{max} = k(0{,}9 - 0{,}004d - 0{,}0025l + 0{,}015\frac{c}{d})\sqrt{f_c'} \qquad (29)$$

with

- d the SMA rebar diameter.
- l the embedment length.
- c the concrete cover.
- f_c' the concrete compressive strength.
- k is the surface roughness factor.

The plastic bond strength can be approximated as $\frac{\tau_{max}}{3}$ based on the experimental data provided by Muntasir (2015).

According to the hypothesis that the stress-strain law for the concrete is linear and that the SMA stress-strain law is composed by three linear parts (Figure 45), by combining Equations (26), (27) and (28) we can obtain:

$$\frac{d^2\delta}{dx^2} = \frac{4 \cdot \tau_b}{{d\sigma_{sma}}/{dx} \cdot \emptyset_l} + \frac{\tau_b \cdot \pi \cdot \emptyset_l}{A_t \cdot E_c \cdot (1 - \rho_l)} \qquad (30)$$

E_c and ${d\sigma_{sma}}/{dx}$ are the young modulus of the concrete and the SMA. ${d\sigma_{sma}}/{dx}$, can take three values as seen in Table 2. As in Marti et al. (1998) model, with those assumptions, the steel stress distribution can be derived from Equation (30) without complex numerical integration.

5.2 SMA elements

To adapt the mechanical model developed by Tarquini et al (2019) to wall reinforced with SMA rebars, a new SMA element similar to the Anchorage-slip element or the tension chord element (see sections 4.3.1 and 4.3.2) was developed. Beforehand, the tension chord model developed by Marti et al. (1998) had to be modified as explained in the previous section.

The SMA element has the same purpose as the basic tension chord element, i.e. to represent the portion of a tension chord between two cracks. However, in this case, it needs to be adapted for a SMA-concrete tension chord element. For a value of $\varepsilon_{cs} < \varepsilon_{ac} < \varepsilon_{ult}$, where ε_{ac} is the SMA strain at crack, the SMA and concrete stress and strain distributions can be determined by equilibrium considerations. The crack width and the total chord elongation can be obtained by resolving Equations (11) and (12).

As explained earlier, there are 3 possible cases for the steel basic tension chord element. Firstly, the steel in the tension chord is still in the elastic phase, (1) $\varepsilon_{ac} < \varepsilon_y$. Secondly, part of the steel is still in the elastic phase and the other part is in the plastic phase, (2) $\varepsilon_{ac} > \varepsilon_y$ and $l_{ac,p} < srm/2$. Lastly, the steel is completely in the plastic phase, (3) $\varepsilon_{ac} > \varepsilon_y$ and $l_{ac,p} > srm/2$, where $l_{ac,p}$ is the length required to develop the plastic strain $\varepsilon_p = \varepsilon_{ac} - \varepsilon_y$,:

$$l_{ac,p} = \frac{A_s \cdot E_{sh} \cdot (\varepsilon_{ac} - \varepsilon_y)}{\tau_{b1} \cdot \pi \cdot \phi_l} \tag{31}$$

Due to the bilinear nature of the approximation of the steel stress-strains relation, three cases were distinguished. Similarly, due to the approximation of the SMA stress-strains relation composed of 3 linear parts, five cases were differentiated (see Figure 47), one for each linear part and one for each transition between two states:

1. $\varepsilon_{ac} < \varepsilon_{AMs}$
2. $\varepsilon_{ac} > \varepsilon_{AMs}$, $\varepsilon_{ac} < \varepsilon_{AMf}$ and $srm/2 > l_{ac,s}$
3. $\varepsilon_{ac} > \varepsilon_{AMs}$, $\varepsilon_{ac} < \varepsilon_{AMf}$ and $srm/2 < l_{ac,s}$
4. $\varepsilon_{ac} > \varepsilon_{AMf}$ and $\varepsilon_{ac} < l_{ac,f}$
5. $\varepsilon_{ac} > \varepsilon_{AMf}$ and $\varepsilon_{ac} > l_{ac,f}$

where $l_{ac,s}$ and $l_{ac,f}$ are defined as follows:

$$l_{ac,s} = \frac{A_{sma} \cdot E_{AMf} \cdot (\varepsilon_{ac} - \varepsilon_{AMs})}{\tau_{b1} \cdot \pi \cdot \phi_l} \tag{32}$$

$$l_{ac,f} = \frac{A_{sma} \cdot E_{nu} \cdot (\varepsilon_{ac} - \varepsilon_{SMf})}{\tau_{b2} \cdot \pi \cdot \phi_l} \tag{33}$$

with τ_{b1} and τ_{b2} the two values of the step approximation of the bond slip relation between concrete and SMA as explained in section 5.1.2 ($\tau_{b1} = \tau_{max}$ and $\tau_{b2} = \frac{\tau_{max}}{3}$).

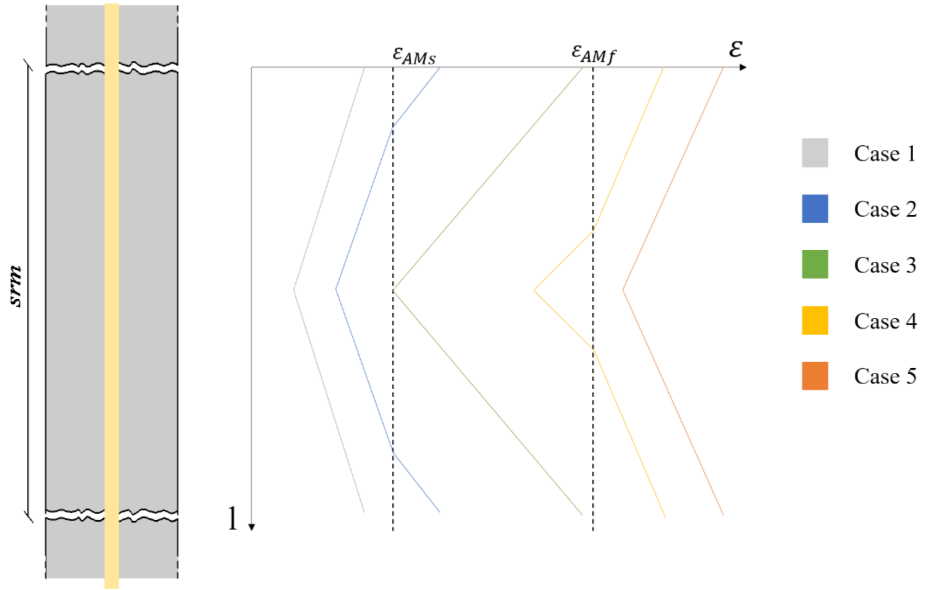

Figure 47 Basic tension chord element: Sketch and qualitative SMA strain profile;

The crack width and the elongation can be derived from Equations (11) and (12). The calculation for case 1 is developed below, the development for case 2 can be found in the Annex.

5.2.1 Crack width and elongation for case 1 of the SMA element

The total elongation of a basic SMA tension chord Δ_{TC} (Equation (12)) is developed for the case 1:

$$\Delta_{TC} = \int_{-\frac{srm}{2}}^{\frac{srm}{2}} \varepsilon_{sma}\, dx \tag{12}$$

With *srm* the distance between 2 cracks

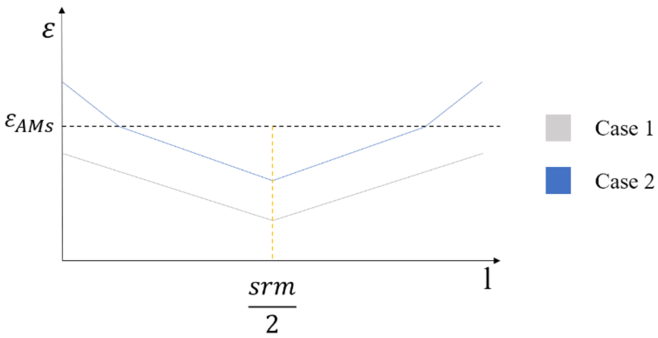

Figure 48 qualitative SMA strain profile for case 1 & 2.

$$\Delta_{TC} = \frac{1}{2}\left(\varepsilon_{ac} + \varepsilon_{\frac{srm}{2}}\right) \times \frac{srm}{2} \times 2 \tag{34}$$

$$\Delta_{TC} = \left(\varepsilon_{ac} + \varepsilon_{\frac{srm}{2}}\right) \times \frac{srm}{2} \tag{35}$$

$\varepsilon_{\frac{srm}{2}}$ can be calculated as the deformation due to the difference of force between the force applied at crack and the maximum force transmitted to the concrete (see Equation (10)):

$$\varepsilon_{\frac{srm}{2}} = \left(A_{sma}.\varepsilon_{ac}.E_{AMs} - \tau_{b1}.\pi.\frac{srm}{2}.\emptyset\right) \times \frac{1}{A_{sma}.E_{AMs}} \quad (36)$$

$$\varepsilon_{\frac{srm}{2}} = \varepsilon_{ac} - \frac{N_{c,max}}{A_{sma}.E_{AMs}} \quad (37)$$

Equation (37) can be substituted in Equation (35):

$$\Delta_{TC} = \left(2.\varepsilon_{ac} - \frac{N_{c,max}}{A_{sma}.E_{AMs}}\right) \times \frac{srm}{2} \quad (38)$$

$$\Delta_{TC} = \left(\varepsilon_{ac} - \frac{N_{c,max}}{2.A_{sma}.E_{AMs}}\right) \times srm \quad (39)$$

This final expression (39) gives the total elongation of a basic elongation Δ_{TC} for the case 1 of an SMA element. The expression of Δ_{TC} for cases 3 and 5 are not developed here because it is the same development as case 1 with only a different expression of E and $N_{c,max}$.

The crack width w can then be deduced from Equation (11):

$$w = \int_{-\frac{srm}{2}}^{\frac{srm}{2}} \varepsilon_{sma} - \varepsilon_c \, dx \quad (11)$$

with ε_c the concrete strain

$$w = \Delta_{TC} - \int_{-\frac{srm}{2}}^{\frac{srm}{2}} \varepsilon_c \, dx \quad (40)$$

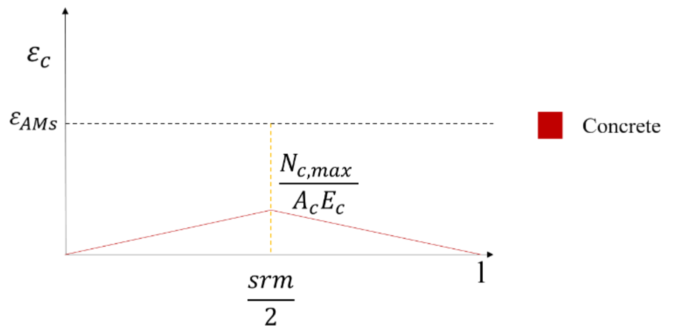

Figure 49 qualitative concrete strain profile.

$$w = \Delta_{TC} - \frac{N_{c,max}}{2.A_c.E_c} \times srm \quad (12)$$

By subtituing Equation (39) in Equation (41), the final expresion of the crack width for case 1 can be exrpessed as:

$$w = \left(\varepsilon_{ac} - \frac{N_{c,max}}{2.A_{sma}.E_{AMs}} - \frac{N_{c,max}}{2.A_c.E_c}\right) \times srm \tag{40}$$

Once again, the expression of the crack width for cases 3 and 5 are not developed as it is the same as case 1 with only different values of E and $N_{c,max}$.

Finally, the expression for all the cases of the total elongation of a basic SMA tension chord Δ_{TC} can be written as such:

$$\Delta_{TC} = \left(\varepsilon_{ac} - \frac{N_{c,max}}{2 \cdot A_{sma} \cdot E_{AMs}}\right) \cdot srm \qquad for\ case\ (1)$$

$$\Delta_{TC} = \varepsilon_{ac} \cdot l_{ac,s} + \varepsilon_{AMs} \cdot \frac{srm}{2} + \varepsilon_{\frac{srm}{2}} \cdot \left(\frac{srm}{2} - l_{ac,s}\right) \qquad for\ case\ (2)$$

$$\Delta_{TC} = \left(\varepsilon_{ac} - \frac{N_{c,max,s}}{2 \cdot A_{sma} \cdot E_{AMf}}\right) \cdot srm \qquad for\ case\ (3)$$

$$\Delta_{TC} = \varepsilon_{ac} \cdot l_{ac,f} + \varepsilon_{AMf} \cdot \frac{srm}{2} + \varepsilon_{\frac{srm}{2}} . \left(\frac{srm}{2} - l_{ac,f}\right) \qquad for\ case\ (4)$$

$$\Delta_{TC} = \left(\varepsilon_{ac} - \frac{N_{c,max,s}}{2 \cdot A_{sma} \cdot E_{nu}}\right) \cdot srm \qquad for\ case\ (5)$$

The expressions for all the cases of the crack width *w* can be written as such:

$$w = \left(\varepsilon_{ac} - \frac{N_{c,max}}{2.A_{sma}.E_{AMs}} - \frac{N_{c,max}}{2.A_c.E_c}\right) \times srm \qquad for\ case\ (1)$$

$$w = \Delta_{TC}^{case(2)} - \varepsilon_{c,s} \cdot \frac{srm}{2} - \varepsilon_{c,\frac{srm}{2}} \cdot \left(\frac{srm}{2} - l_{ac,p}\right) \qquad for\ case\ (2)$$

$$w = \left(\varepsilon_{ac} - \frac{N_{c,max,s}}{2.A_{sma}.E_{AMf}} - \frac{N_{c,max,s}}{2.A_c.E_c}\right) \times srm \qquad for\ case\ (3)$$

$$w = \Delta_{TC}^{case(4)} - \varepsilon_{c,s} \cdot \frac{srm}{2} - \varepsilon_{c,\frac{srm}{2}} \cdot \left(\frac{srm}{2} - l_{ac,f}\right) \qquad for\ case\ (4)$$

$$w = \left(\varepsilon_{ac} - \frac{N_{c,max,s}}{2.A_{sma}.E_{nu}} - \frac{N_{c,max,s}}{2.A_c.E_c}\right) \times srm \qquad for\ case\ (5)$$

5.3 Implementation

Once the new SMA element is created, the last step in the adaptation of the mechanical model is to include the element in the implementation. As explained in section 2.1, the SMA rebar is located just above the foundation, the more solicitated part during a seismic activity.

Conveniently, in the model, this location is the same as the lap splices element. In the wall tested, there was no lap splices element. As a consequence, for the adaptation to this specific case, the lap splices element was replaced by the SMA element as show in Figure 50 (b).

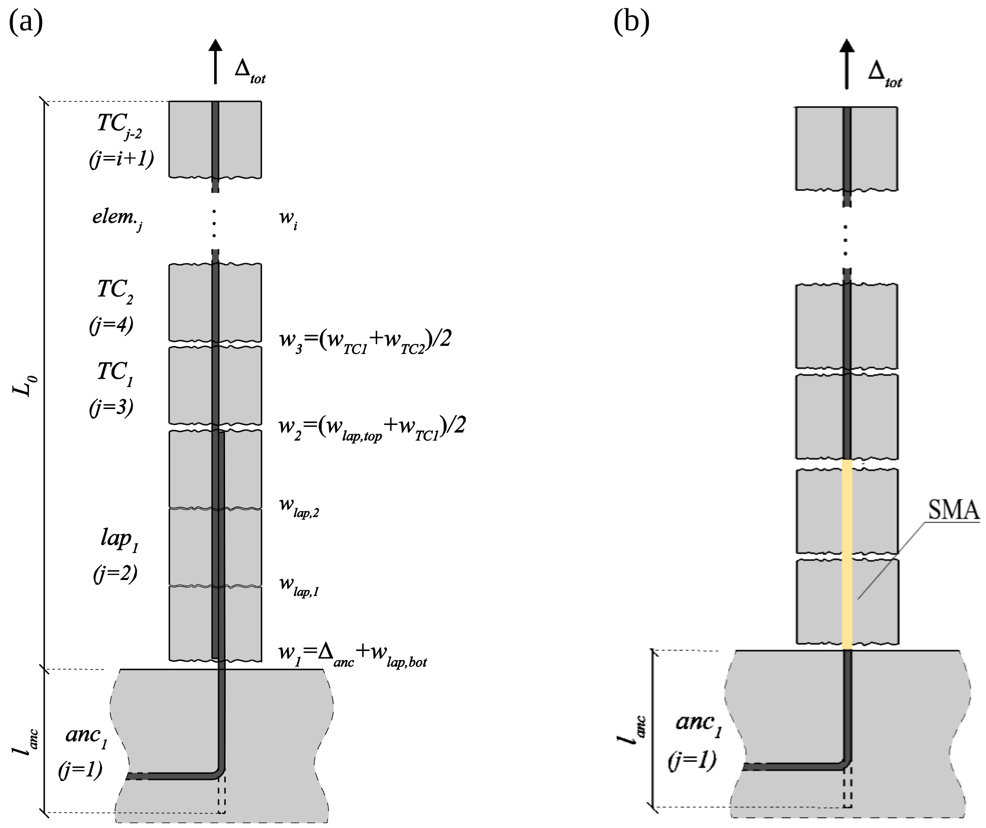

Figure 50 RC boundary element model: (a) (D. Taquini, 2019) Assembly of the components for a RC member featuring lap splice, anchorage, and multiple basic tension chord (TCi) elements; (b) Assembly of the components for a RC member featuring SMA basic tension chord, anchorage, and multiple basic tension chord elements.

There is no modification to the implementation of the model as described in section 4.4. The iterative method remains the same and, at every loop, the strain at crack ε_{ac} is updated. The only difference is the value of ε_{ac} for the SMA and the steel. The force for each iteration carried through all the elements represented in Figure 50 (a or b) is the same. For the mechanical model of Tarquini et al (2019), the ε_{ac} at every crack is the same but in the adaptation in Figure 50 (b) due to the different properties of the materials, ε_{ac} is no longer the same. As depicted in Figure 51, one can observe that for the same force the strain for the SMA and the steel is different.

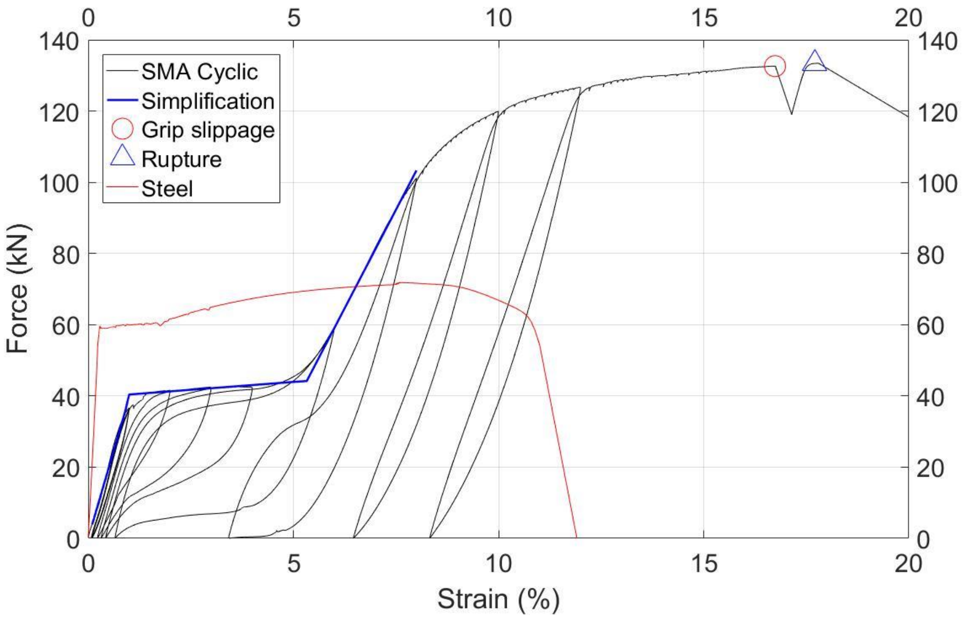

Figure 51 Steel and SMA: Strain-Force profile.

To incorporate this in the adaptation, just before the total elongation Δ_{TC} , the cracks widths *w* are calculated for all the different SMA elements. The steel strain at crack ($\varepsilon_{ac(1)}$) is adapted for the SMA ($\varepsilon_{ac(2)}$) as depicted in Table 3 :

$$\boxed{\varepsilon_{ac(1)}} \Rightarrow \boxed{\sigma_{steel}} \Rightarrow \boxed{Force} \Rightarrow \boxed{\sigma_{SMA}} \Rightarrow \boxed{\varepsilon_{ac(2)}}$$

Table 3 Path between the steel strain a crack $\varepsilon_{ac(1)}$ and the SMA strain at crack $\varepsilon_{ac(2)}$.

Once the total elongation Δ_{TC} is calculated for all the different SMA elements, the implementation can be carried on as explained in section 4.4. This final step concludes the adaptation of the model presented by Tarquini et al (2019) to a SMA reinforced concrete wall.

6 Comparison with experimental response

In this section, the results from the experiment described in section 2 are compared to the adaptation of the model made in section 5. Three different levels of displacement are explored in more details in section 6.1 and then the model limitations are discussed in section 6.2.

All the information, materials properties and experimental data acquired during the experiment were introduced in the new model. The length of the SMA rebar in the experimental wall is smaller than the SMA *srm*, which means that, theoretically, the length is not long enough to create even one SMA element. In other words, the length of the rebar is not long enough to transfer the concrete tensile stress f_{ct} from the SMA to the concrete trough bond stress. This can be verified by the experimental results, as no crack appeared along the SMA rebar length on wall during the experiment (see Figure 53 (b)).

To be able to compare the experience and the model, even if the location of the second crack above the foundation in the model will not correspond to the experience results, the model will still create a SMA element smaller than the minimal length.

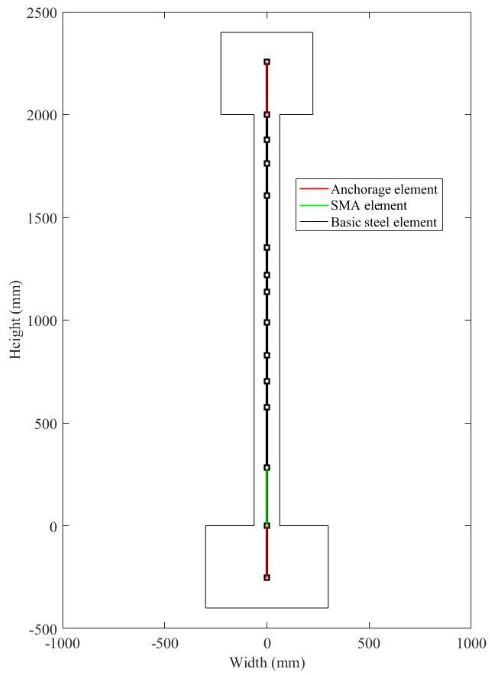

Figure 52 Modelization of SMA reinforced wall: elements representation.

Considering the previous assumption, Figure 52 represents the different elements composing the model for the experimental SMA reinforced wall.

The experimental measure of the crack width was taken manually between all LS during the test. To confirm the measurements and have a better evaluation of the wall boundary element, the DIC was used. Two numerical gauges were place at the limit of the boundary element of the SMA wall for each crack (Figure 53 (b)). The boundary element was defined as 20 cm width, englobing 4 layers of rebars (Figure 53 (a)). The mean of the two measurements from the gauges of each crack was then calculated and compared with the measurement taken manually. The base crack of the wall is out of the range of the DIC as it can be seen in Figure 53 (b) so only the value of the manually taken measurement is assumed

(a) (b)

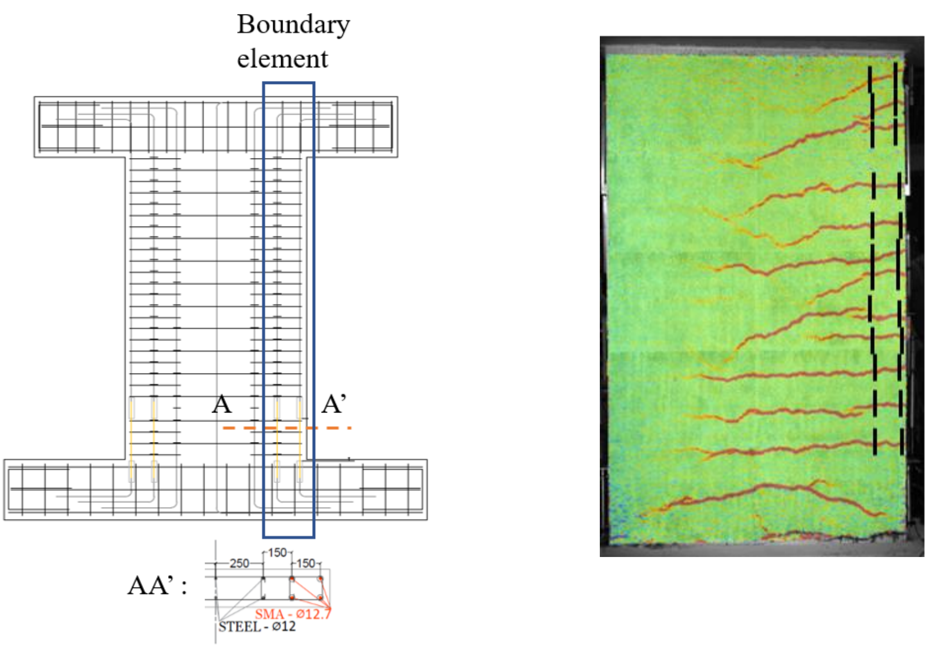

Figure 53 (a) Boundary element (b) DIC gauges.

6.1 Experimental cases

6.1.1 Case A

The first case is taken at LS 16 with a maximal drift of -0,268 % and a force of -84,01 kN. As illustrated in Figure 53(a), the wall is still in the early phase and has a small residual drift of 0,02 %. Figure 53(b) shows few cracks on the wall, which means that the wall did not reach the crack stabilization phase described in section 4.2.

(a) (b)

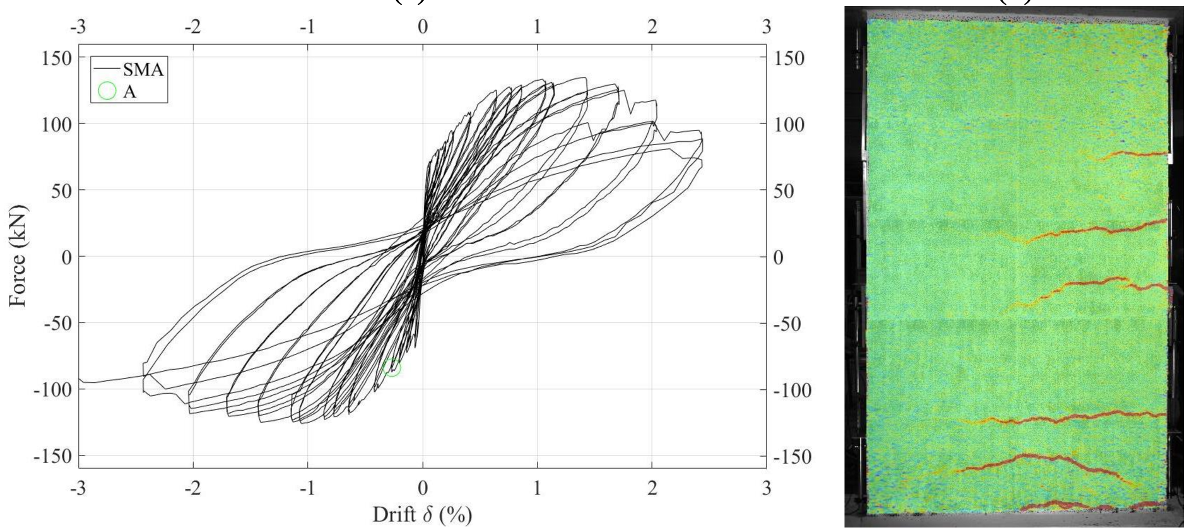

Figure 54 (a) SMA wall Force displacement response (b) DIC vertical strain representation.

The model gives the same assumption as predicted previously. Indeed, it can be seen in Figure 55 (c) that the green dot is on the plateau representing the crack opening phase, as explained in section 4.4 and illustrated in Figure 39. For a global top displacement Δ_{tot} smaller than Δ_{cs} (crack stabilization), the model assumes that there is no crack in the wall as illustrated in Figure 55 (a). This implies that the bond between the steel and the concrete is unbroken and the normal force is constant in the whole armature length. Figure 55(b) illustrates this consideration by having a constant strain for the whole steel length and along the SMA length. This is obviously not case in experimental response of the wall.

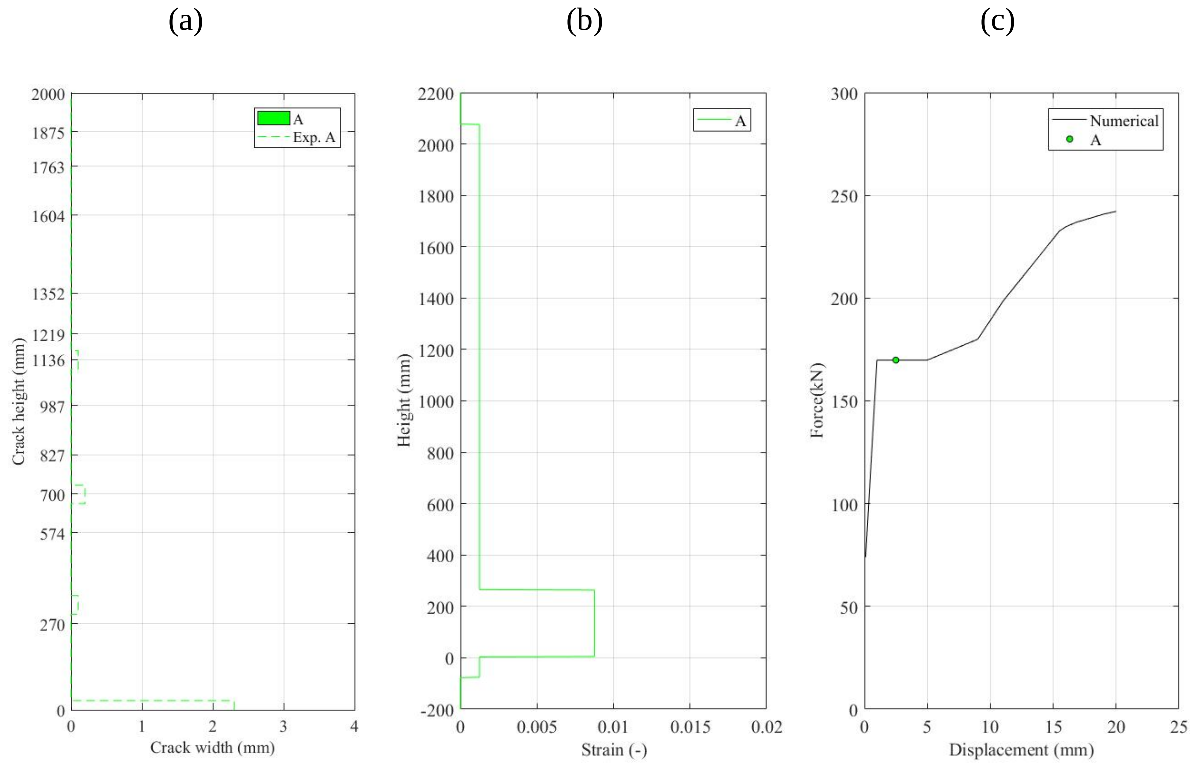

Figure 55 Mechanical model: (a) experimental vs numerical crack width (b) simulated strain profile (c) numerical force-displacement response.

Figure 55 (c) represents the numerical force displacement response of the model for the boundary element of the SMA wall (Figure 53(a)). The *Y* axis represents the force through the boundary element for a given displacement, not to be confused with the force of the *Y* axis from Figure 54, which is the force through the horizontal actuator of the test setup described in section 2. This force can easily be compared with Figure 56 as the boundary element contains 4 rebars and Figure 56 is the strain-force response of a steel rebar ($\emptyset = 12$ mm) and a single SMA rebar ($\emptyset = 12{,}7$ mm). The comparison between the two graphs is particularly interesting as it gives the state in which the steel and SMA are at crack and the value of strain can be compared with the values in Figure 55 (c). For this first case (A), from the green dashed line in Figure 56, one can see that the steel is in the plastic phase and SMA is at the limit of the austenite phase which explains, among other reasons, the small residual drift noted previously.

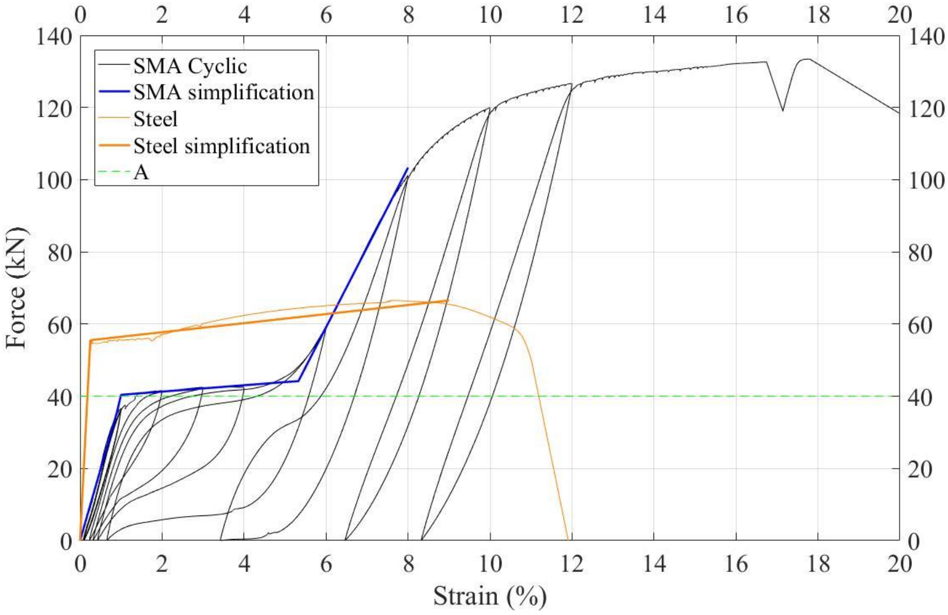

Figure 56 SMA and steel: Strain force response.

6.1.2 Case B

The second case (B) developed here is taken at LS 34 with a maximal drift of -1,071 % and a force of -123,61 kN. As illustrated in Figure 57(a) and (b), we can see that the wall has reached the limit of elasticity and is in a post-yield phase with a residual drift of 0,2 % which is under a permissible standard residual drift of 0,5 %.

(a) (b)

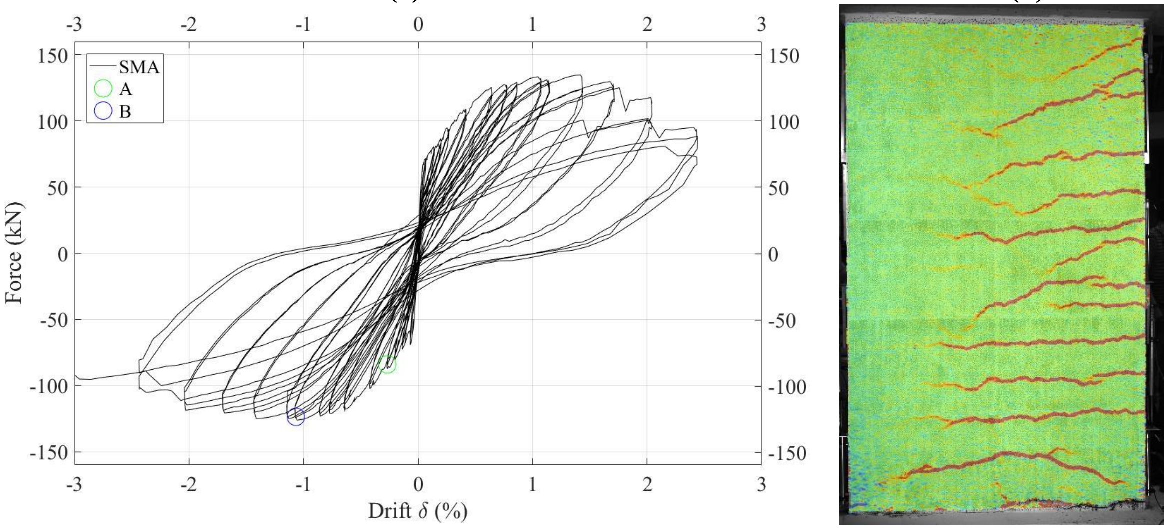

Figure 57 (a) SMA wall Force displacement response (b) DIC vertical strain representation.

As illustrated in Figure 58 (a), the model gives a good approximation of the crack width as compared to the experimental results. The experimental and numerical locations of the second crack above the foundation are different; this is due to the small length of the SMA and the way the issue was addressed as explained at the beginning of section 6. The model assumes that the wall is over the crack opening phase ($\Delta_{tot} > \Delta_{cs}$) as it can be seen in Figure 58 (c), the blue dot is over the plateau phase in which the green dot is. During the experimental test, no more cracks opened after LS 34, which confirms the model assumption. The model now considers that all the cracks are opened, and the strain profile in Figure 58 (b) is not as regular as for case (A).

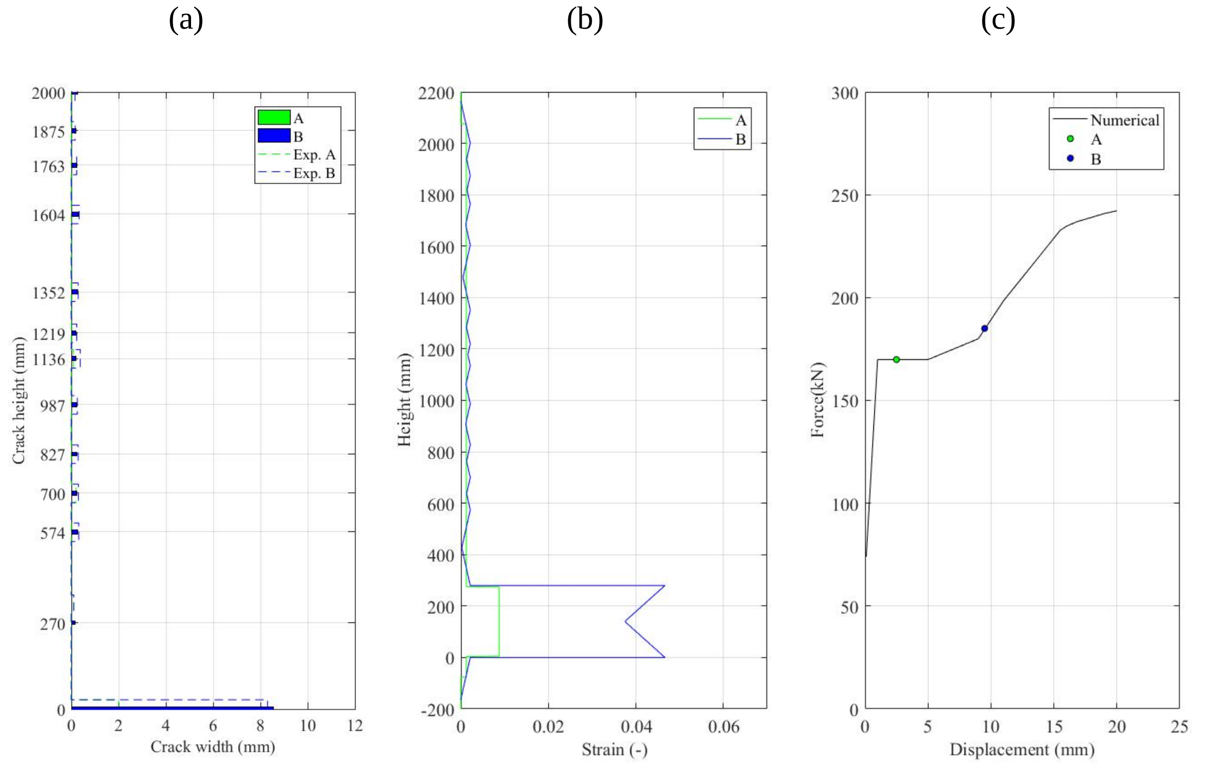

Figure 58 Mechanical model: (a) experimental vs numerical crack width (b) simulated strain profile (c) numerical force-displacement response.

Taking the force for case (B) from Figure 58 (c) and plotting it in Figure 59 for one rebar (the blue dashed line), the state of the SMA and steel can be obtained and the maximum value of the strain for both material in Figure 58 (b) can be read on the *X* axis of Figure 59. One can see that the steel is still in the elastic phase but the SMA is now in the austenite to martensite phase.

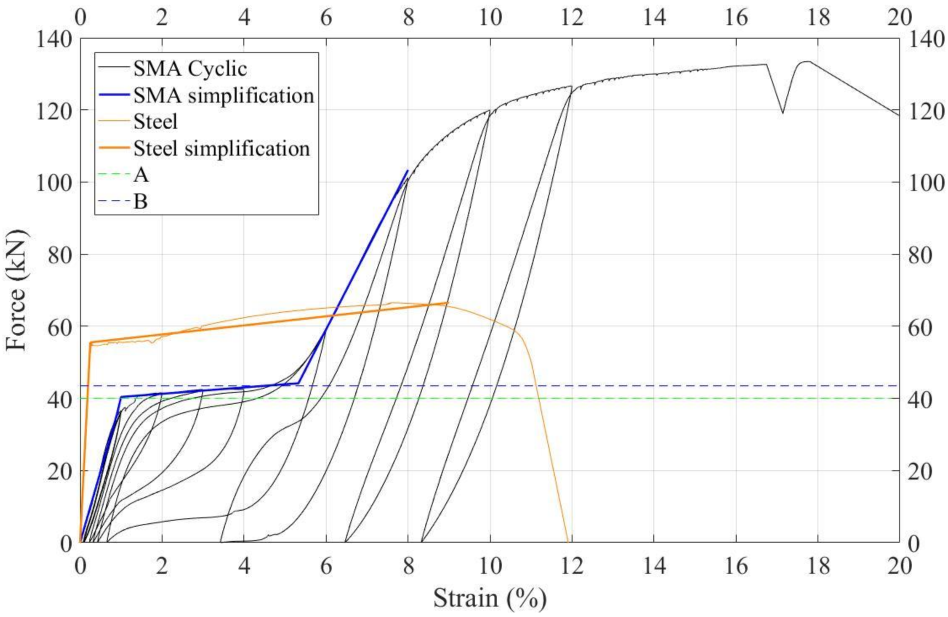

Figure 59 SMA and steel: Strain force response.

6.1.3 Case C

The last case (C) developed here is taken at LS 48 with a maximal drift of -1,8 % and a force of -118,8 kN. At LS 48, the wall is between LS 41 (the load stage in which the wall reached its maximum strength, i.e. 134,66 kN) and the rupture. The residual drift is 0,39 %, which is still under a permissible standard residual drift of 0,5 %.

(a) (b)

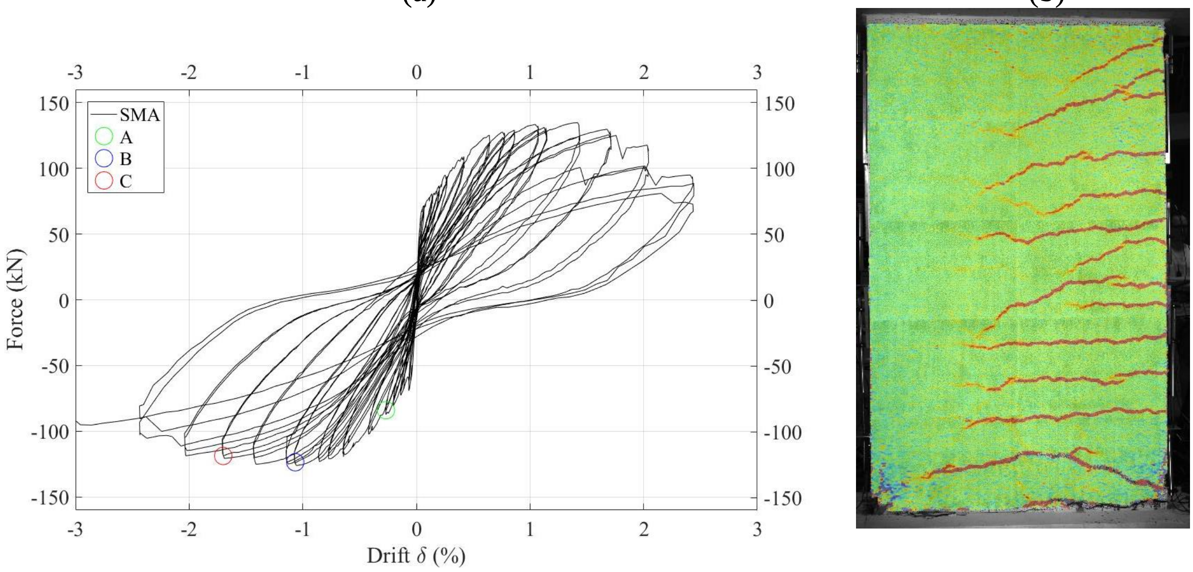

Figure 60 (a) SMA wall Force displacement response (b) DIC vertical strain representation.

Figure 61(a) shows the comparison between the experimental and numerical crack widths for the different cases. A good match between the two can be observed. Indeed, there is a maximum difference between the numerical and the experimental crack widths of 0,45 mm and an average difference of 0,04 mm. The model is thus able to capture the crack width evolution for the SMA element as well as for the other elements.

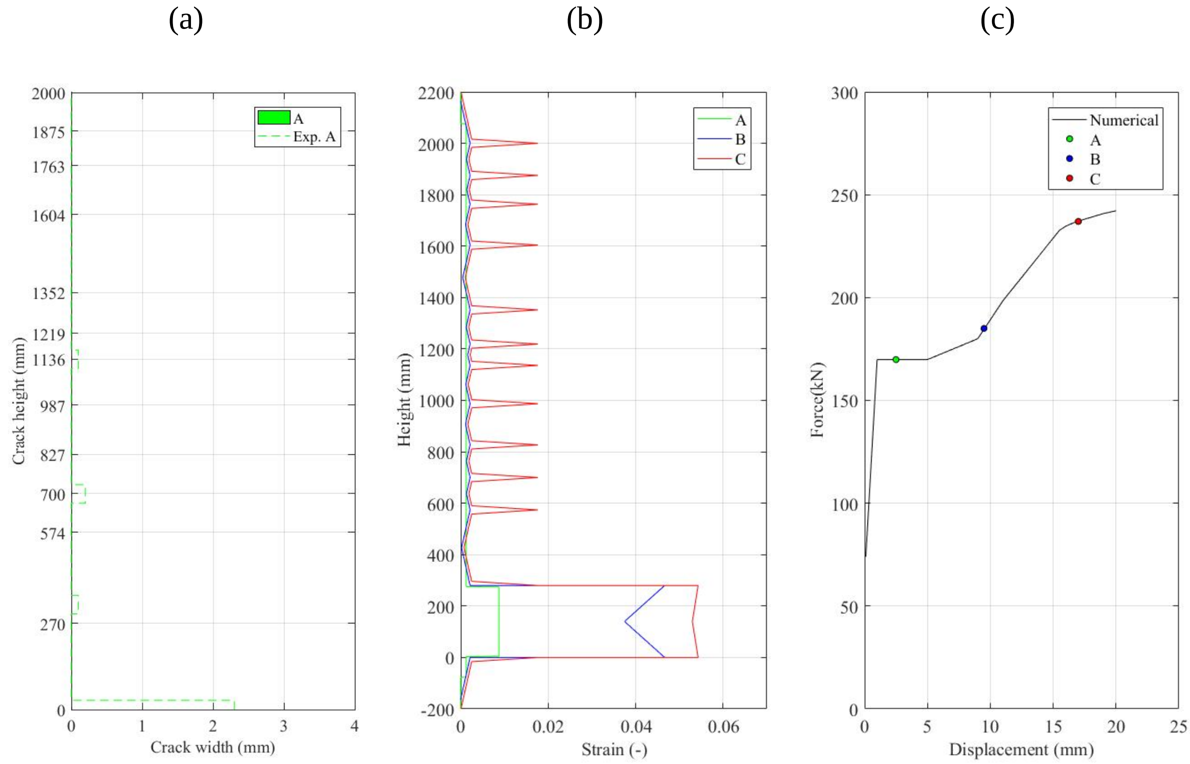

Figure 61 Mechanical model: (a) experimental vs numerical crack width (b) simulated strain profile (c) numerical force-displacement response.

The numerical strain profile for the three cases predicted by the model is represented in Figure 61(b) (the position of the different elements being represented in Figure 52). The changes of slope from case B to case C, for the SMA element and the steel, indicate a change of behaviour for both materials. This assumption can be confirmed by Figure 62. The SMA in now in the martensite phase and the steel in the plastic phase.

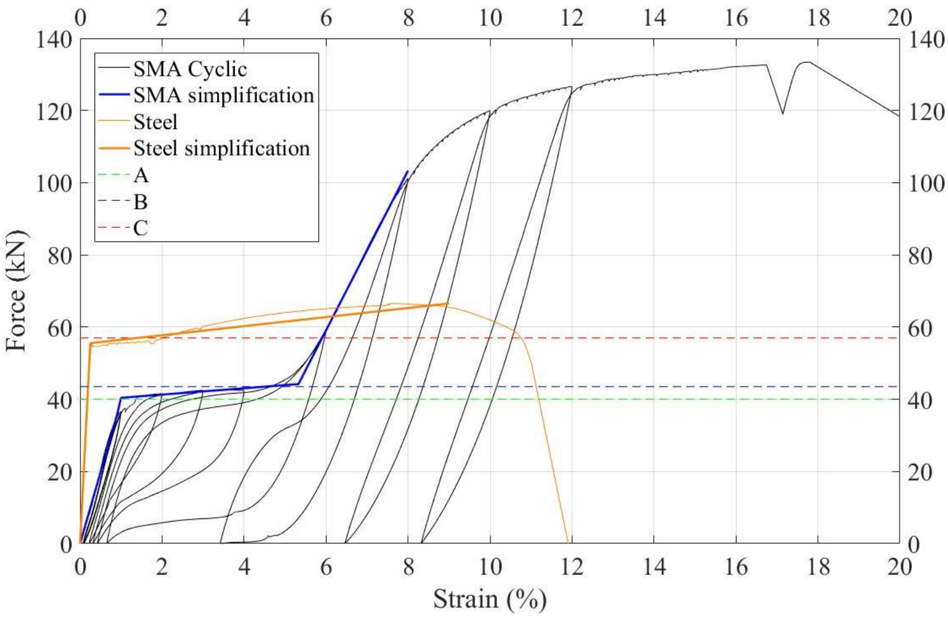

Figure 62 SMA and steel: Strain force response.

6.2 Model limitation

The adaptation of the model is a good fit to the data from the experience described in the first part of this thesis. Although some points could still be addressed.

First addressing the model itself:

- Before crack stabilization ($\Delta_{cs} > \Delta_{tot}$), the model considers, as illustrated in section 6.1 for the first case, that the cracks are not opened and that they all open once when $\Delta_{tot} = \Delta_{cs}$. The model could be developed further to have a better modelization of the early phase of the wall behaviour.
- A better approximation of the bond stress between the concrete and the SMA could be made. The same goes for the bond stress between the steel and the concrete, even if it would complicate the integration of Equation (4). A more discretized approximation would multiply the number of different cases for each element. The SMA element has already 5 case as explained in section 5.2.

Second, addressing if the model is a good fit for the experimental wall:

- The couplers described in section 2.3 are neglected in the model but are quite significative. To put it in perspective, the free length of SMA in the wall is 280 mm for two couplers of 140 mm.
- As explained at the beginning of section 6, the length of the SMA is too small to create a full SMA element. A solution could have been to develop a hybrid element composed of both materials.

Finally, to fully validate the model, additional comparisons with different experimental cases should be carried out. However, this first comparison shows very promising results.

7 Conclusion

The exceedance of tight limits for post-earthquake residual displacements typically imposes very costly repairs or structural demolition, which are a weight on the increasing economic losses from natural disasters. As reinforced concrete walls become a more widely used structural bracing system, the scientific and engineering community developed new self-centring technologies to control residual damage, such as post-tensioning tendons with energy dissipators. The current research addresses a more recent alternative technology, which requires minor adaptations to current construction practices as it transfers the recentring and energy-dissipation capabilities to the material level.

The present thesis describes the experimental response of two large-scale (2:3) reinforced concrete walls subjected to quasi-static cyclic loading protocols. In one-unit ribbed steel rebars were replaced by shape-memory bars over a limited height above the base inside the wall boundary element regions. The employed test setup allows imposing a large shear span, forcing the walls to behave in flexure as representative of medium to high-rise buildings. It was observed that the reference RC wall does not respond in the desired ductile way, and therefore the most relevant conclusion from this study take this fact into account:

- On one hand, the force capacity of the RC wall is 10 % lower than that of the RC+SMA unit, which closely agrees with the preliminary finite element simulations. On the other hand, the displacement ductility of the RC wall is smaller than that of the RC+SMA unit, and much lower than predicted by the numerical model. Such behaviour should not however be taken as representative due to the premature failure of the RC wall through an unintended brittle mechanism. Finally, the RC+SMA wall shows a better response than predicted by the finite element model, both in terms of ductility and bulkier energy-dissipation cycles.
- The evolution of the cracking pattern and damage progression in the RC+SMA wall complies with the capacity-design considerations for the SMA rebars and couplers. This is confirmed by the DIC strain maps and curvature profiles, which show that concentration of damage at the base occurs together with an elastic response of the steel rebars above the couplers.
- The minimal replacement of steel rebars by SMA rebars analysed in this study implies major improvements in terms of lateral residual displacement control. This effect becomes relevant for imposed displacement demands above the yield displacement, when the superelastic behaviour of the alloy is activated. Residual lateral displacements of the RC+SMA wall are roughly 1/3 of those of the RC unit, and up to failure the structural member shows a promising displacement recovery capacity of more than 75 %, which keep the unit below a permissible standard residual drift of 0.5 %.
- For small displacement demands below the yield displacement, which could be expected from low-intensity ground motions, the presence of SMA alloy rebars logically does not contribute to minimise the residual displacements, which can also be observed in the results of other studies.

- Often neglected but relevant in terms of post-earthquake serviceability, the vertical elongation due to the neutral axis flexural shift was also analysed. While the maximum elongations, which occur at peak drifts, are only very slightly larger than for the classical RC wall, a major reduction down to 50 % is seen to occur for the residual vertical elongation.

The previous observations confirm the promising avenue of this recent RC wall construction technology to improve seismic performance, both by facilitating repair works and ensuring an adequate earthquake response. As a concluding remark, it is noted that the short length of the SMA rebars employed in the tested walls (280 mm between couplers), selected in order to minimise the construction cost of the test units, is considerably lower than any estimate of the plastic hinge length for this wall. Although SMA rebars are still relatively expensive, much larger lengths in construction practice can be used as the increase in overall total building cost, particularly if non-structural components are also accounted for, will be negligible.

The boundary element in reinforced concert wall is the most strained region during a seismic activity. In the second part of this thesis, an adaptation of a mechanical model for the simulation of RC wall boundary element (D. Taquini, 2019) to accommodate RC wall with SMA rebar is presented. The newly adapted model is composed of three types of elements connected in series: an anchorage element, a basic steel-concrete tension chord element, accounting for most of the boundary element, and the new SMA element describing the deformation occurring along the SMA rebars. The newly created SMA element was derived from the classical steel-concrete tension chord model (Marti P, 1998). To solve the nonlinear problem, an iterative procedure is implemented. The adapted model can be used for any kind of RC wall by modifying the order or the number of the 3 different above-mentioned elements in the model. Results obtained with this new model were compared with the results from the experiment described in the first part of this thesis. Three cases, representing each a different level of total elongation of the boundary element, were discussed in details. Comparisons were made in terms of crack width and location. For each case, the model provided the cracks width, the crack location, the numerical force-displacement response and the strain profile along the boundary element and along the anchorage into the foundation. The comparison between the experimental and numerical crack width for the different cases shows a good match with a maximum difference between the numerical and the experimental crack width of 0,45 mm and an average difference of 0,04 mm. The model is able to capture the crack width evolution for the SMA element as well as for the other elements.

As discussed in this thesis, there is still place for improvement in both the experimentation and modeling aspects of the subject (amongst others: a bigger length of SMA in the wall, a more ductile steel rebars in the RC wall, additional data to analyze, a better approximation of the bond stress in the model...). However, the results presented here help in proving the consistency of the approach and provide a step forward in the paraseismic field.

Bibliographic references

A. Abdulridha, D. P. (2017). Behaviour and modelling of hybrid SMA-steel reinforced concrete shear wall. *Eng. Struct. 147* , 77-89. https://doi.org/10.1016/j.engstruct.2017.04.058.

A. Belleri, M. S. (2014). Fleischman, Dynamic behavior of rocking and hybrid cantilever walls in a precast concrete building. *ACI Struct. J. 111* , 661-671. https://doi.org/10.14359/51686778.

A.H.M.M. Billah, M. A. (2012). Seismic performance of concrete columns reinforced with hybrid shape memory alloy (SMA) and fiber reinforced polymer (FRP) bars. *Constr. Build. Mater. 28* , 730-742. https://doi.org/10.1016/j.conbuildmat.2011.10.020.

B. Mas, D. B.-A. (2017). Superelastic shape memory alloy cables for reinforced concrete applications. *Constr. Build. Mater. 148* , 307-320. https://doi.org/10.1016/j.conbuildmat.2017.05.041.

B. Wang, S. Z. (2018). Seismic behavior of self-centering reinforced concrete wall enabled by superelastic shape memory alloy bars. *Bull. Earthq. Eng. 16* , 479-502. https://doi.org/10.1007/s10518-017-0213-8.

C.M. Ramirez, E. M. (2012). Significance of residual drifts in building earthquake loss estimation. *Earthq. Eng. Struct. Dyn. 41* , 1477-1493. https://doi.org/10.1002/eqe.2217.

D. Taquini, J. A. (2019). The Deformation Capacity of Lap Splices in RC Walls: From Experimental Testing to Numerical Modelling. *Lausanne, EPFL*.

D. Tarquini, J. A. (2017). Axially equilibrated displacement-based element for simulating the cyclic inelastic behaviour of RC members. *Earthq. Eng. Struct. Dyn. 46* , 1471-1492. https://doi.org/10.1002/eqe.2865.

Dunbar, P. (2014). Significant Earthquake. *Ngdc.noaa.gov*.

E. Abraik, M. Y. (2015). Cyclic performance of shape memory alloy reinforced concrete walls, Fifth International Workshop on Performance, Protection and Strengthening of Structures under Extreme Loading . *no. 5*, pp. 326-333. https://doi.org/10.13140.

E. Rosenblueth, R. M. (1986). The 1985 Mexico earthquake: causes and effects in Mexico City . *Concrete International 8*, 23–34.

ECS. (2004). Eurocode, EN 1998-1. Eurocode 8: Design of structures for earthquake resistance – Part 1: General rules, seismic actions and rules for buildings. *European Committee for Standardization, Brussels, Belgium*.

EMDAT. (2017). OFDA/CRED International Disaster Database, . *Université Catholique de Louvain, Brussels, Belgium*, https://ourworldindata.org/natural-disasters.

F. Marquis, J. K. (2017). Understanding post-earthquake decisions on multi-storey concrete buildings. *Christchurch, New Zealand, Bull. of Earthq. Eng.* , 731-758. https://doi.org/10.1007/s10518-015-9772-8 .

F. McKenna, G. F. (2000). Open System for Earthquake Engineering Simulation (OpenSees). *Berkely, California, USA.*

G.A. MacRae, K. K. (1997). Post-earthquake residual displacements of bilinear oscillators. *Earthq. Eng. Struct. Dyn. 26*, 701–716. https://doi.org/10.1002/(SICI)1096-9845(199707)26:7<701::AID-EQE671>3.0.CO;2-I.

Hall, P. (2004). Laser welding nitinol to stainless steel. *Proceedings of the International Conference on Shape Memory and Superelastic Technologies SMST-2003 USA, California: SMST Society*, 219–28. https://doi.org/10.1361/ep2003smst219.

I. Fehr, P. G. (2005). Managing Tsunami Risk in the Aftermath. *RMS*.

J. McCormick, H. A. (2008). Permissible residual deformation levels for building structures considering both safety and human elements. *14th World Conference on Earthquake Engineering (2008),* Paper ID 05-06-0071.

J.B. Mander, C.-T. C.-T. (1997). Seismic resistance of bridge piers based on damage avoidance design. *Technical Report NCEER-97-0014, U.S. National Center for Earthquake Engineering Research (NCEER) Dept. of Civil and Environmental Engineering, State Univ.* .

J.I. Restrepo, A. R. (2007). Seismic performance of self-centering structural walls incorporating energy dissipators. *J. Struct. Eng. 133*, 1560-1570. https://doi.org/10.1061/(ASCE)0733-9445(2007)133:11(1560).

J.M. Rius, A. C. (2019). Shear strengthening of reinforced concrete beams using shape memory alloys. *Constr. Build. Mater. 200* , 420-435. https://doi.org/10.1016/j.conbuildmat.2018.12.104.

J.P. Almeida, D. T. (2017). Axially equilibrated displacement-based element for simulating the cyclic inelastic behaviour of RC members. *Earthq. Eng. Struct. Dyn. 46* , 1471-1492. https://doi.org/10.1002/eqe.2865.

K.M. Twigden, R. H. (2019). Shake table testing of unbonded post-tensioned concrete walls with and without additional energy dissipation. *Soil Dyn. Earthq. Eng. 119* , 375-389. https://doi.org/10.1016/j.soildyn.2018.05.007.

Kawashima,]. K. (2000). Seismic design and retrofit of bridges, Seismic design and retrofit of bridges. *Bull. New Zeal. Soc. Earthq. Eng. 33* , 265–285.

L. Cortés-Puentes, M. Z. (2018). Cyclic loading testing of repaired SMA and steel reinforced concrete shear walls. *Eng. Struct. 168* , 128-141. https://doi.org/10.1016/j.engstruct.2018.04.044.

M. Bruneau, A. R. (2007). Exploring the concept of seismic resilience for acute care facilities. *Earthq. Spectra. 23* , 41-62. https://doi.org/10.1193/1.2431396 .

M. Maciel, D. P. (2016). Seismic response of SMA reinforced shear walls. *Conf. Proc. Soc. Exp. Mech. Ser. 6* , 185–192. https://doi.org/10.1007/978-3-319-29910-5_19.

M. Steinmetz, T. W. (2019). Design of an experimental step for cyclic testing of large-scale units at LEMSC. *MSc. thesis, UCLouvain,*.

M.A. Youssef, M. A. (2008). Experimental investigation on the seismic behavior of beam-column joints reinforced with superelastic shape memory alloys. *J. Earthq. Eng. 12* , 1205-1222. https://doi.org/10.1080/13632460802003082.

M.J.N. Priestley, J. T. (1993). Seismic response of precast prestressed concrete frames with partially debonded tendons. *PCI J. 38* , 58-69. https://doi.org/10.15554/pcij.01011993.58.69.

M.J.N. Priestley, S. S. (1999). Preliminary results and conclusions from the PRESSS five-story precast concrete test building. *PCI J. 44* , 42–67. https://doi.org/10.15554/pcij.11011999.42.67.

M.J.T. Kian, C. N. (2018). Damage mitigation in reinforced concrete shear walls detailed with SMA and SFRC. *Int. Conf. Civil, Struct. Transp. Eng.,* 103.1-103.8. https://doi.org/10.11159/iccste18.103.

M.S. Alam, M. Y. (2010). Exploratory investigation on mechanical anchors for connecting SMA bars to steel or FRP bars. *Mater. Struct. Constr. 43*, 91–107. https://doi.org/10.1617/s11527-010-9601-0.

M.S. Saiidi, H. W. (2006). Exploratory study of seismic response of concrete columns with shape memory alloys reinforcement. *ACI Struct. J. 103*, 436–443. https://doi.org/10.14359/15322.

M.S. Saiidi, M. S.-Z. (2007). Pilot study of behavior of concrete beams reinforced with shape memory alloys. *J. Mater. Civ. Eng. HYPERLINK "https://ascelibrary.org/toc/jmcee7/19/6"19* , 454-461. https://doi.org/10.1061/(ASCE).

Marti P, A. M. (1998). Tension Chord Model for Structural Concrete. *Struct Eng Int 8*, doi: 10.2749/101686698780488875.

Muir-Wood, R. (2012). The Christchurch earthquakes of 2010 and 2011. *The Geneva risk reports. Risk and insurance research. Extreme events and insurance: 2011 Annus horribilis. Courbage C, Stahel WR, Geneva.* , http://www.genevaassociation.org. .

NBN. (2001). EN 12390. Testing hardened concrete. *Bureau de Normalisation, Belgium*.

Priestley, M. (2003). Myths and Fallacies in Earthquake Engineering, revisited. The Ninth Mallet Milne Lecture. *IUSS Press, Istituto Universitario di Studi Superiori di Pavia, Italy*, .

R. DesRoches, J. M. (2004). Cyclic Properties of Superelastic Shape Memory Alloy Wires and Bars. *J. Struct. Eng. 130* , 38-46. https://doi.org/10.1061/(ASCE)0733-9445(2004)130:1(38).

T. Herrezeel, F. R. (2019). Seismic design and performance of reinforced concrete walls with shape memory alloy reinforcement. *MSc. thesis, UCLouvain*.

T. Holden, J. R. (2003). Seismic performance of precast reinforced and prestressed concrete walls. *J. Struct. Eng. 129* , 286-296. https://doi.org/10.1061/(ASCE)0733-9445(2003)129:3(286).

W.A. Zatar, H. M. (2002). Residual displacements of concrete bridge piers subjected to near field earthquakes. *ACI Struct. J. 99* , 740-749. https://doi.org/10.14359/12338.

X. Geng, W. Z. (2019). Cyclic experimental response of self-centering concrete frames with slotted columns. *Constr. Build. Mater. 195* , 363-375. https://doi.org/10.1016/j.conbuildmat.2018.11.079.

X. Zhai, X. Z. (2019). Study on seismic performance of precast fabricated RC shear wall with opening filling. *Constr. Build. Mater. 214* , 539-556. https://doi.org/10.1016/j.conbuildmat.2019.04.070.

8 Annexes

8.1 Instrumentation

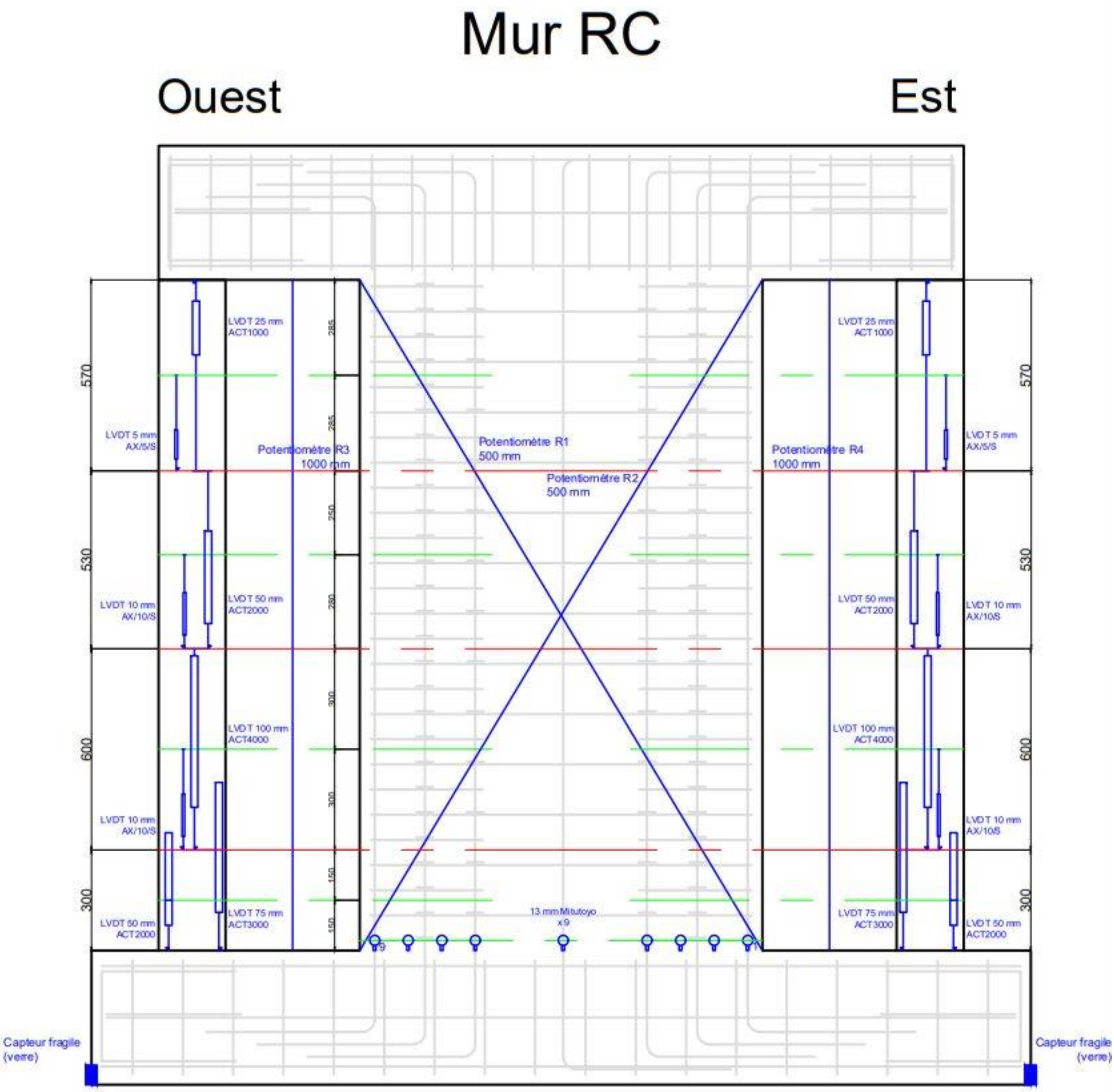

8.1.1 RC wall

8.1.2 SMA wall

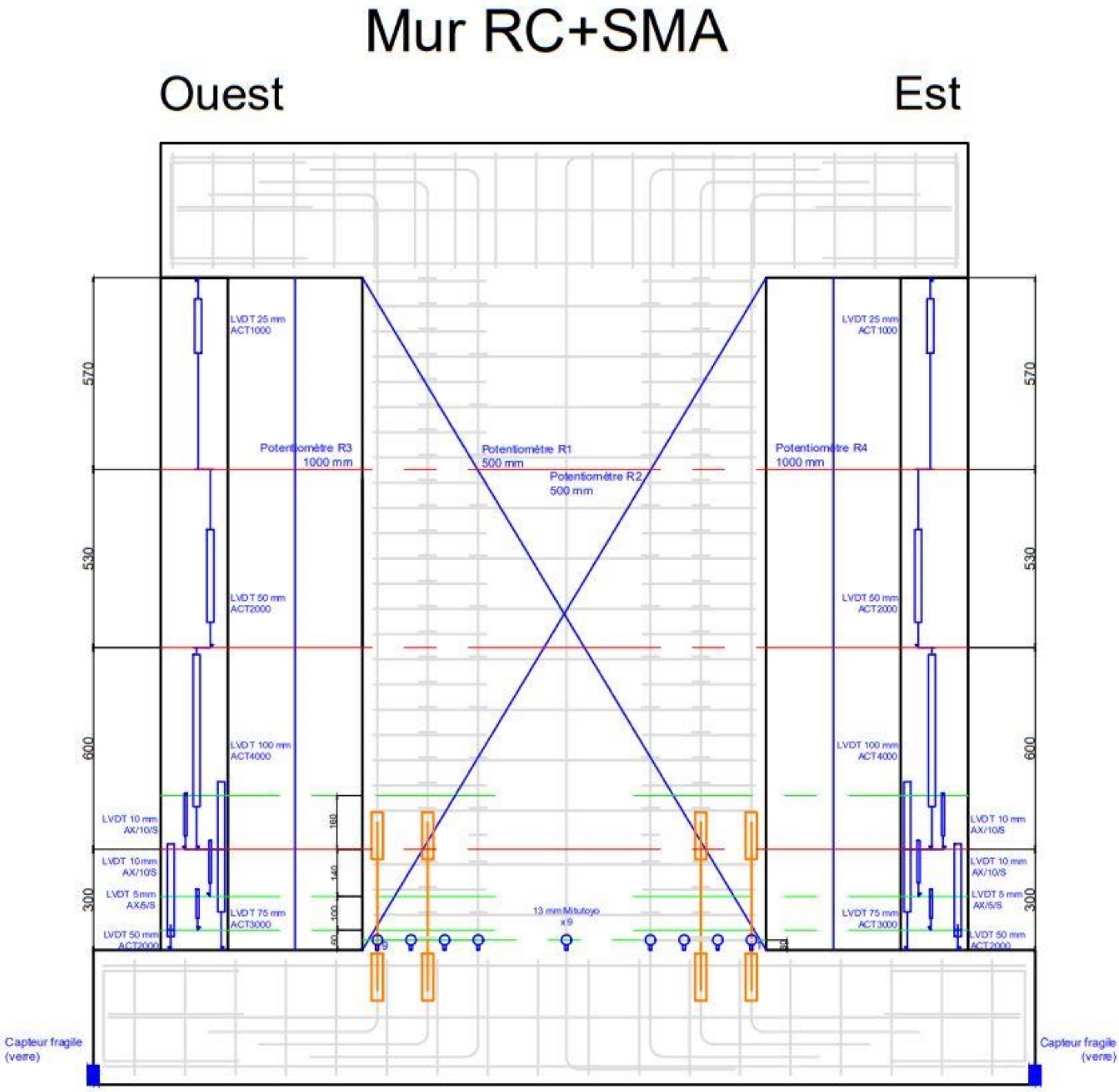

Mur RC+SMA
Ouest
Est
LVDT 25 mm
ACT1000
Potentiomètre R3
1000 mm
Potentiomètre R1
500 mm
Potentiomètre R2
500 mm
Potentiomètre R4
1000 mm
LVDT 50 mm
ACT2000
LVDT 100 mm
ACT4000
LVDT 10 mm
AX/10/S
LVDT 5 mm
AX/5/S
LVDT 75 mm
ACT3000
13 mm Mitutoyo
x 9
570
530
600
300
160
140
100
80
Capteur fragile
(verre)

8.2 Plans: RC wall

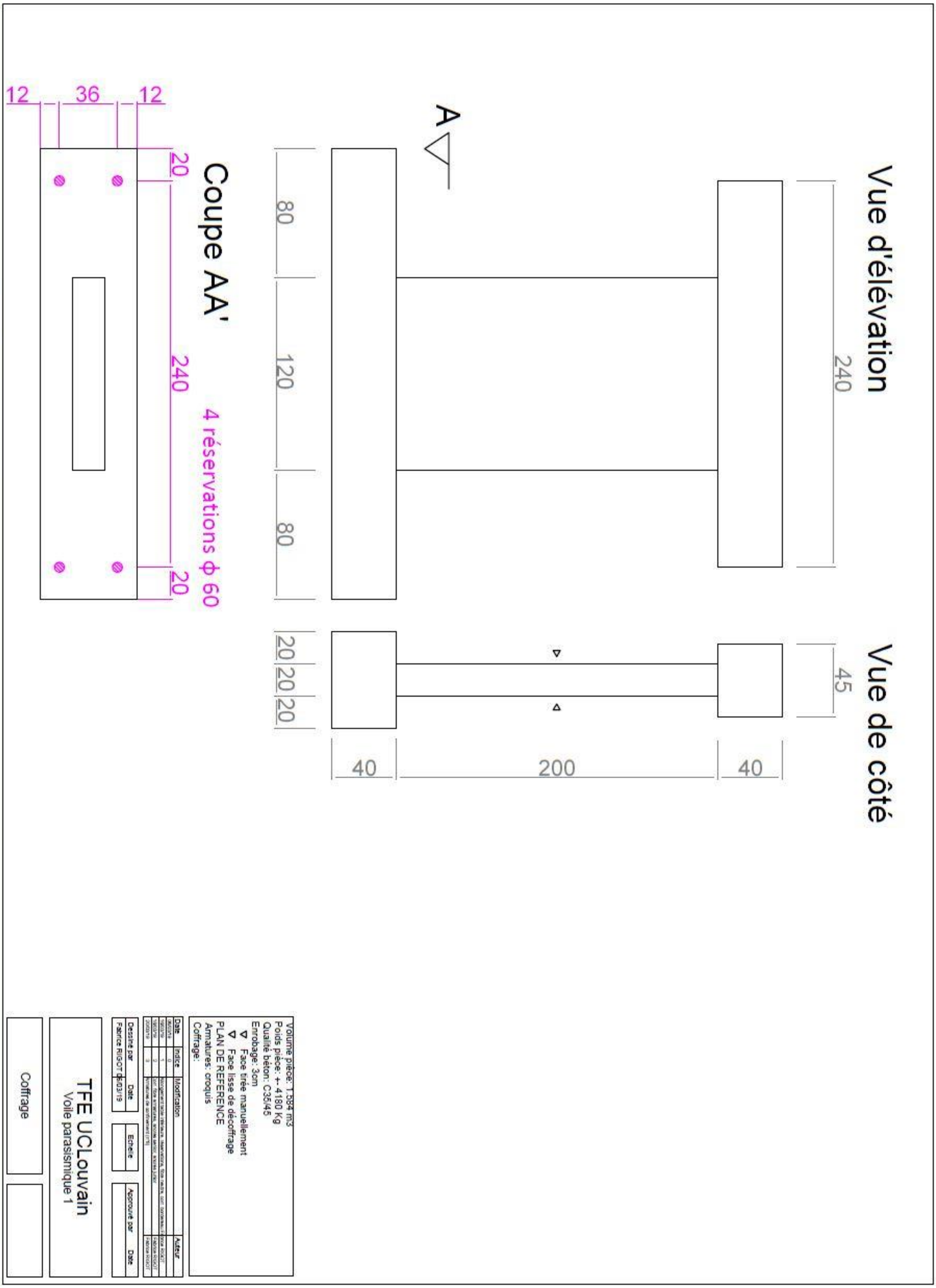

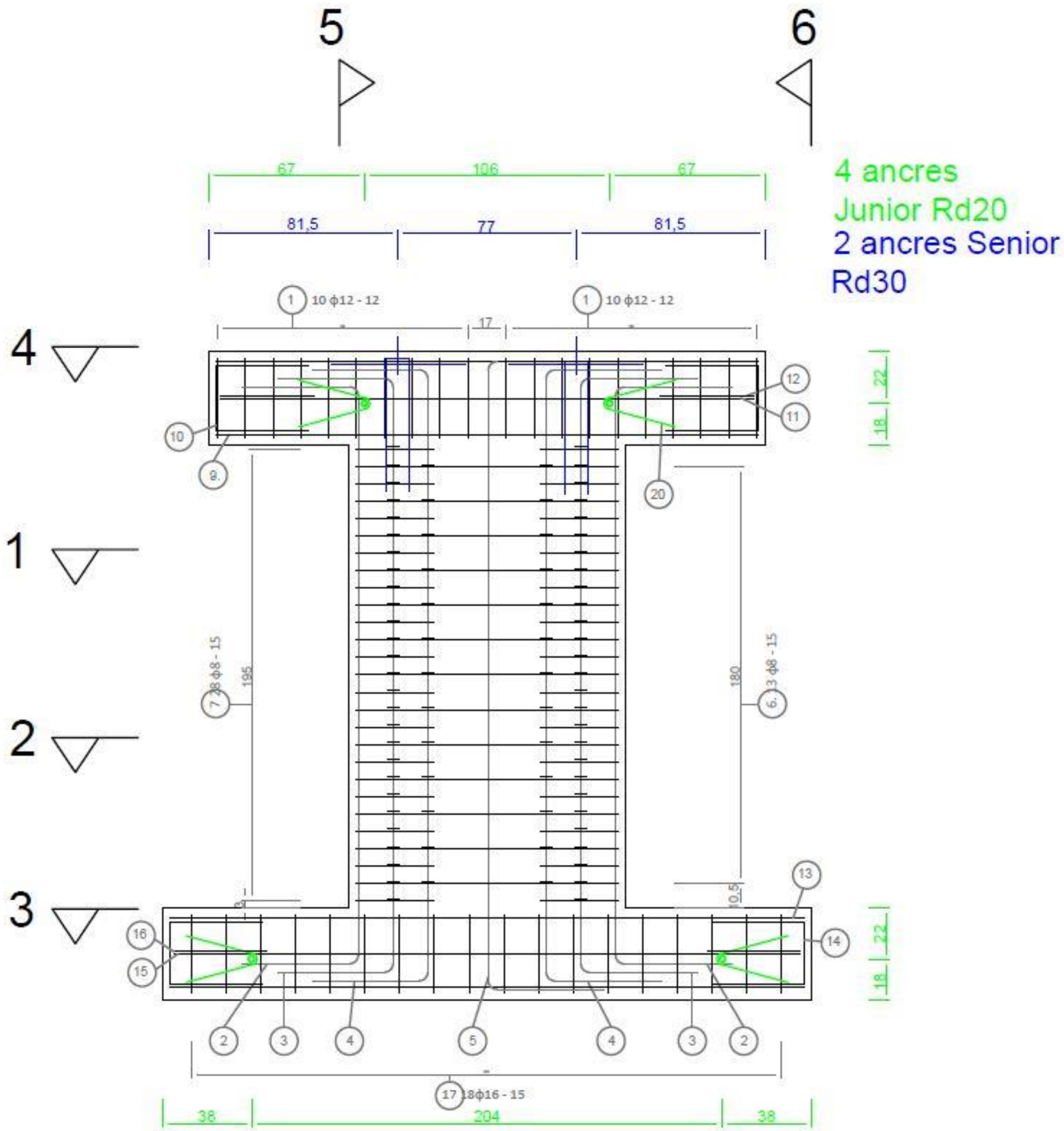

Volume pièce: 1.584 m3
Poids pièce: +- 4180 Kg
Qualité béton: C35/45
Enrobage: 3cm
▽ Face tirée manuellement
▽ Face lisse de décoffrage
PLAN DE REFERENCE
Armatures: croquis
Coffrage:

Date	Indice	Modification	Auteur

Dessiné par	Date	Echelle	Approuvé par	Date
Fabrice RIGOT	09/03/19			

TFE UCLouvain
Voile parasismique 1

Armatures

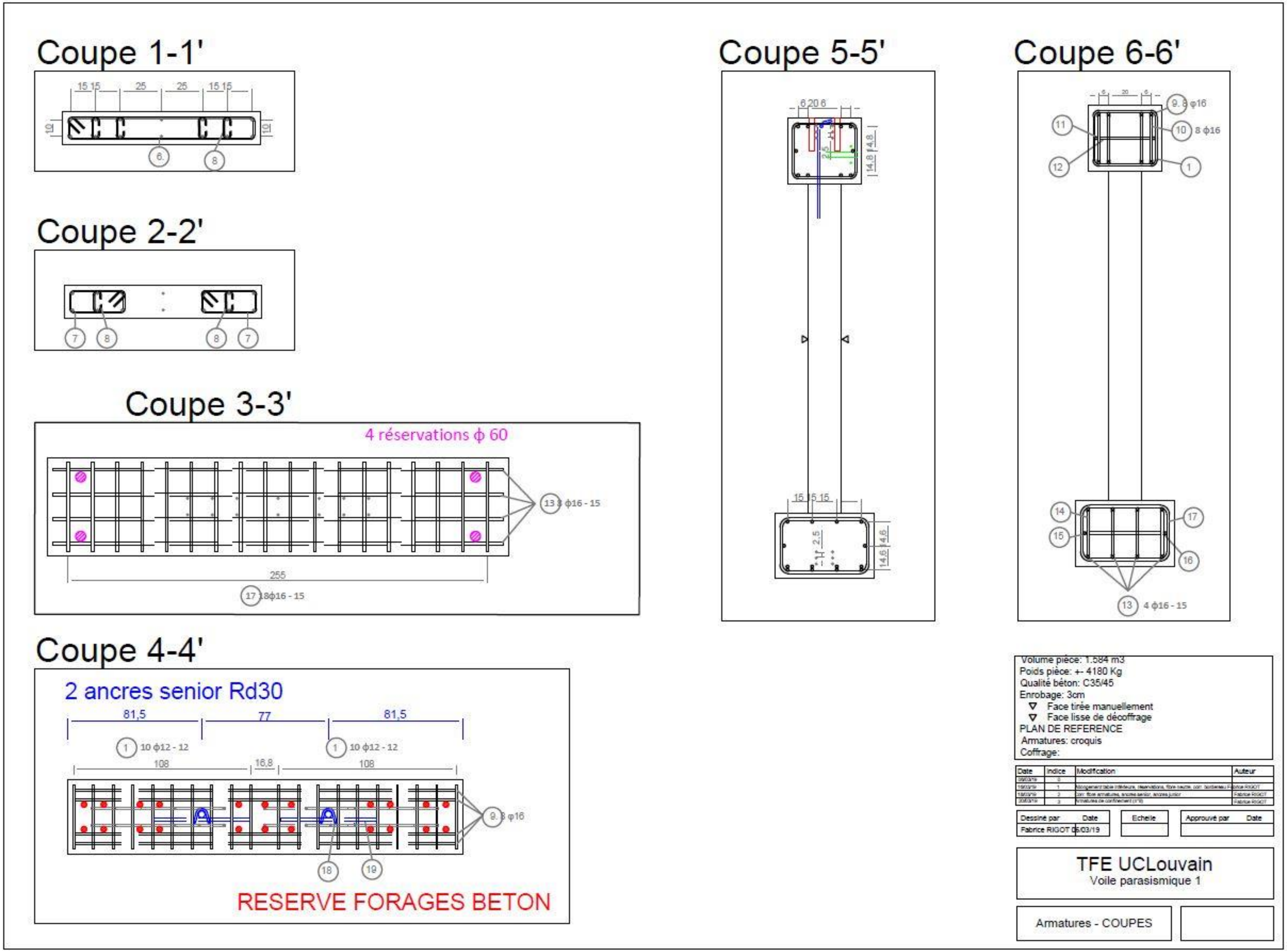
Coupe 1-1'
15 15
25
25
15 15
10
10
6.
8
Coupe 2-2'
7
8
8
7
Coupe 3-3'
4 réservations ϕ 60
13 8 ϕ16 - 15
255
17 18ϕ16 - 15
Coupe 4-4'
2 ancres senior Rd30
81,5
77
81,5
1 10 ϕ12 - 12
1 10 ϕ12 - 12
108
16,8
108
9. 8 ϕ16
18
19
RESERVE FORAGES BETON
Coupe 5-5'
6 20 6
2,5
14,8 14,8
15 15 15
2,5
14,6 14,6
Coupe 6-6'
6 20 6
9. 8 ϕ16
11
10 8 ϕ16
12
1
14
17
15
16
13 4 ϕ16 - 15
Volume pièce: 1.584 m3
Poids pièce: +- 4180 Kg
Qualité béton: C35/45
Enrobage: 3cm
Face tirée manuellement
Face lisse de décoffrage
PLAN DE REFERENCE
Armatures: croquis
Coffrage:
Date
Indice
Modification
Auteur
0
1
2
3
Fabrice RIGOT
Fabrice RIGOT
Fabrice RIGOT
Dessiné par
Date
Fabrice RIGOT 05/03/19
Echelle
Approuvé par
Date
TFE UCLouvain
Voile parasismique 1
Armatures - COUPES

8.3 Plans: SMA

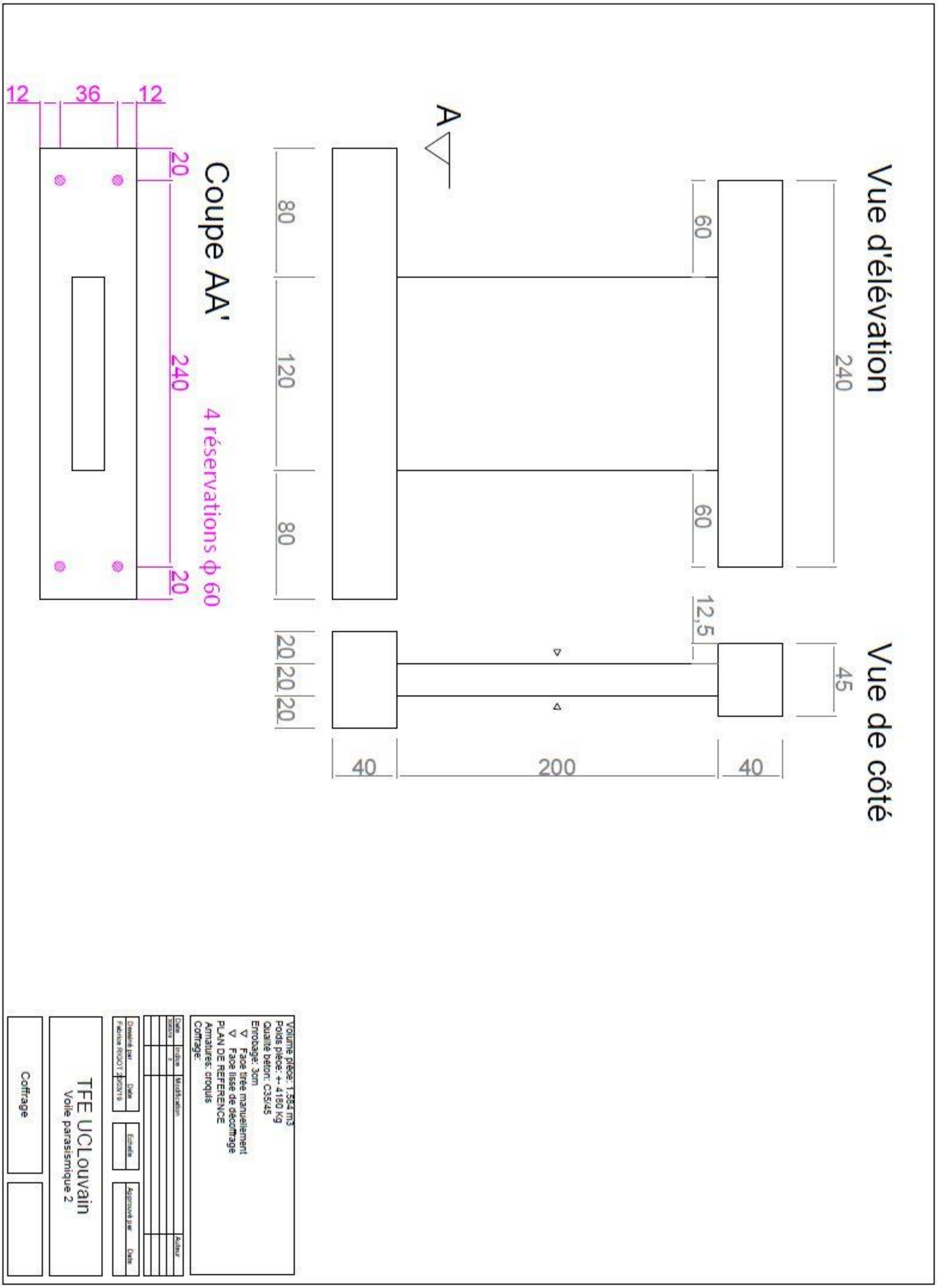
Vue d'élévation
Vue de côté
Coupe AA'
4 réservations ф 60
A
TFE UCLouvain
Voile parasismique 2
Coffrage

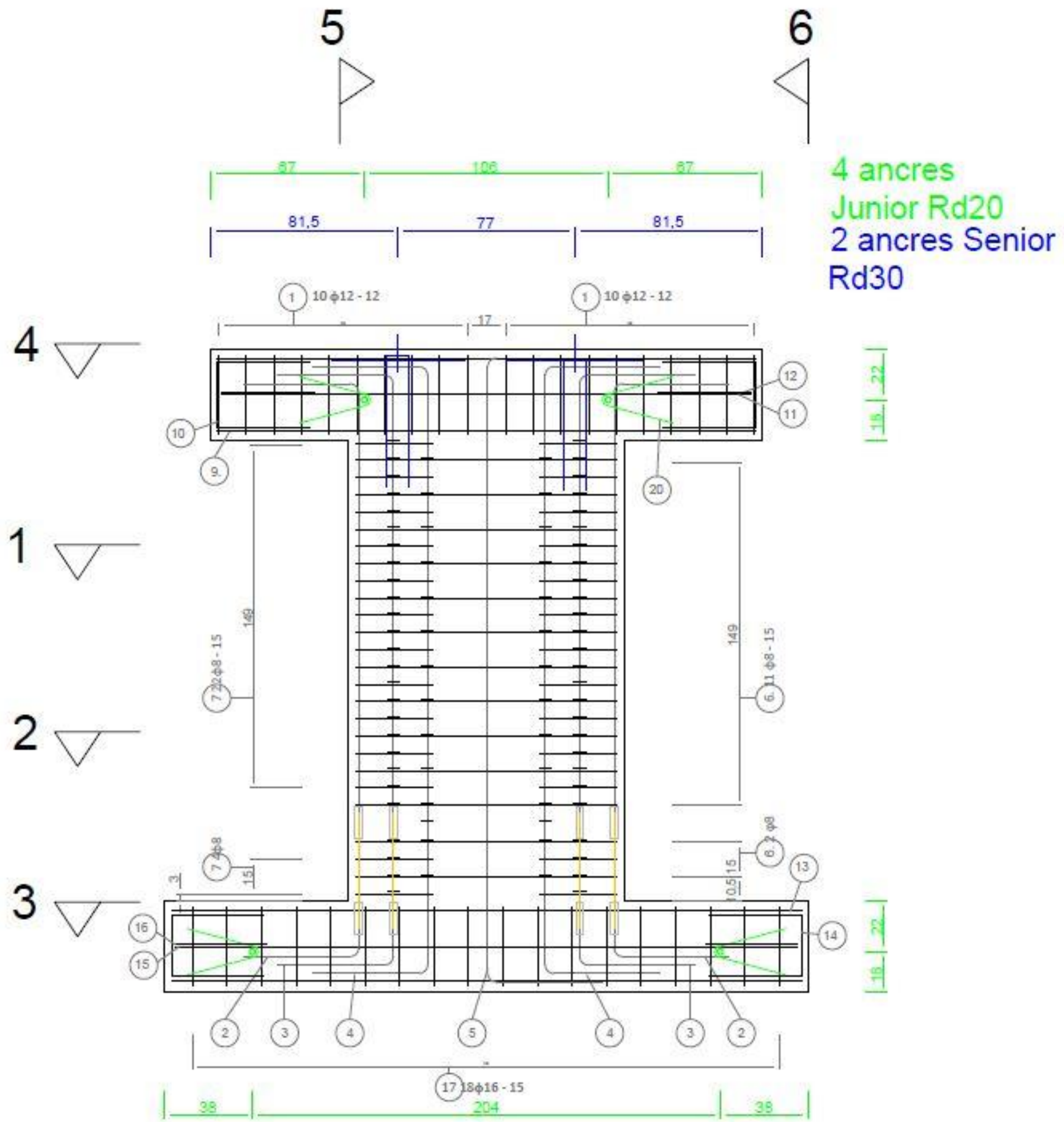

Volume pièce: 1.584 m3
Poids pièce: +- 4180 Kg
Qualité béton: C35/45
Enrobage: 3cm
∇ Face tirée manuellement
∇ Face lisse de décoffrage
PLAN DE REFERENCE
Armatures: croquis
Coffrage:

Date	Indice	Modification	Auteur

Dessiné par	Date	Echelle	Approuvé par	Date
Fabrice RIGOT	20/03/19			

TFE UCLouvain
Voile parasismique 2

Armatures

Coupe 1-1'

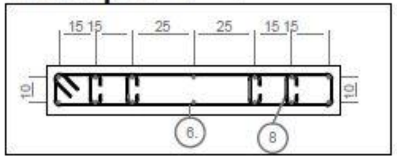

Coupe 2-2'

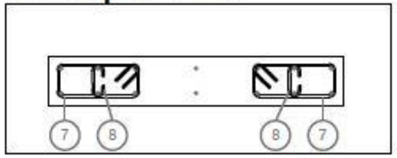

Coupe 3-3'

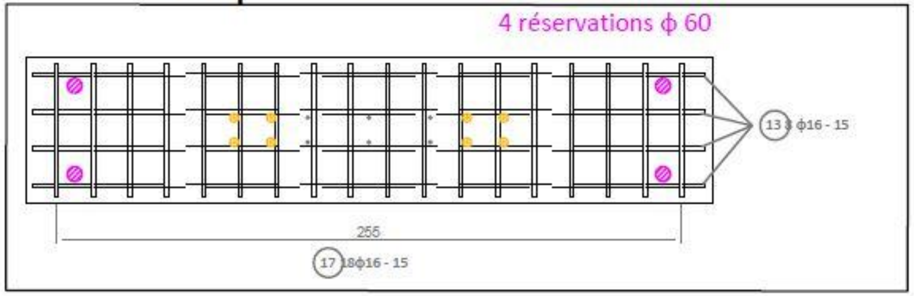

Coupe 4-4'

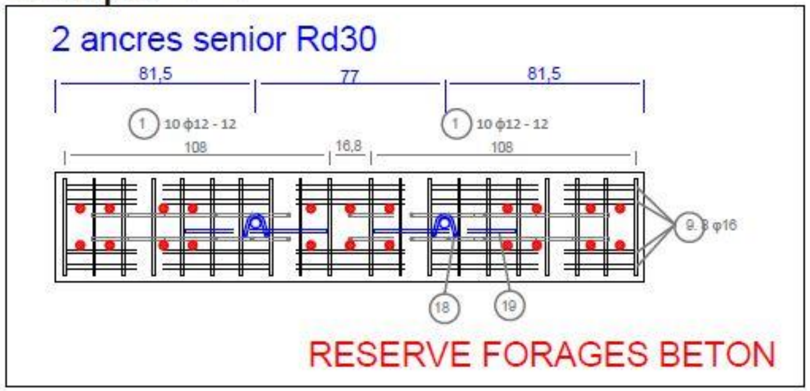

Coupe 5-5'

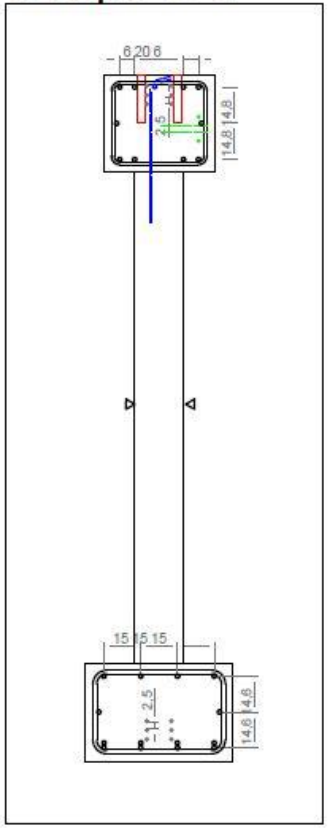

Coupe 6-6'

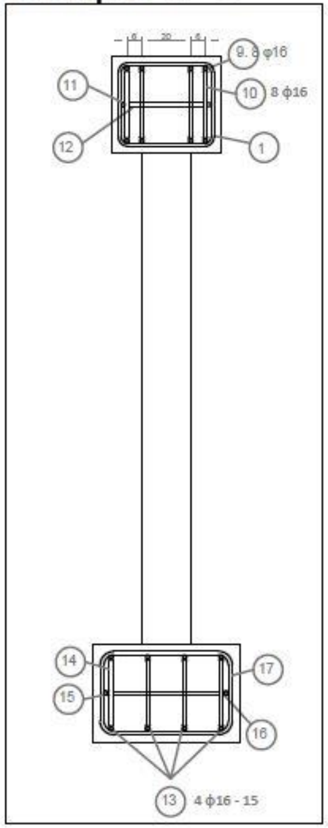

Volume pièce: 1.584 m3
Poids pièce: +- 4180 Kg
Qualité béton: C35/45
Enrobage: 3cm
▽ Face tirée manuellement
▽ Face lisse de décoffrage
PLAN DE REFERENCE
Armatures: croquis
Coffrage:

Date	Indice	Modification	Auteur
20/03/19	0		

Dessiné par	Date	Echelle	Approuvé par	Date
Fabrice RIGOT	20/03/19			

TFE UCLouvain
Voile parasismique 2

Armatures - COUPES

8.4 SMA element case 2: development

The total elongation of a basic SMA tension chord Δ_{TC} (Equation (12)) is developed for the case 2:

$$\Delta_{TC} = \int_{-\frac{srm}{2}}^{\frac{srm}{2}} \varepsilon_{sma}\, dx \qquad (12)$$

With *srm* the distance between 2 cracks

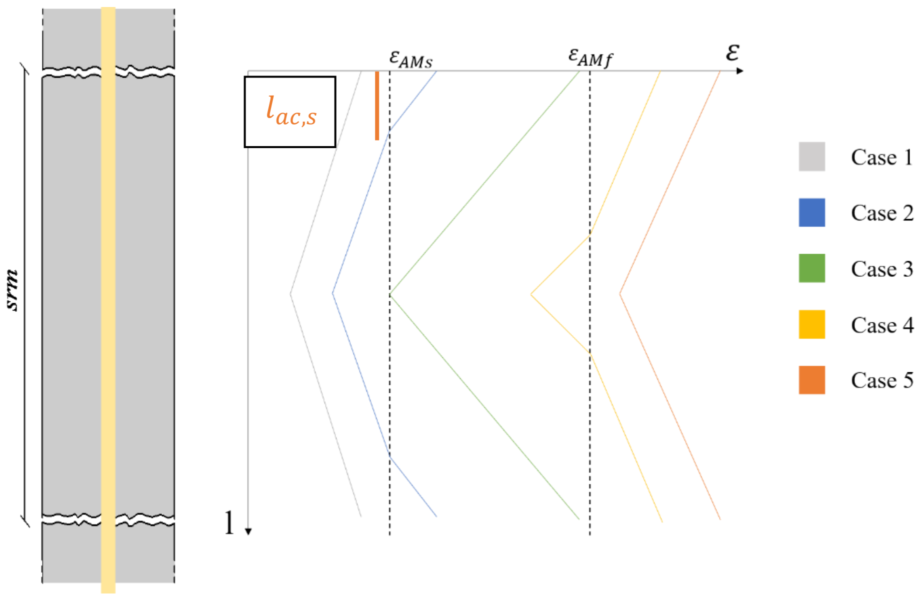

$$\Delta_{TC} = \left((\varepsilon_{ac} + \varepsilon_{AMs}) \times \frac{l_{ac,s}}{2} + \left(\varepsilon_{AMs} + \varepsilon_{\frac{srm}{2}}\right) \times \left(\frac{srm}{2} - l_{ac,s}\right) \times \frac{1}{2} \right) \times 2$$

$$\Delta_{TC} = \left((\varepsilon_{ac} + \varepsilon_{AMs}) \times l_{ac,s} + \left(\varepsilon_{AMs} + \varepsilon_{\frac{srm}{2}}\right) \times \left(\frac{srm}{2} - l_{ac,s}\right) \right)$$

$$\Delta_{TC} = \varepsilon_{ac} \times l_{ac,s} + \varepsilon_{AMs} \times \frac{srm}{2} + \varepsilon_{\frac{srm}{2}} \times \left(\frac{srm}{2} - l_{ac,s}\right)$$

With $l_{ac,s}$ is the length required to develop the plastic strain $\varepsilon_p = \varepsilon_{ac} - \varepsilon_{AMs}$:

$$l_{ac,s} = \frac{A_{sma} \cdot E_{AMf} \cdot (\varepsilon_{ac} - \varepsilon_{AMs})}{\tau_{b1} \cdot \pi \cdot \phi_l}$$

The strain at $\frac{srm}{2}$ can be calculated as such:

$$\varepsilon_{\frac{srm}{2}} = \varepsilon_{AMs} - \pi \tau_{b1} \emptyset \times \frac{\left(\frac{srm}{2} - l_{ac,s}\right)}{A_{sma} \times E_{AMf}}$$

The crack width *w* can then be deduced from Equation (11):

$$w = \int_{-\frac{srm}{2}}^{\frac{srm}{2}} \varepsilon_{sma} - \varepsilon_c \, dx \tag{11}$$

with ε_c the concrete strain

$$w = \Delta_{TC} - \int_{-\frac{srm}{2}}^{\frac{srm}{2}} \varepsilon_c \, dx$$

With:

$$\int_{-\frac{srm}{2}}^{\frac{srm}{2}} \varepsilon_c \, dx = \left(\varepsilon_{c,AMs} \times \frac{l_{ac,s}}{2} + \left(\varepsilon_{c,AMs} + \varepsilon_{c,\frac{srm}{2}}\right) \times \left(\frac{srm}{2} - l_{ac,s}\right) \times \frac{1}{2}\right) \times 2$$

$$\int_{-\frac{srm}{2}}^{\frac{srm}{2}} \varepsilon_c \, dx = \varepsilon_{c,AMs} \times l_{ac,s} + \left(\varepsilon_{c,AMs} + \varepsilon_{c,\frac{srm}{2}}\right) \times \left(\frac{srm}{2} - l_{ac,s}\right)$$

Then:

$$w = \Delta_{TC} - \varepsilon_{c,AMs} \times l_{ac,s} - \left(\varepsilon_{c,AMs} + \varepsilon_{c,\frac{srm}{2}}\right) \times \left(\frac{srm}{2} - l_{ac,s}\right)$$

$$w = \Delta_{TC} - \varepsilon_{c,AMs} \times \frac{srm}{2} - \varepsilon_{c,\frac{srm}{2}} \times \left(\frac{srm}{2} - l_{ac,s}\right)$$

With the concrete strain at $l_{ac,s}$ by equilibrium:

$$\varepsilon_{c,AMs} = \frac{\tau_{b1} \cdot \pi \cdot \phi_l \cdot l_{ac,s}}{A_c \cdot E_c}$$

And the concrete strain at $\frac{srm}{2}$ by equilibrium:

$$\varepsilon_{c,\frac{srm}{2}} = \varepsilon_{c,AMs} + \frac{\tau_{b1} \cdot \pi \cdot \phi_l \cdot (\frac{srm}{2} - l_{ac,s})}{A_c \cdot E_c}$$

For case 4 the development is the same expect that with only different values of $\varepsilon_{c,AMs}$ and $l_{ac,s}$.

8.5 Matlab code

8.5.1 Main

```
%% FILE Main

% This file plots the chord discretization, F-D response, Stress and strain
% profiles
clc
close all

%% EXPERIMENTAL DATA

% location of the experimental data
B = readtable('DIC_Fissure.xlsx');
X = table2array(B);
% Three experimental cases
X1 = X(:,5);
X2 = X(:,4);
X3 = X(:,1);
Y=[0,87,253,233,126,127,160,149,83,133,252,159,112,125];
Y=cumsum(Y);
y = 1:length(Y)*4;
x1 = y;
x2 = y;
x3 = y;
for i=1:length(Y)
    y(4*i)=Y(i)+30;
    y(4*i-1)=Y(i)+30;
    y(4*i-2)=Y(i)-30;
    y(4*i-3)=Y(i)-30;

    x1(4*i)=0;
    x1(4*i-1)=X1(i);
    x1(4*i-2)=X1(i);
    x1(4*i-3)=0;

    x2(4*i)=0;
    x2(4*i-1)=X2(i);
    x2(4*i-2)=X2(i);
    x2(4*i-3)=0;

    x3(4*i)=0;
    x3(4*i-1)=X3(i);
    x3(4*i-2)=X3(i);
    x3(4*i-3)=0;
end
%% EXPERIMENTAL: INPUT VARIABLES EXPERIMENTAL PLOTS

% Test unit for which the experimental results are plotted
% TU=[4];  %LAP-P1...P22-> TU=1..22, LAP-C1->TU=23, LAP-C2->TU=24
 LStep=[P(TU).NDI.LoadSteps([5,9]),10984]; %P(TU).NDI.LoadSteps(1);
% displacement at loadstep (required for comparing numerical and experimental results)
expF= 1:length(Delta_atLS);
Force_at_LS=P(TU).CAT.processed_channels(35).data(LStep);

% CONTROL F-D plot
% linecolor F plot
linecol_exp_FD={'b','r','g','m','c'};
% switch properties on =1 off=0 [failure splices, failure specimen, top casted]
switch_prop_FD=[0,0,0];

% CONTROL CRACK WIDTH plot
% line of LEDs to be used for the calculation of the crack width
LED_line='SE2'; % possibilities: NE1, NE2, NW1, NW2, SE1, SE2, SW1, SW2. The number (1,2)
differentiates the LEDs at the left and right of the holes. %For continuous reinforcement the
number 1 or 2 yields the same result
linecol_exp_CW={'b','r','g','m','c'};

% CONTROL EXP STRAIN plot;
LAP_LOC='SE'; % possibilities: NE, NW, SE, SW
linecol_exp_SP={'b','r','g','m','c'};
```

```matlab
%% NUMERICAL: INPUT DATA

% STEEL MATERIAL PROPERTIES
steel_prop.Es=204000; %MPa Elastic modulus longitudinal reinforcement
steel_prop.fy=510; %MPa Yield force longitudinal reinforcement
steel_prop.fu=635;%MPa Ultimate stress longitudinal reinforcement
steel_prop.epsu=9/100; % [-] Ultimate strain longitudinal reinforcement
steel_prop.epsy=steel_prop.fy/steel_prop.Es; % [-] Yield strain longitudinal reinforcement
 steel_prop.b=(steel_prop.fu-steel_prop.fy)/(steel_prop.epsu-steel_prop.epsy)/steel_prop.Es; %
[-] Post yield slope
steel_prop.Esh=steel_prop.Es*steel_prop.b; %MPa [-] Post yield young modulus

%SMA MATERIAL PROPRETIES
SMA_prop.f1=300; %MPa stress at first configuration change
SMA_prop.f2=400; %MPa stress at seconde configuration change

SMA_prop.eps1=0.01;% [-] strainat first configuration change
SMA_prop.eps2=0.05;% [-] strainatat seconde configuration change

SMA_prop.E1=SMA_prop.f1/SMA_prop.eps1;%MPa Elastic modulus
SMA_prop.E2=(SMA_prop.f2-SMA_prop.f1)/(SMA_prop.eps2-SMA_prop.eps1);%MPa Elastic modulus
SMA_prop.E3=17460;%MPa Elastic modulus


SMA_prop.fu=1001;%MPa Ultimate stress longitudinal reinforcement
SMA_prop.Dim=12.7;%mm diameter of the longitudinal rebar
SMA_prop.A=4*pi*SMA_prop.Dim^2/4;
% CONCRETE MATERIAL PROPERTIES
conc_prop.fc=49.17; %MPa % concrete compressive strength
conc_prop.fct=0.3*conc_prop.fc^(2/3); %MPa % concrete tensile strength
conc_prop.Ec=5000*conc_prop.fc^(1/2); %MPa % concrete Young modulus

% BOND MATERIAL
bond_prop.taub0=conc_prop.fct*2; % bond prior to rebar yielding
bond_prop.taub1=bond_prop.taub0/2; % bond post rebar yielding

% TU LAYOUT AND REINFORCEMENT PROPERTIES
TUlr.L0=2000; % mm specimen height
TUlr.Lfound= 400; %mm foundation height
TUlr.bfound=200; %mm foundation width
TUlr.l0=255; %mm length of straight anchored rebar
TUlr.dbl=12; %mm diameter of the longitudinal rebar
TUlr.lanc=TUlr.l0; %mm actual embedment length of the rebar anchored in the foundation of top
beam bloc
TUlr.b=200; %mm % side of the cross section
TUlr.nbars=4; % number of longitudinal rebars
TUlr.Atot=TUlr.b^2; % total sectional area
TUlr.As=TUlr.nbars*pi*TUlr.dbl^2/4; % steel area outside lap region
TUlr.Ac=TUlr.Atot-TUlr.As; % concrete area
TUlr.rhol=TUlr.As/TUlr.Atot; % reinforcement ratio
TUlr.srm0=TUlr.dbl*conc_prop.fct*(1-TUlr.rhol)/(2*bond_prop.taub0*TUlr.rhol); % maximum length
over which forces are transferred at cracking
TUlr.lambda=0.9; % parameter mutiplying srm0 to obtain srm. lamda [0.5,1]
TUlr.ls=280; % LAP splice length

% BOND SMA MATERIAL
% Sand_Alpha = 2/0.6;
% bondSMA.taub0= (1.25-0.025*SMA_prop.Dim)*(conc_prop.fc)^(1/2);
% kr =(0.17*Sand_Alpha^2-1.92*Sand_Alpha+6.5);
kr =1;
bondSMA.taub0=kr*(0.9-0.004*SMA_prop.Dim-
0.0025*TUlr.ls+0.015*50/SMA_prop.Dim)*(conc_prop.fc)^(1/2);
bondSMA.taub1=bondSMA.taub0/3;
TUlr.srmSMA=SMA_prop.Dim*conc_prop.fct*(1-TUlr.rhol)/(2*bondSMA.taub0*TUlr.rhol);


%% NUMERICAL: definition of vector of crack locations

srm_vector_input =[341,233,126,127,160,149,83,133,252,159,112,125];
if sum(srm_vector_input)==TUlr.L0
srm_vector=[TUlr.lanc,srm_vector_input,TUlr.lanc];
else
    sprintf('Sum srm_vec is: %d, the difference with L0 is
%d',sum(mid_srmvec),sum(mid_srmvec)-TUlr.L0)
    error('Sum of baseic TC portions different from L0')
end
```

```
[srm_vector,srm_vector_LAP] = DISCRETIZATION_TC_visualization_LAP(TUlr,srm_vector);
%[srm_vector,srm_vector_LAP] = DISCRETIZATION_TC_visualization_LAP(TUlr); %Automatic mesher
depending on the value of lambda

%% RUN NUMERICAL MODEL AND EXTRACT EXPERIMENTAL VALUES FOR FOLLWING 2 PLOTS
% run mechanical model and save 3 d matrix for the crack widths
for j=1:length(Delta_atLS)
%%%%%%%%%%%%%%%%%%%%%%%%%%%%%%%%%%%%%%%%%%%%%%%%%%%%%%%%%%%%%%%%%
%COMPUTE Numerical model (crack widths and strains distributions)
delta_tot=Delta_atLS(j); %mm  conc_prop.fct/conc_prop.Ec*TUlr.L0
max_ite=300; % maximum number of iterations accepted
tol=0.2;
pts_discr=100; % points in which the basic TC and the anchorages are discretized
[w_matrix(:,:,j),epsS_matrix(:,:,j),epsC_matrix,eps_atc,N_applied,delta_LAP
]=COMPUTE_from_displ_to_strain_LAP(delta_tot,srm_vector,srm_vector_LAP,TUlr,steel_prop,conc_pr
op,bond_prop,pts_discr,max_ite,tol,SMA_prop,bondSMA);
% w_matrix(:,1,j)=cumsum([0,srm_vector_input]);
expF(j)=N_applied;
%%%%%%%%%%%%%%%%%%%%%%%%%%%%%%%%%%%%%%%%%%%%%%%%%%%%%%%%%%%%%%%%%
end

%% FIGURE 2: CRACK WIDTH
Fig1=figure;

set(Fig1,'renderer','painters')

% fs=8;
fs=12;
fn='Times New Roman';

set(0,'DefaultAxesFontName',fn)
set(0,'DefaultAxesFontSize',fs)
set(0,'DefaultTextFontSize',fs)
set(0,'DefaultTextFontName',fn)

%Units
%inches | centimeters | normalized | points | {pixels} | characters
%Units of measurement. Specifies the units MATLAB uses to interpret size and location data.
All units are measured from the lower-left corner of the window.
set(gcf,'Units','Centimeters');
% Position on screen and dimensions of outer box [a b c d]
set(gcf,'Position',[11 7 16/3 7]);
% the dimension of the plot on the screen are the same of those in the paper
%set(gcf,'PaperPositionMode','auto');

%%%%%%%%%%%%%%%%%%%%%%%%%%%%%%%%%%%%%%%%%%%%%%%%%%%%%%%%%%%%%%%%%%%%%%%%%%%%%
% PLOT STUFF
figure(2)
% % plot numerical crack widths  case 1
barh(w_matrix(:,1,1),w_matrix(:,2,1),0.15,'g'); hold on
% % plot numerical crack widths case 2
 barh(w_matrix(:,1,2),w_matrix(:,2,2),0.15,'b'); hold on
 % % plot numerical crack widths case 3
 barh(w_matrix(:,1,3),w_matrix(:,2,3),0.15,'r'); hold on

%  plot experimental crack widths
plot(x1,y,'g--');
 plot(x2,y,'b--');
plot(x3,y,'r--');

stairs([EXP_cw(1,j);EXP_cw(:,j);0],[yvec_LEDs';yvec_LEDs(end)],'g:'); hold on
f21(1)=plot([110,110],[1,1],'k');
f21(2)=plot([110,110],[1,1],'k:');
f21(3)=plot([110,110],[1,1],'g');
f21(4)=plot([110,110],[1,1],'b');
f21(5)=plot([110,110],[1,1],'r');

w=0.76;
h=0.85;
leg=legend(f21,'Num.','Exp.','A','B','C');
leg=legend(f21,'Num.','Exp.','A');
legend boxoff
set(leg,'fontsize',fs)
set(leg,'Color',[1 1 1]);
set(leg,'Units','normalized');
set(leg,'Position',[0.54 0.48 0.39 0.25]);
grid on
```

```
set(gcf,'units','centimeters','OuterPosition',[0 0 10 20]);
ylabel('Crack height (mm)','fontsize',fs);
xlabel('Crack width (mm)','fontsize',fs);
xlim([0 4]);
ylim([0 2000]);
% %%%%%%%%%% BOTTOM AND LEFT AXES %%%%%%%%%%%%%%
%positioning the plot in the outer box
ax1=gca;
set(gca,'Position',[0.2 0.13     w    h]);
axis([0,0.8,-10,TU1r.L0+10]);
X=get(ax1,'XLim'); Y=get(gca,'YLim');

% set(ax1,'xtick',[])
% set(ax1,'xticklabel',[]);
% set(ax1,'ytick',[])
% set(ax1,'yticklabel',[]);
set(ax1,'XAxisLocation','bottom');
set(ax1,'YAxisLocation','left');
%set(ax1,'Color','none'); %background: no color

%YL=ylabel(['Mean {\it' char(949) '_{ls}} [-]']);
YL=ylabel(['TU height {\ith} [mm]']);
set(YL,'Units','normalized')
set(YL,'HorizontalAlignment','center')
set(YL,'VerticalAlignment','Middle')
% position of the axes' text [x,y,z] (relative coord with respect to to axes lenght)
set(YL,'Position',[-0.22 0.5  0])

XL=xlabel('Crack width {\itw} [mm]');
set(XL,'Units','normalized')
set(XL,'HorizontalAlignment','center')
set(XL,'VerticalAlignment','Middle')
% position of the axes' text [x,y,z] (relative coord with respect to to axes lenght)
set(XL,'Position',[0.5 -0.11 0])


set(ax1,'YMinorTick','on')
set(ax1,'XMinorTick','on')
set(ax1,'TickLength',[0.03 1])
set(ax1,'ytick',[0:400:1260])
set(ax1,'xtick',[0:0.2:0.6])
% set(ax1,'xticklabel',[1:4:length(LoadSteps)]);



%%%%%%%%%% TOP AND RIGHT AXES %%%%%%%%%%%%%%
ax1b=axes('Position',get(ax1,'Position'));

set(ax1b,'YLim',get(ax1,'YLim'))
set(ax1b,'XLim',X)
set(ax1b,'XAxisLocation','top');
set(ax1b,'YAxisLocation','right');
set(ax1b,'Color','none'); %background: no color

XL2=xlabel([]);
set(XL2,'Units','normalized')
set(XL2,'HorizontalAlignment','center')
set(XL2,'VerticalAlignment','Middle')
set(XL2,'Position',[0.5 1.14 0])

YL2=ylabel([]);
set(YL2,'Units','normalized')
set(YL2,'HorizontalAlignment','center')
set(YL2,'VerticalAlignment','Middle')
set(YL2,'Position',[1.08 0.5  0])

set(ax1b,'YMinorTick','on')
set(ax1b,'XMinorTick','on')
set(ax1b,'TickLength',[0.03 1])
%set(ax1b,'xtick',[])
set(ax1b,'ytick',[0:400:1260])
set(ax1b,'xtick',[0:0.2:0.6])
set(ax1b,'xticklabel',[]);
set(ax1b,'yticklabel',[]);

print(Fig1,'crack_width_25','-depsc')
%%%%%%%%%%%%%%%%%%%%%%%%%%%%%%%%%%%%%%%%%%%%%%%
```

```
% Steel and SMA strain

figure(3)
np=10; %points between markers

j=1;
a=epsS_matrix(:,1,j);
a(end-100);
% numerical
plot(epsS_matrix(:,2,j),epsS_matrix(:,1,j),'g'); hold on

j=2;
a=epsS_matrix(:,1,j);
a(end-100);
% % numerical
 plot(epsS_matrix(:,2,j),epsS_matrix(:,1,j),'b'); hold on

j=3;
% numerical
plot(epsS_matrix(:,2,j),epsS_matrix(:,1,j),'r'); hold on
a=epsS_matrix(:,1,j);
a(end-100);

f3l(1)=plot([110,110],[1,1],'g'); hold on
f3l(2)=plot([110,110],[1,1],'b'); hold on
f3l(3)=plot([110,110],[1,1],'r'); hold on

w=0.76;
h=0.86;

% leg=legend(f3l,'A','B','C');
legend boxoff
set(leg,'fontsize',fs)
set(leg,'Color',[1 1 1]);
set(leg,'Units','normalized');
grid on
ax = gca;
ax.YTick =([-200:200:2200]);
set(gcf,'units','centimeters','OuterPosition',[10 0 10 20]);
ylim([-200 2200]);
xlim([0 0.07]);
ylabel('Height (mm)','fontsize',fs);
xlabel('Strain (-)','fontsize',fs);
%%%%%%%%%%%%%%%%%%%%%%%%%%%%%%%%%%%%%%%%%%%%%%
% CALCULATION
 delta_vector=linspace (0,20,20);
 N_applied =  delta_vector;
[X,Y,x,y] = Exp();

max_ite=1000; % maximum number of iterations accepted
tol=1;
pts_discr=100; % points in which the basic TC and the anchorages are discretized

defining delta_lim using predictive equation
if ls/TUlr.dbl+(60-25)/0.3*rhot*100-60>0
delta_ls_limit=(-23+50*rhot*100+0.44*ls/TUlr.dbl)/1000*ls; % [mm] predictive equation
SUBDOMAIN A
else
delta_ls_limit=(1.2+0.04*ls/TUlr.dbl)/1000*ls;     % [mm] predictive equation SUBDOMAIN B
end

for j=1:length(delta_vector)
    [w_matrix(:,:,j),epsS_matrix(:,:,j),epsC_matrix,eps_atc,N_applied(j),delta_LAP
]=COMPUTE_from_displ_to_strain_LAP(delta_vector(j),srm_vector,srm_vector_LAP,TUlr,steel_prop,c
onc_prop,bond_prop,pts_discr,max_ite,tol,SMA_prop,bondSMA);

[~,~,~,N_applied(j),~]=COMPUTE_from_displ_to_strain_LAP(delta_vector(j),srm_vector,srm_vector_
LAP,TUlr,steel_prop,conc_prop,bond_prop,pts_discr,max_ite,tol(j),SMA_prop,bondSMA);
    if delta_LAP >= delta_ls_limit
        N_applied(j)=0;
        delta_vector(j+1:end)=[];
        break
    else
    end
 end
%%%%%%%%%%%%%%%%%%%%%%%%%%%%%%%%%%%%%%%%%%%%%
PLOT
```

```
figure(4)
plot(delta_vector,N_applied/1000,'k-'); hold on

plot(Delta_atLS(1),expF(1)/1000,'ko','markersize',4,'markerfacecolor','g'); hold on
plot(Delta_atLS(2),expF(2)/1000,'ko','markersize',4,'markerfacecolor','b'); hold on
plot(Delta_atLS(3),expF(3)/1000,'ko','markersize',4,'markerfacecolor','r'); hold on

w=0.76;
h=0.85;
ylim([0 300]);
xlim([0 25]);
grid on
ylabel('Force(kN)','fontsize',fs);
xlabel('Displacement (mm)','fontsize',fs);
set(gcf,'units','centimeters','OuterPosition',[20 0 10 20]);
leg=legend(f1l,'Experimental','Numerical','TU Failure','\Delta = 2 mm','\Delta = 3 mm','\Delta
= 4 mm');
legend boxoff
set(leg,'fontsize',fs)
set(leg,'Color',[1 1 1]);
set(leg,'Units','normalized');
set(leg,'Position',[ 0.63 0.35 0.1 0.1]);
```

8.5.2 From displacement to strain

```
function [w_matrix,epsS_matrix,epsC_matrix,eps_atc,N_applied,delta_ls ] =
COMPUTE_from_displ_to_strain_LAP(delta_tot,srm_vector,srm_vector_LAP,TUlr,steel_prop,conc_prop
,bond_prop,pts_discr,max_ite,tol,SMA_prop,bondSMA)
% This function computes the steel and concrete strain of the entire
% tension chord (+ the anchorages). it uses the functions compute
% delta_TC_basic and delta_anc

%% shortening variables name
Es=steel_prop.Es; %MPa Elastic modulus longitudinal reinforcement
fy=steel_prop.fy; %MPa Yield force longitudinal reinforcement
fu=steel_prop.fu;%MPa Ultimate stress longitudinal reinforcement
epsu=steel_prop.epsu; % [-] Ultimate strain longitudinal reinforcement
epsy=steel_prop.epsy; % [-] Yield strain longitudinal reinforcement
Esh=steel_prop.Esh;

fc=conc_prop.fc; %MPa % concrete compressive strength
fct=conc_prop.fct; %MPa % concrete tensile strength
Ec=conc_prop.Ec; %MPa % concrete Young modulus

tau_b0=bond_prop.taub0; % bond prior to rebar yielding
tau_b1=bond_prop.taub1; % bond post rebar yielding

dbl=TUlr.dbl; %  [mm] diameter longitudinal rebar
l0=TUlr.l0; % [mm] anchorage length
srm0=TUlr.srm0;% max crack width
srmSMA=TUlr.srmSMA;
rhol=TUlr.rhol; % confining reinforcmeent ratio
As=TUlr.As; % total steel area (4*Abar)
Ac=TUlr.Ac; % total steel area (4*Abar)
nbars=TUlr.nbars; % number of longitudinal bars
L0=TUlr.L0; % Column height [mm]
lanc=TUlr.lanc; % anchorage length
SMADim=SMA_prop.Dim;

EAeq=Es*As+Ec*Ac;

%% INITIAL CALCULATIONS: determination displacement at first crack and minimum displacement to
have everithing cracked

% displacement at first crack
delta_FC=fct/Ec*L0;

% displacement due to anchorage when all tension chord is cracked (only extremities are
cracked at lap splice zone)
eps_atc=fct*EAeq/(Ec*Es*As);
switch_plot_strain_anc='off'; %possibilities : 'on', 'off' to enable/disable plot of the
strains in the anchored rebars
[delta_anc,~,~] =
COMPUTE_Delta_anc(eps_atc,pts_discr,TUlr,steel_prop,conc_prop,bond_prop,switch_plot_strain_anc
);
delta_AC_anc=2*delta_anc;
% displacement due to tension chord when all crack are formed
% b) Evaluation of how many different basic tension chord models exist
[srm_TC,~,ic]=unique(srm_vector([length(srm_vector_LAP)+2:end-1])); %srm_tc is the vector of
different basic length
a_counts = accumarray(ic,1);
value_counts = [srm_TC', a_counts]; % matrix having in I column srm_tc and in 2 column the
number of times in which the basic length occurs
% c) Calculation of the basic TC displacement for each one of them
switch_plot_strain_TC='off'; %possibilities : 'on', 'off' to enable/disable plot of the
strains in the basic TC model
for j=1:length(srm_TC)
    [delta_tcb(j),~,~,~,~] =
COMPUTE_Delta_TC_basic(eps_atc,srm_TC(j),pts_discr,TUlr,steel_prop,conc_prop,bond_prop,switch_
plot_strain_TC);
end
% d) Compute the total displacement associated with the assumed strain at crack
delta_AC_TC=delta_tcb*a_counts;
% displacement due to lap splice region
switch_plot_strain_LAP='off';
delta_ls_tot = 0;
for j=1:length(srm_vector_LAP)
```

```
[delta_ls_AC(j),~,~,~,~] =
COMPUTE_Delta_LAP(eps_atc,srm_vector_LAP(j),pts_discr,TUlr,steel_prop,conc_prop,bond_prop,swit
ch_plot_strain_LAP,SMA_prop,bondSMA);
delta_ls_tot = delta_ls_AC(j) + delta_ls_tot;
end
delta_AC=delta_AC_TC+delta_AC_anc+delta_ls_tot;


%% MAIN CALCULATIONS:

%%%%%%%%%%%%%%%%%%%%%%%%%%%%%%%%%%%%%%%%%%%%%%%%%%%%%%%%%%%%%%%%%%%%%%%%%%%%%%%%%%%%%%%%%%%%%%%%%%
% case 1: applied displacement smaller than displacement required for first crack
%%%%%%%%%%%%%%%%%%%%%%%%%%%%%%%%%%%%%%%%%%%%%%%%%%%%%%%%%%%%%%%%%%%%%%%%%%%%%%%%%%%%%%%%%%%%%%%%%%

if delta_tot<=delta_FC % applied displacement smaller than displacement at first crack
    w_matrix=([[0;cumsum(srm_vector(2:end-1))'],zeros(length(srm_vector)-1,1)]); % cracks
location: NO CRACKS
    srm_all_discr=linspace(-lanc,L0+lanc,pts_discr*length(srm_vector));

epsS_matrix=[srm_all_discr',[zeros(pts_discr,1);delta_tot/L0*ones(pts_discr*(length(srm_vector
)-
2),1);zeros(pts_discr,1)],[zeros(pts_discr,1);delta_tot/L0*ones(pts_discr*(length(srm_vector)-
2),1);zeros(pts_discr,1)]];
    epsC_matrix=epsS_matrix;
    eps_atc=delta_tot/L0;
    N_applied=eps_atc*EAeq;
    delta_ls=delta_tot*ls/L0;

%%%%%%%%%%%%%%%%%%%%%%%%%%%%%%%%%%%%%%%%%%%%%%%%%%%%%%%%%%%%%%%%%%%%%%%%%%%%%%%%%%%%%%%%%%%%%%%%%%
    % case 2: applied displacement in between displacement at first crack and displacement
where tension chord is fully cracked
%%%%%%%%%%%%%%%%%%%%%%%%%%%%%%%%%%%%%%%%%%%%%%%%%%%%%%%%%%%%%%%%%%%%%%%%%%%%%%%%%%%%%%%%%%%%%%%%%%

else if delta_tot>delta_FC && delta_tot<delta_AC
        % these results are fake, it will be assumed in this stage that the section is still
homogenized and that cracks are still not open (although they are opening one at a time)
        w_matrix=([[0;cumsum(srm_vector(2:end-1))'],zeros(length(srm_vector)-1,1)]); % cracks
location: only some cracks are opened
        srm_all_discr=linspace(-lanc,L0+lanc,pts_discr*length(srm_vector));
        if length(srm_vector_LAP) == 1
         epsiSMA=delta_tot/L0*210/30;

epsS_matrix=[srm_all_discr',[zeros(pts_discr,1);delta_tot/L0*ones(45,1);(epsiSMA)*ones(pts_dis
cr+51,1);delta_tot/L0*ones(pts_discr*(length(srm_vector)-3)-
96,1);zeros(pts_discr,1)],[zeros(pts_discr,1);delta_tot/L0*ones(pts_discr*(length(srm_vector)-
2),1);zeros(pts_discr,1)]];
        else

epsS_matrix=[srm_all_discr',[zeros(pts_discr,1);delta_tot/L0*ones(pts_discr*(length(srm_vector
)-
2),1);zeros(pts_discr,1)],[zeros(pts_discr,1);delta_tot/L0*ones(pts_discr*(length(srm_vector)-
2),1);zeros(pts_discr,1)]];
        end
        epsC_matrix=epsS_matrix;
        eps_atc=fct*EAeq/(Ec*Es*As);
        N_applied=eps_atc*Es*As;
        delta_ls=delta_tot*ls/L0;

%%%%%%%%%%%%%%%%%%%%%%%%%%%%%%%%%%%%%%%%%%%%%%%%%%%%%%%%%%%%%%%%%%%%%%%%%%%%%%%%%%%%%%%%%%%%%%%%%%
        % case 3: applied displacement larger than displacement where tension chord fully
cracked
%%%%%%%%%%%%%%%%%%%%%%%%%%%%%%%%%%%%%%%%%%%%%%%%%%%%%%%%%%%%%%%%%%%%%%%%%%%%%%%%%%%%%%%%%%%%%%%%%%
    else
        %%  NR PROCEDURE

        % 1) Determination of the first attempt strain at crack
        eps_atc=0.00185;
        iteration=0;
        convergence=0;
        % BEGINNING OF THE NR PROCEDURE
        while convergence==0 && iteration<max_ite
            % 2) Calculation of the displacement, strain and crack width of the anchorage
            switch_plot_strain_anc='off'; %possibilities : 'on', 'off' to enable/disable plot
of the strains in the anchored rebars
            [delta_anc,epsanc_discr,lanc_discr] =
COMPUTE_Delta_anc(eps_atc,pts_discr,TUlr,steel_prop,conc_prop,bond_prop,switch_plot_strain_anc
);
```

```
            delta_tot_anc=2*delta_anc;
            % 3) Evaluation of how many different basic tension chod models exist
            [srm_TC,ia,ic]=unique(srm_vector([length(srm_vector_LAP)+2:end-1])); %srm_tc is
the vector of different basic length
            a_counts = accumarray(ic,1);
            value_counts = [srm_TC', a_counts]; % matrix having in I column srm_tc and in 2
column the number of times in which the basic length occurs
            % 4) Calculation of the basic TC displacement for each one of them
            switch_plot_strain_TC='off'; %possibilities : 'on', 'off' to enable/disable plot
of the strains in the basic TC model
            for j=1:length(srm_TC)
                [delta_tcb(j),w_tcb(j),epsS_discr(:,j),epsC_discr(:,j),srm_discr(:,j)] =
COMPUTE_Delta_TC_basic(eps_atc,srm_TC(j),pts_discr,TUlr,steel_prop,conc_prop,bond_prop,switch_
plot_strain_TC);
            end
            % 5) Compute the total displacement associated with the assumed strain at crack
            delta_tot_TC=delta_tcb*a_counts;

            % 6) Calculation of the displacement for the lap splice region
            delta_ls_tot = 0;
            switch_plot_strain_LAP='off';
            for j=1:length(srm_vector_LAP)
            [delta_ls(j),w_ls(j),epsS_discr_BOT(:,j),epsS_discr_TOP(:,j),ls_discr(:,j)] =
COMPUTE_Delta_LAP(eps_atc,srm_vector_LAP(j),pts_discr,TUlr,steel_prop,conc_prop,bond_prop,swit
ch_plot_strain_LAP,SMA_prop,bondSMA);
            delta_ls_tot = delta_ls(j) + delta_ls_tot;
            end
            if length(srm_vector_LAP) == 1
                delta_ls_tot = delta_ls_tot/(1.4);
            end
%             6) Tolerance check and possible update of the strain at crack
             a=delta_tot_anc+delta_tot_TC+delta_ls_tot;
             residual=delta_tot-(delta_tot_anc+delta_tot_TC+delta_ls_tot);

            if abs(residual)<tol
                iteration=iteration+1;
                convergence=1;
                sprintf(['Residual : ',num2str(residual), 'mm'])
                sprintf(['Convergence!! @ iteration: ',num2str(iteration)])
                % put together matrix of crack widths and strains (I column: locations, II
column: values of crack widths and strains)
                % crack associated to each portion (either anchorage or basic tc)
                w_portions=zeros(1,length(srm_vector));
                w_portions([1,end])=delta_anc;%first and last portion equal to anchorage width

                % steel and concrete strain associated to each portion
                epsS_portion=zeros((length(srm_vector)-length(srm_vector_LAP)+1)*pts_discr,1);
                epsC_portion=zeros((length(srm_vector)-length(srm_vector_LAP)+1)*pts_discr,1);
                epsS_portion(1:pts_discr)=fliplr(epsanc_discr); % first portion equal to
anchorage length
                epsS_portion(length(epsS_portion)-
pts_discr+1:length(epsS_portion))=epsanc_discr; % last portion equal to anchorage width
                epsS_portion(pts_discr+1:2*pts_discr)=epsS_discr_BOT; % second portion portion
equal to lap length (BOTTOM ANCHORED)

                srm_portion=zeros((length(srm_vector)-length(srm_vector_LAP)+1)*pts_discr,1);
                srm_portion(1:pts_discr)=fliplr(lanc_discr)*-1; % first portion equal to
anchorage width
                srm_portion(length(srm_portion)-
pts_discr+1:length(srm_portion))=L0+lanc_discr; % last portion equal to anchorage width
                srm_portion(pts_discr+1:2*pts_discr)=ls_discr; % second portion portion equal
to lap length (BOTTOM ANCHORED)
                k=2; % counter for the epsS, epsC and srm portions

                crack_h=cumsum(srm_vector(2:end-1));
                for j=length(srm_vector_LAP)+2:length(srm_vector)-1
                    idx= srm_TC==srm_vector(j);
                    w_portions(j)=w_tcb(idx);
                    epsS_portion(pts_discr*k+1:pts_discr*(k+1))=epsS_discr(:,idx);
                    epsC_portion(pts_discr*k+1:pts_discr*(k+1))=epsC_discr(:,idx);

srm_portion(pts_discr*k+1:pts_discr*(k+1))=srm_discr(:,idx)+srm_vector(j)/2+crack_h(k-1);
                    k=k+1;
                end
                % lump cracks into their location
                if length(srm_vector_LAP) == 1
                w_matrix=zeros(length(srm_vector)-1,2);
```

```
                w_matrix(:,1)=[0,cumsum(srm_vector(2:end-1))]; % cracks location
                w_matrix(1,2)= w_portions(1)+w_ls(1)/(1.4); % cracks width foundation
interface
                w_matrix(end,2)=w_portions(end)+(w_portions(end-1))/2; % cracks width top beam
interface
                w_matrix(length(w_ls)+1:end-1,2)=(w_portions(length(w_ls)+1:end-
2)+w_portions(length(w_ls)+2:end-1))/2; % cracks width above lap splice region
                else
                w_matrix=zeros(length(srm_vector)-1,2);
                w_matrix(:,1)=[0,cumsum(srm_vector(2:end-1))]; % cracks location
                w_matrix(1,2)=w_portions(1)+w_ls(1); % cracks width foundation interface
                w_matrix(end,2)=w_portions(end)+(w_portions(end-1))/2; % cracks width top beam
interface
                w_matrix(length(w_ls),2)=w_ls(end)+(w_portions(length(w_ls)+1))/2; % crack
width top lap splice interface
                w_matrix(2:length(srm_vector_LAP),2)=w_ls(2:end-1); % crack width within lap
splices
                w_matrix(length(w_ls)+1:end-1,2)=(w_portions(length(w_ls)+1:end-
2)+w_portions(length(w_ls)+2:end-1))/2; % cracks width above lap splice region
                end
                % create one eps_portion in which in the strain in the lap region is the one
of the top anchored rebar
                epsS_portion_TOP=epsS_portion;
                epsS_portion_TOP(pts_discr+1:2*pts_discr)=epsS_discr_TOP; % second portion
portion equal to anchorage length (BOTTOM ANCHORED)

                epsS_matrix=([srm_portion,epsS_portion,epsS_portion_TOP]);
%                 epsS_matrix=([srm_portion,epsS_portion]);
                epsC_matrix=([srm_portion,epsC_portion]);

                % compute total force
                if eps_atc<=epsy
                    N_applied=eps_atc*Es*As;
                else
                    N_applied=epsy*Es*As+(eps_atc-epsy)*Esh*As;
                end

            else
%                 sprintf(['Residual : ',num2str(residual), 'mm'])
                iteration=iteration+1;
                eps_atc=eps_atc+0.0001;
            end

        end

    end % end elseif

end % end if
end
```

8.5.3 SMA element

```
 function [ delta_ls,w_ls,epsS_discr_BOT,epsS_discr_TOP,ls_discr] = COMPUTE_Delta_SMA(
eps_atc,srm_LAP,pts_discr,TUlr,steel_prop,conc_prop,bond_prop,switch_plot_strain_LAP,SMA_prop,
bondSMA)
% This function computes the total elongation of the basic part of a tension
% chord model (part comprised between 2 cracks, length of srm) given the
% strain at crack eps_atc. It also outputs the crack width and the SMA and concrete strains

%% shortening variables name
Es=steel_prop.Es; %MPa Elastic modulus longitudinal reinforcement
fy=steel_prop.fy; %MPa Yield force longitudinal reinforcement
fu=steel_prop.fu;%MPa Ultimate stress longitudinal reinforcement
epsu=steel_prop.epsu; % [-] Ultimate strain longitudinal reinforcement
Esh=steel_prop.Esh;
epsys=steel_prop.epsy;

fc=conc_prop.fc; %MPa % concrete compressive strength
fct=conc_prop.fct; %MPa % concrete tensile strength
Ec=conc_prop.Ec; %MPa % concrete Young modulus

tau_b0=bond_prop.taub0; % bond prior to rebar yielding
tau_b1=bond_prop.taub1; % bond post rebar yielding

dbl=TUlr.dbl; %  [mm] diameter longitudinal rebar
l0=TUlr.l0; % [mm] anchorage length
srm0=TUlr.srm0;% max crack width
rhol=TUlr.rhol; % confining reinforcmeent ratio
As=TUlr.As; % total steel area (4*Abar)
Ac=TUlr.Ac; % total steel area (4*Abar)
nbars=TUlr.nbars; % number of steel rebars
ls=TUlr.ls; % [mm] lap splice length
Atot=TUlr.Atot; %[mm2] gross sectional area

E1=SMA_prop.E1;
E2=SMA_prop.E2;
E3=SMA_prop.E3;
fu_SMA=SMA_prop.fu;
dblSMA=SMA_prop.Dim;
srmSMA0=TUlr.srmSMA;
epsy=SMA_prop.eps1;% [-] strainat first configuration change
epsy2=SMA_prop.eps2;%
f1=SMA_prop.f1; % [-] Yield strain longitudinal reinforcement
f2=SMA_prop.f2; % [-] Yield strain longitudinal reinforcement
A=SMA_prop.A;

tau_0=bondSMA.taub0;
tau_1=bondSMA.taub1;

EAeq=Es*As+Ec*Ac;

% steel and concrete area within lap splice region considering both rebars contributing
As_lap=2*As;
Ac_lap=Atot-As_lap;
EAeq_lap=Ac_lap*Ec+As_lap*Es;

% yield and ultimate forces
Ny=fy*As;
Nu=fu*As;

%% Computation section
% determine applied force
if eps_atc<=epsys
    N_applied=eps_atc*Es*As;
else
    N_applied=epsys*Es*As+(eps_atc-epsys)*Esh*As;
end

% check sum of lap splice discretization add up to lap splice length
if sum(srm_LAP)==ls
else
    sprintf('Sum srm lap is %d while lap length is %d',sum(srm_LAP),ls)
    error('Lap splice length is not well discretized')
end

% check distance between 2 consecutive cracks
if any(srm_LAP<0.5*srmSMA0) || any(srm_LAP>srmSMA0)
```

```
    warning('one or more element within la splice region are smaller than srm0/2 or larger tha
srm')
else
end

% check input strain is larger than minimum for a crack at the lap splice ends and smaller
than ultimate steel strain
if eps_atc<fct*EAeq/(Ec*Es*As)
    sprintf(' eps at crack is %4d and the minimum strain at crack is
%4d',eps_atc,fct*EAeq/(Ec*Es*As))
    warning('The input strain is smaller than the minimum for a crack')
else if eps_atc>epsu
        error('The input strain is larger than the ultimate steel strain')
    else
    end

end

 sig =N_applied/A;
% eps_atc for the SMA
if sig <= f1
    eps_atc = sig/E1;
elseif f1 < sig && sig <= f2
    eps_atc = epsy+ (sig-f1)/E2;
elseif  sig > f2
   eps_atc = epsy2+ (sig-f2)/E3;
end

l_dev=TUlr.srmSMA;

%%%%%%%%%%%%%%%%%%%%%%%%%%%%%%%%%%%%%%%%%%%%%%%%%%%%%%%%%%%%%%%%%%%%%%%%%%%%%%%%
% cas 1
 if eps_atc<=epsy
    Nc_max=tau_b0*srm_LAP/2*pi*dblSMA*nbars;
    delta_ls=(eps_atc-Nc_max/(2*As*E1))*srm_LAP;
    w_ls=(eps_atc-Nc_max/(2*As*E1)-Nc_max/(2*Ac*Ec))*srm_LAP;
    srm_discr1=linspace(0,srm_LAP/2,pts_discr/2);
    ls_discr=[fliplr(srm_discr1)*-1,srm_discr1];
    epsS_discr_BOT = ls_discr ;
    epsS_discr_TOP = ls_discr ;
 end
  if epsy <= eps_atc && eps_atc <= epsy2
    l1=As*E1*(eps_atc-epsy)/(tau_1*pi*dblSMA*nbars);
% cas 2
    if l1<srm_LAP/2
        l2=srm_LAP/2-l1; %length from epsy to srm/2
        epsC=epsy-tau_0*pi*dblSMA*nbars*l2/(As*E1);
        epsE=tau_1*pi*dblSMA*nbars*l1/(Ac*Ec);
        epsF=epsE+tau_0*pi*dblSMA*nbars*l2/(Ac*Ec);
        delta_ls=epsC*srm_LAP+(srm_LAP+2*l1)*(epsy-epsC)/2+(eps_atc-epsy)*l1;
        w_ls=delta_ls-l1*epsE-2*l2*epsE-l2*(epsF-epsE);
        srm_discr1=linspace(0,l1,floor(pts_discr/srm_LAP*l1/2));
        srm_discr2=linspace(l1,srm_LAP/2,pts_discr/2-floor(pts_discr/srm_LAP*l1/2));
        ls_discr=[-srm_LAP/2+srm_discr1,-srm_LAP/2+srm_discr2,srm_discr2-l1,srm_discr1+l2];
        epsS_discr_BOT = ls_discr ;
        epsS_discr_TOP = ls_discr ;
% cas 3
    else
        Nc_max=tau_1*srm_LAP/2*pi*dblSMA*nbars;
        delta_ls=(eps_atc-Nc_max/(2*As*E2))*srm_LAP;
        w_ls=(eps_atc-Nc_max/(2*As*E2)-Nc_max/(2*Ac*Ec))*srm_LAP;
        srm_discr1=linspace(0,srm_LAP/2,pts_discr/2);
        ls_discr=[fliplr(srm_discr1)*-1,srm_discr1];
        epsS_discr_BOT = ls_discr ;
        epsS_discr_TOP = ls_discr ;
    end
  end
 if  epsy2 <= eps_atc
    l1=As*E2*(eps_atc-epsy2)/(tau_1*pi*dblSMA*nbars);
% cas 4
    if l1<srm_LAP/2
        l2=srm_LAP/2-l1; %length from epsy to srm/2
        epsC=epsy2-tau_0*pi*dblSMA*nbars*l2/(As*E3);
        epsE=tau_1*pi*dblSMA*nbars*l1/(Ac*Ec);
        epsF=epsE+tau_0*pi*dblSMA*nbars*l2/(Ac*Ec);
        delta_ls=epsC*srm_LAP+(srm_LAP+2*l1)*(epsy2-epsC)/2+(eps_atc-epsy2)*l1;
        w_ls=delta_ls-l1*epsE-2*l2*epsE-l2*(epsF-epsE);
```

```
        srm_discr1=linspace(0,l1,floor(pts_discr/srm_LAP*l1/2));
        srm_discr2=linspace(l1,srm_LAP/2,pts_discr/2-floor(pts_discr/srm_LAP*l1/2));
        ls_discr=[-srm_LAP/2+srm_discr1,-srm_LAP/2+srm_discr2,srm_discr2-l1,srm_discr1+l2];
        epsS_discr_BOT = ls_discr ;
        epsS_discr_TOP = ls_discr ;
% cas 5
    else
        Nc_max=tau_1*srm_LAP/2*pi*dblSMA*nbars;
        delta_ls=(eps_atc-Nc_max/(2*As*E3))*srm_LAP;
        w_ls=(eps_atc-Nc_max/(2*As*E3)-Nc_max/(2*Ac*Ec))*srm_LAP;
        srm_discr1=linspace(0,srm_LAP/2,pts_discr/2);
        ls_discr=[fliplr(srm_discr1)*-1,srm_discr1];
        epsS_discr_BOT = ls_discr ;
        epsS_discr_TOP = ls_discr ;
    end
 end
end
%  end
```

UNIVERSITÉ CATHOLIQUE DE LOUVAIN
École polytechnique de Louvain
Rue Archimède, 1 bte L6.11.01, 1348 Louvain-la-Neuve, Belgique | **www.uclouvain.be/epl**